TURUN
YLIOPISTO
UNIVERSITY
OF TURKU

Adsorption and catalysis in hydrogen evolution reaction environments

Kimmo Pyyhtiä

TURUN YLIOPISTON JULKAISUJA – ANNALES UNIVERSITATIS TURKUENSIS
SARJA – SER. F OSA – TOM. 78 | TECHNICA – INFORMATICA | TURKU 2026

TURUN
YLIOPISTO
UNIVERSITY
OF TURKU

ADSORPTION AND CATALYSIS IN HYDROGEN EVOLUTION REACTION ENVIRONMENTS

Kimmo Pyyhtiä

TURUN YLIOPISTON JULKAISUJA ANNALES UNIVERSITATIS TURKUENSIS
SARJA SER. F OSA TOM. 78 | TECHNICA INFORMATICA | TURKU 2026

University of Turku

Faculty of Technology
Department of Mechanical and Materials Engineering
Materials Engineering
Doctoral Programme of Technology

Supervised by

Professor Pekka Peljo University of Turku Turku, Finland	Doctor Ulriika Mattinen University of Turku Turku, Finland	Doctor Emilia Palo University of Turku Turku, Finland

Reviewed by

Professor Ifan Stephens Imperial College London London, United Kingdom	Professor Enn Lust University of Tartu Tartu, Estonia

Opponent

Professor Pawel J. Kulesza
University of Warsaw
Warsaw, Poland

The originality of this publication has been checked in accordance with the University of Turku quality assurance system using the Turnitin OriginalityCheck service.

ISBN 978-952-02-0584-3 (PRINT)
ISBN 978-952-02-0585-0 (PDF)
ISSN 2736-9390 (PRINT)
ISSN 2736-9684 (ONLINE)
Painosalama Oy, Turku, Finland, 2026

mut koska hyvää myös ma löysin sieltä,
niin valaiskoon nää seikat täysi valo

UNIVERSITY OF TURKU
Faculty of Technology
Department of Mechanical and Materials Engineering
Materials Engineering
PYYHTIÄ, KIMMO: Adsorption and catalysis in hydrogen evolution reaction environments
Doctoral dissertation, 186 pp.
Doctoral Programme of Technology
March 2026

ABSTRACT

Renewable energy generation methods, such as solar or wind power, are cost-effective and environmentally friendly energy sources, but their intermittent nature creates considerable challenges in their incorporation into the current energy infrastructure. As it stands, some of the production capacity has to be disconnected when supply exceeds demand, thus lowering the profitability of investments into renewable energy.

One potential solution is using the excess energy to produce hydrogen. Water molecules are dissociated into hydrogen and oxygen gases in electrolyzers and catalysts are used to improve the efficiency of these gas evolution reactions. However, the best catalyst materials are composed of valuable metals, such as platinum or palladium, resulting in increased investment costs of hydrogen production.

In order to reduce the quantity of the required noble metals, the first article of this doctoral dissertation examined the production of silver and palladium nanoparticles by electrodeposition in electrolytes based on different aqueous isotopes. The nucleation mechanism of the electrodeposition process was determined to be progressive in nature and that the growth of the nanoparticles could be suppressed with the use of D_2O-based solvents. The origin of damage observed in CR-39 polymer pieces in hydrogen evolution reaction environments was the focal point of the second research article of the thesis. Cavitation collapse of nanobubbles formed during gas evolution reactions was judged to be the most probable explanation for the origin of the damage. The third research article surveyed the adsorption sites of hydrogen atoms on the Pt(111) catalyst surface using electron paramagnetic resonance spectroscopy. It was reasoned that hydrogen adsorbs primarily onto on-top and fcc hollow sites.

Results from this research offer potential tools for the development of more specialized and cost-effective catalyst materials, and aid in characterizing material deterioration in hydrogen evolution reaction environments.

KEYWORDS: electrolysis, adsorption, hydrogen evolution reaction, electrodeposition, CR-39, cavitation, electron paramagnetic resonance spectroscopy

UNIVERSITÄT TURKU
Fakultät für Technologie
Abteilung für Maschinenbau und Werkstofftechnik
Werkstofftechnik
PYYHTIÄ, KIMMO: Adsorption and catalysis in hydrogen evolution reaction environments
Doktorarbeit, 186 S.
Doktorandenprogramm in Technologie
März 2026

ABSTRAKT

Erneuerbare Energiequellen, wie Solar- und Windkraft, erzeugen Energie kosteneffizient und umweltfreundlich, jedoch stellt ihre intermittierende Natur erhebliche Herausforderungen für ihre Integration in die Energieinfrastruktur dar. Bei Überproduktion muss ein Teil der Erzeugungskapazität abgeschaltet werden, was die Rentabilität von Investitionen in erneuerbare Energien verringert.

Eine mögliche Lösung besteht darin, die überschüssige Energie zur Herstellung von Wasserstoff zu nutzen. In Elektrolyseuren werden Wassermoleküle in Wasserstoff- und Sauerstoffgas zerlegt, und diese Reaktion läuft effizienter unter der Verwendung von Katalysatoren ab. Die besten Katalysatormaterialien bestehen aus wertvollen Metallen wie Platin und Palladium, was die Investitionskosten der Wasserstoffproduktion erhöht.

Um die benötigte Menge an Edelmetallen zu reduzieren, untersucht der erste Artikel dieser Doktorarbeit die Herstellung von Silber- und Palladiumnanopartikeln durch elektrochemische Abscheidung aus Elektrolyten, die auf unterschiedlichen Wasserisotopen basieren. Es wurde festgestellt, dass der Nukleationsmechanismus der Elektroabscheidung progressiv ist und dass das Wachstum der Nanopartikel durch den Einsatz von D_2O-basierten Lösungsmitteln unterdrückt werden kann. Im Mittelpunkt des zweiten Artikels der Dissertation stand der Ursprung der Schäden am CR-39-Kunststoff in einer Wasserstoffentwicklungsreaktionsumgebung. Es wurde festgestellt, dass die wahrscheinlichste Erklärung für die Schäden die Kavitationsimplosion von Nanoblasen ist, die durch eine Gasentwicklungsreaktion entstehen. In der dritten Studie wurden die Adsorptionsstellen von Wasserstoffatomen auf der Pt(111)-Katalysatoroberfläche mittels Elektronenspinresonanzspektroskopie untersucht. Es wurde angenommen, dass Wasserstoff hauptsächlich an On-Top-Stellen und fcc-Hohlstellen adsorbiert.

Die Forschungsergebnisse bieten potenzielle Werkzeuge für die Entwicklung spezialisierterer und kosteneffizienterer Katalysatormaterialien. Zudem können sie bei der Charakterisierung elektrolyseinduzierter Materialschäden helfen.

STICHWÖRTER: Elektrolyse, Adsorption, Wasserstoffentwicklungsreaktion, Elektroabscheidung, CR-39, Kavitation, Elektronenspinresonanzspektroskopie

TURUN YLIOPISTO
Teknillinen tiedekunta
Kone- ja materiaalitekniikan laitos
Materiaalitekniikka
PYYHTIÄ, KIMMO: Adsorption and catalysis in hydrogen evolution reaction environments
Väitöskirja, 186 s.
Tekniikan tohtoriohjelma
Maaliskuu 2026

TIIVISTELMÄ

Uusiutuvat energianlähteet, kuten tuuli- ja aurinkovoima, tuottavat energiaa kustannustehokkaasti ja ympäristöystävällisesti, mutta tuotannon vaihtelevuus aiheuttaa merkittäviä haasteita niiden sulauttamisessa nykyiseen energiainfrastruktuuriin. Nykyisellään ylituotannon hetkinä osa tuotantokapasiteetista on kytkettävä pois käytöstä vähentäen täten uusiutuvan energian investointien kannattavuutta.

Yksi mahdollinen ratkaisu on ylimääräisen energian hyödyntäminen vedyn tuottamiseen. Elektrolyysereissä vesimolekyylejä pilkotaan sähkön avulla vety- ja happikaasuiksi, ja näitä kaasunkehitysreaktioita tehostetaan katalyyttien avulla. Parhaat katalyyttimateriaalit koostuvat kuitenkin arvokkaista metalleista, kuten platinasta ja palladiumista, mikä nostaa merkittävästi vedyn tuotannon investointikustannuksia.

Vaadittujen jalometallien määrän vähentämiseksi tämän väitöskirjan ensimmäisessä artikkelissa tutkittiin hopea- ja palladium-nanopartikkelien valmistamista sähkösaostamalla käyttäen veden eri isotooppeihin pohjautuvia elektrolyyttejä. Työssä havaittiin sähkösaostuksen nukleaatiomekanismin olevan progressiivinen ja että nanopartikkelien kasvua voidaan hidastaa tekemällä elektrolyyttiliuos raskaaseen veteen. Vedynkehitysreaktioympäristössä CR-39-muoviin kohdistuvan vahingon alkuperä oli väitöskirjan toisen artikkelin keskiössä. Kaasunkehityksessä syntyneiden nanokuplien kavitaatiomaisen romahtamisen pääteltiin olevan todennäköisin selitys havaitulle vahingolle. Kolmannessa tutkimuksessa kartoitettiin vetyatomien adsorptiota Pt(111)-pinnalle elektroniparamagneettisen resonanssispektroskopian avulla. Vedyn järkeiltiin adsorboituvan pääasiassa joko yksittäisen platina-atomin päälle tai kolmen platina-atomin pintakeskeiseen ontelokohtaan.

Väitöskirjan tutkimustulokset tarjoavat mahdollisia työkaluja entistä erikoistuneempien ja kustannustehokkaampien katalyyttimateriaalien kehittämiseen sekä elektrolyysissä tapahtuvien materiaalivaurioiden karakterisointiin.

ASIASANAT: elektrolyysi, adsorptio, vedynkehitysreaktio, sähkösaostaminen, CR-39, kavitaatio, elektroniparamagneettinen resonanssispektroskopia

Acknowledgements

One should not wait until the very end, to the triumphant speeches and stories of remembrance, to finally express their gratitude towards those who deserve it the most; rather, such words of import should be given then and there. Nevertheless, I want to begin by thanking University of Turku, Department of Physics and Astronomy, and the Materials Engineering unit for this opportunity to study, work, research and grow as a person. For financial support of this doctoral thesis, I would like to acknowledge the funding provided by the EU Horizon 2020 HERMES project.

Next, as is appropriate, thanks should be given to my doctoral supervisor Pekka Peljo, without whom this long journey would not have been possible, for it began with him approaching me with an exciting yet challenging topic, and in the midst of its trials he was always there to point the way when the straightforward path had been lost. With his support I was encouraged to develop my skills and practices to one day shine on my own travels on whatever paths I chose. He introduced me to a great network of academic researchers and provided me with opportunities I never could have hoped for. My thanks should also be given to my two other supervisors, Ulriika Mattinen and Emilia Palo, for their support and advice on various points of this journey. Ulriika's high-spirited presence and positivity would always light up one's day, and Emilia could always be trusted to lend her ear when I had something on my mind. Additionally, I want to thank my collaborators from the HERMES project, with whom I have had the pleasure of co-operating in two publications included in this thesis.

What else would have made the journey up to this point worth it, if not the people I have shared that time with? Starting from our research group, I want to express my deepest gratitude to Jenna Hannonen and Gabriel Gonzalez, without whom I don't think I would be writing these words. Thank you for your support and all the moments we've shared. I would also like to thank Jenni Jarju, Jerzy Jasielec and Valtteri Vinni for being some of the best office mates one could hope for. And thank you to all the good people at the Materials Engineering unit; the community that has arisen there in such a short time is something truly special.

Now, there are also those who have been sharing this fate with me, on their own journeys and their tribulations, and like myself, have learned which parts of tales told of doctoral studies are true. With that, I want to thank my fellow expeditioners: Mikko Miettinen, Matilda Sipilä, Anton Nykänen, Elias Ervelä, Kerttu Pusa, Lauri Heinonen, Amanda Myntti, und natürlich Tina Neumann. Many are still waiting for their day of graduation, but I have no doubt in my mind that they will reach that moment. Thank you for partaking these gifts of academic life with me.

Many a page would need to be added, for all those deserving of my thanks and mention, to be named here, but as is often the case, these people are part of larger communities, or rather they are what make said communities. With that, I want to thank these people for making my time at the university worth it, and say that I'm truly honored to be part of these groups. My deepest thanks to Delta, RTT, Perjantailounas, all the board game groups, Sigmanaali, Adamas, Treberyhmä and TYLVO. A special mention goes to all the people of HybridiSpeksi for being so passionate, yet welcoming about working together to make what to me is one of the greatest forms of art.

And last, but certainly not least, I want to thank my family; my father Jarmo for his encouraging engineering mindset and quiet yet reliable support, my mother Lea for her love of language and art, and for her kindness, and, of course, Heidi for being my sister. They have been there since the beginning.

In conclusion, thank you to everyone who has shared this journey of my life with me up to this milestone. But let us not rest for long – the future awaits, our work continues – ne'er to be finished, but to be carried on by those who come after.

15.2.2026
Kimmo Pyyhtiä

Table of Contents

Abbreviations

3D	Three-dimensional
AI	Artificial intelligence
CA	Chronoamperometry
CE	Counter electrode
CR-39	Columbia Resin 39, Poly(allyl diglycol carbonate)
CV	Cyclic voltammetry/voltammogram
DFT	Density functional theory
DSA	Dimensionally stabilized anode
EC	Electrochemical/Electrochemistry
EPR	Electron paramagnetic resonance
fcc	face-centered cubic crystal structure
FTIR	Fourier-transform infrared spectroscopy
FT-IRAS	Fourier-transform infrared reflection absorption spectroscopy
H_{ads}	Adsorbed hydrogen
HCA	high contact angle
hcp	hexagonal close-packed crystal structure
HER	Hydrogen evolution reaction
H_{upd}	Hydrogen underpotential deposition
H_{opd}	Hydrogen overpotential deposition
ICP-MS	Inductively coupled plasma mass spectrometry

IHP	Inner Helmholtz plane
IR	Infrared (wavelengths)
LASV	Large amplitude sinusoidal voltammetry
LR-FES	Laterally resolved free energy surface
MD	Molecular dynamics
ML	Molecular layer
NMR	Nuclear magnetic resonance
OER	Oxygen evolution reaction
OHP	Outer Helmholtz plane
pc	polycrystalline
PLA	Polylactic acid polymer
RE	Reference electrode
RHE	Reversible hydrogen electrode
ROI	Region of interest
SEIRAS	Surface-enhanced IR absorption spectroscopy
SEM	Scanning electron microscope
SHE	Standard hydrogen electrode
STM	Scanning tunneling microscopy
WE	Working electrode
XRD	X-Ray diffraction

List of Original Publications

This dissertation is based on the following original publications, which are referred to in the text by their Roman numerals:

I **Kimmo Pyyhtiä**, and Pekka Peljo. Isotope effects in the electrodeposition of Ag and Pd, *J. Electroanal. Chem.* 947 (2023) 117759.

II **Kimmo Pyyhtiä**, Jerzy J. Jasielec, Tom Sillanpää, Jere Hyvönen, Rainer Götz, Lilian Moumaneix, Vincent Martin, Arnaud Viola, Frédéric Maillard, Tanja Kallio, Ari Salmi, Elena Gubanova, Aliaksandr Bandarenka, and Pekka Peljo. Investigation of CR-39 damaging mechanisms in electrochemical environments. *Submitted.*

III Rainer Götz, **Kimmo Pyyhtiä**, Bingxin Li, Theophilus K. Sarpey, Kun-Ting Song, Mira Todorova, Nadezhda Kukharchyk, Siegfried Schreier, Pekka Peljo, Elena L. Gubanova, Jörg Neugebauer, Aliaksandr S. Bandarenka. In-situ EC-EPR Spectroscopy & DFT simulations of H_{upd} on Polycrystalline Pt, *ChemSusChem*, in press, DOI: 10.1002/cssc.202501908

The original publications have been reproduced with the permission of the copyright holders.

Author's contribution

Within each of the research projects, the doctoral candidate was responsible for designing, assembling and operation of the electrochemical experiments, and extracting quantitative information from the data generated during the experiments. In addition to preparing the solutions and cells used in the experimental works, the candidate contributed substantially to the interpretation of the results and the iteration of experimental setup.

In **Publication I** and **Publication II**, the doctoral candidate was the first author of the research article, and as such, was responsible for data analysis and visualization, and writing the manuscript with input from the co-authors. In these works, the candidate performed bulk of the experimental parts with co-authors contributing to individual experiments.

In **Publication III**, the doctoral candidate shared first authorship with two other researchers, all of whom contributed equally to the work, with the candidate's main contribution being in performing the *in situ* electrochemical electron paramagnetic resonance measurements. Additionally, in this collaboration the candidate took part in the interpretation of the experimental results and assisted in the writing and editing of the manuscript, especially in the introductory and experimental sections.

Declaration of AI use

In preparing this dissertation, generative artificial intelligence (AI) has been used as a search engine in finding literary sources and to debug Python / LaTeX code. No plain text in this dissertation has been written or edited using AI tools with the exception grammar inspection of the abstracts. No AI was used in developing research questions, to analyze data or to draw conclusions.

1 Introduction

The current world economy is based on greenhouse gas emitting fossil fuels that are causing the ever-worsening climate destabilization, which is already leading to an extreme crisis for the Earth's biosphere. The best way to lessen the impacts of climate change is removing fossil fuels as the lifeblood of the world economy and supplanting them with energy created by less destructive, mostly renewable green energy sources. According to the rules of the economy, this will be possible only when renewable energy is economically more viable than fossil fuels. Of the current green energy sources, solar panels, wind turbines and hydropower are already economically more competitive per unit of produced energy than thermal plants burning fossil fuels. These production methods are, however, extremely dependent on the geographical location, season, time of day and the local weather meaning that they are inherently more unreliable than fossil fuels for continuous and stable energy production. Adding to this, electricity is not the ideal energy carrier for many applications, such as in the transportation sector where a continuous grid connection is not possible. Thus, the energy needs to be rendered into a form better suited for storage to balance out the varying energy production and consumption, and to enable its physical transportation.

One approach for storing green electricity is converting it into hydrogen gas via water electrolysis. Hydrogen is an attractive alternative for fossil fuels due to its high gravimetric energy density, low carbon emissions and high availability of its feedstocks: water and electricity. Hydrogen gas is stored in pressurized or liquefied form, and can thus be transported with relative ease. In industry, hydrogen gas can be used directly e.g. in production of carbon-free steel, or processed further into important industrial chemicals such as ammonia, or used in conjunction with carbon capture technologies to create e-methanol or other e-fuels.

Renewable hydrogen gas is generated by using electricity to split water molecules into hydrogen and oxygen gases. This is done in electrochemical cells known as electrolyzers, where water molecules decompose on the electrode surfaces.

Water splitting is made more efficient by utilizing catalyst materials that promote the various steps involved in the electrolysis process. Best catalyst materials, however, are often scarce noble metals, and thus the high capital requirements limit the competitiveness of production of hydrogen-based alternatives to fossil fuels. Development of new catalysts and minimizing the amount of expensive materials required are of vital importance in the wider adoption of hydrogen-based economy.

This doctoral dissertation is composed of three **original publications** that each approach hydrogen evolution reaction from their own research questions. In **Publication I**, the effect of solvent isotope substitution from H_2O to D_2O on the nucleation mechanism and kinetic parameters during Ag and Pd electrodeposition on graphite substrate has been examined. Additionally, this work deliberates if isotope-dependent effects originate from mass-transport, solvation and/or interfacial factors instead of isotope-substitution related influences in bulk electrochemical thermodynamics. Isotope substitution rarely significantly affects the chemical properties of the electrolyte, and thus it would provide an additional method to customize noble metal catalyst nanoparticles grown via electrodepostion. **Publication II** delves into the hydrogen evolution reaction environments, with concurrent deposition of metal species and hydrogen evolution, to examine what non-nuclear mechanisms can produce surface damage on CR-39 that resembles tracks produced by energetic particles. Despite the complex nature of the examined system, the research article found evidence indicating cavitation effects as the damage mechanism, and suggested that CR-39 could be used in characterizing cavitation processes in electrochemical cells with hydrogen gas evolution. Finally, **Publication III** examined the feasibility of using *in-situ* electrochemical electron paramagnetic resonance spectroscopy (EC-EPR) to study paramagnetic signals originating from hydrogen atoms adsorbed on polycrystalline platinum in non-cryogenic temperatures. This first-of-its-kind work presented that statistically dominant adsorption sites of hydrogen on Pt could be deduced from the EPR signal of the system. These results were supported by computational modeling also included in the research article. The overarching aim of the research included in this thesis has been in trying to shed light on how solvent isotope composition, hydrogen electrosorption and hydrogen evolution phenomena affect the interfacial kinetics and the observed outcomes in electrochemical systems relevant for hydrogen production in water electrolyzers. Chapters 2–5 provide the necessary background for the theoretical and practical considerations of the phenomena, materials, experiments and characterization methods for the summary of the work done in original publications presented in Chapters 6, 7 and 8.

2 Electrochemical background

Electrochemistry is the study of chemical reactions on interfaces that are connected via an external electrical circuit. Whereas in conventional chemistry electrical charge is transferred directly between the reactants, in electrochemistry the external circuit is used for charge transfer, thus also allowing for the physical separation of the reactants themselves. Connecting a potentiostat to the external circuit allows the precise control and recording of current and/or potential. The direction and rate of a given electrochemical reaction is dependent on the potential of the electrochemical cell. Unlike chemical reactions, which are rarely reversible without changing system temperature or pressure, in many cases electrochemical reactions are easily reversed by simply modifying the cell potential. Reversible electrochemical reactions are the basis of several modern technologies such as rechargeable batteries and fuel cells. This section aims to give a brief overview on the concepts of electrochemistry that are the most relevant to the research presented in this thesis based on some fundamental literature in electrochemistry [1, 2] and the author's Master's thesis [3] with additional references provided when necessary.

At their simplest form an electrochemical cell is composed of only a few components. Two conducting electrodes are submerged in a conducting medium, known as an electrolyte, and connected via an external circuit. Electrolytes are materials that conduct electricity via transport of ions, not electrons, and they are generally composed of a solvent, most commonly water, and salts dissolved into the solvent [1]. An example of a two-electrode cell is illustrated in Figure 1a. The potential between the two electrodes, i.e. the cell potential, is given by the chemical potentials of half-reactions, determined by electrode and electrolyte composition, taking place at each electrode. In galvanic cells, the reaction potentials are such that the reactions initiate spontaneously once the electrodes are connected and current starts to flow. Battery being discharged is prime example of a galvanic cell. Most industrial electrochemical reactions are, however, not spontaneous but rather require external voltage to be applied to the electrode to initiate and sustain the reaction. Electrolyzers are by their nature this kind of electrolytic cells [2].

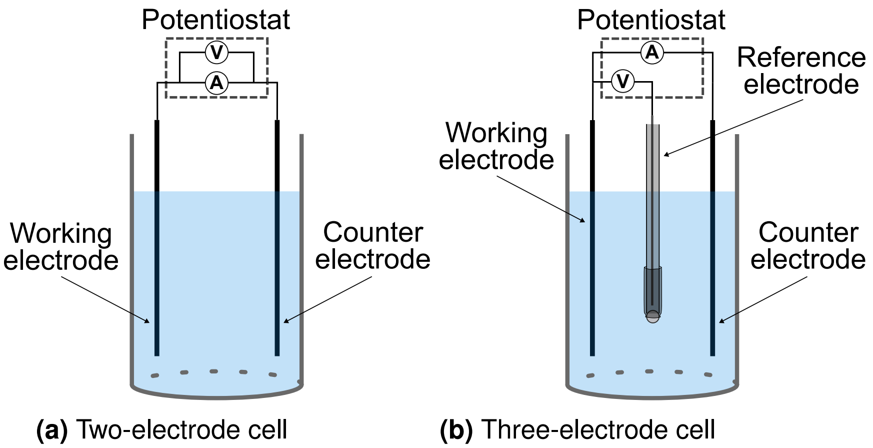

(a) Two-electrode cell **(b)** Three-electrode cell

Figure 1. a) The simplest electrochemical cells used in research consist of a working electrode and a counter electrode connected by an external circuit to a potentiostat that measures and controls the potential and/or current. b) A third electrode with a known reaction potential is often added as a reference electrode and all other potentials in the system are measured against its potential. Author's own illustration.

Reactions within an electrochemical cell are described by the chemical potentials of its electrochemical species. Electrochemical species is any such constituent of the electrode or electrolyte that can be distinguished as a unit of matter with identical energy levels with respect to other members of said species, be it atom, ion, molecule, radical etc., and as such they have their characteristic chemical potentials. Any total cell reaction is composed of half-reactions taking place at their respective electrodes. In oxidation half-reaction, a species donates one or more electrons to the more positive potential electrode known as anode. Likewise, reduction half-reaction sees a species accepting one or more electrons from the cathode, the electrode with more negative potential. Oxidation and reduction half-reactions together form the overall cell redox reaction. In standard conditions each reduction and oxidation reactions have their characteristic standard reduction and oxidation half-reaction potentials, E°_{red} and E°_{ox}. The overall standard cell potential E° is given by the difference of the standard half-reaction potentials [1].

Very commonly these half-reactions are investigated individually and the electrode where that reaction of interest, whether cathode or anode, takes place is designated as the working electrode (WE), while the remaining electrode is known simply as the counter electrode (CE). Electrodes are connected to a potentiostat, which can be used to record and/or control the cell potential or current. Cell potential is dependent on the half-reactions within the cell, and the half-reactions are in turn affected by the cell potential, resulting in a feedback loop. Thus the cell potential in a two-electrode cell cannot be controlled precisely with a potentiostat. Commonly a third electrode, known as a reference electrode (RE), with a half-reaction with a known potential is added to the cell to serve as the reference potential against which all potentials in the cell are measured [1]. A three-electrode cell is depicted in Figure 1b. Standard hydrogen electrode (SHE), where protons are reduced to gaseous hydrogen on platinum, has been defined as $E^\circ = 0$ V and all other electrochemical reaction potentials are defined against this reference potential [1]. In many cases, other reference electrodes with other half-reactions with known potentials against SHE are used.

2.1 Nernst equation

Cell potential of an electrochemical cell in equilibrium is often not exactly the same as the one given by the standard reaction potential. The potential is also affected by the relative concentration of the electron acceptors (oxidants) and electron donors (reductants). In a reduction reaction a dissolved chemical species accepts electrons from the cathode and reduces, and its the concentration/activity has an effect on the cathode potential. This can be understood by the constituents of the reducing species each having their "pull" on the cathode electrons and if their concentration drops as the reducing species is consumed during the reaction, this force on the cathode electrons is reduced. Similarly, on the anode the concentration of the species being oxidized has an effect on the anode potential. In thermodynamic equilibrium, i.e. when the oxidation and reduction reactions are transferring charge at equal rates and the net current is zero, and assuming rapid electron transfer [1], the behavior of the cell potential E is described by the Nernst equation:

$$E = E^{\circ\prime} + \frac{RT}{nF} \ln \frac{C_{\mathrm{ox}}}{C_{\mathrm{red}}}, \tag{1}$$

with $E^{\circ\prime}$ denoting formal potential at the given temperature and at 1 bar pressure, and where the ideal gas constant $R = 8.314\ \frac{\mathrm{J}}{\mathrm{K \cdot mol}}$, T [K] is the temperature, n is the number of transferred electron, Faraday constant $F = 9.649 \cdot 10^4\ \mathrm{C \cdot mol^{-1}}$, and C_{ox} and C_{red} are the oxidizing species and reducing species bulk concentrations, respectively[1]. Use of concentrations instead of activities is a common approximation when reactant species concentrations are low, and for example in aqueous solutions in standard conditions [1]. When the concentrations (more precisely activities) of the oxidizing and reducing species are the same and they are consumed/generated at the same rate, the formal potential $E^{\circ\prime}$ approaches the standard potential E° because $\ln \frac{C_\mathrm{ox}}{C_\mathrm{red}} = \ln 1 = 0$. When the system is not in thermodynamic equilibrium, i.e. rate of oxidation and reduction is not the same, the ratio of oxidized and reduced species will change as a function of time, resulting in a change in the Nernst potential, i.e. measured potential without current flow.

2.2 Overpotential and kinetics

By applying a potential difference between the electrodes that differs from the equilibrium potential, the thermodynamically favorable reactions can be accelerated, decelerated or even reversed. Electrodes are made of conducting materials and as such have a continuous energy states around the Fermi level E_F, energy level that has equal probability of being occupied or unoccupied by an electron [4]. When a potentiostat applies a voltage between the WE and CE, the electrode Fermi levels shift as presented in Figure 2, and the occupied cathode electron states now have a higher energy on average than the unoccupied states of the electrolyte species, thus making the electron transfer from the electrode to the electrolyte energetically favorable. Simultaneously on the anode, the electrode Fermi level becomes lower than the energies of the occupied states of the electrolyte species and electrons start transferring from the electrolyte to the anode [1].

Deviation from the equilibrium potential is described by overpotential η, which is simply the difference between the applied, non-equilibrium, potential E_app and the thermodynamic equilibrium potential (from the Nernst equation [2]) E_eq:

$$\eta = E_\mathrm{app} - E_\mathrm{eq}. \tag{2}$$

When η is positive, reduced species start to be oxidized until equilibrium is reached. The rate of the oxidation reaction may depend on the kinetics or mass transfer of the species. Lowering the applied potential closer the equilibrium potential on the other hand slows the steady-state reaction until it stops completely. Further lowering the applied potential results in reduction of the oxidized species [5].

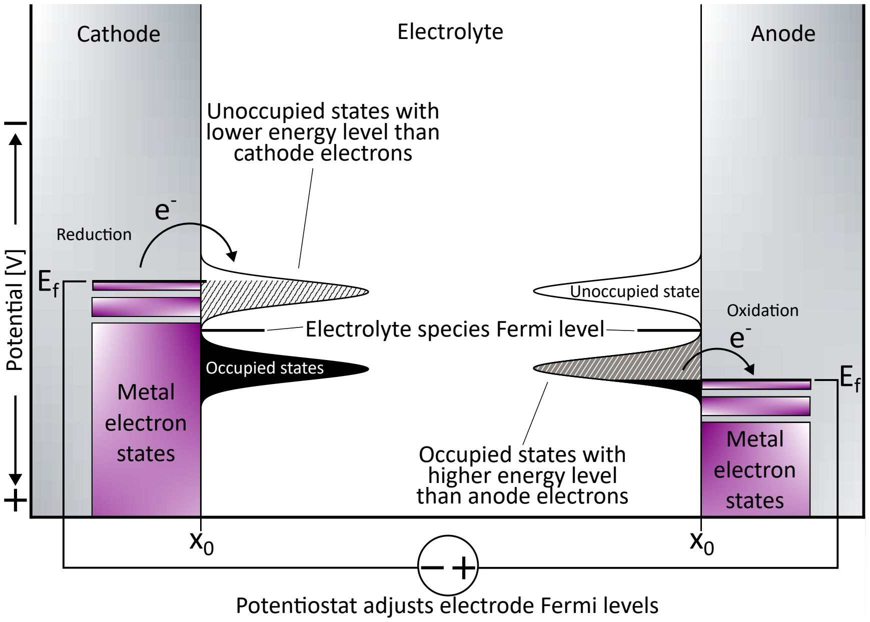

Figure 2. Illustration of the electrode and electrolyte species energy levels when a potentiostat applies a potential difference between the electrodes, thus changing the favorable energy levels from the equilibrium chemical potentials. In reduction reaction, the Fermi energy of the metal electrode is increased above the unoccupied energy levels of the reducing species making the transfer of electrons from the cathode to the reducing species energetically favorable. Similarly, oxidation reaction takes place on the anode where the electrode electron energy levels are lowered below the energy level of the oxidizing species occupied states resulting in transfer of electrons to the anode. Author's own illustration.

2.3 Chronoamperometry

Applying a potential difference between the working and counter electrodes is one of the most basic type of electrochemical measurement or application. In chronoamperometry (CA), a potentiostat is used to apply a stepwise potential difference E_d deviating from the equilibrium potential between the two electrodes. Meanwhile, the time evolution of current is recorded into what is known as a chronoamperometric curve or a current transient. Chronoamperometric curves are indicative of reactions occurring on the electrode surfaces [2]. In Figure 3, a chronoamperometric curve for electrodeposition of dissolved palladium on pencil graphite is presented. At the very first moments after the potential step a great increase in current is seen followed by its rapid decay. This current spike is caused by charging of the electrical double-layer where the reorientation of the electrolyte and solvent species functions akin to a capacitor in an electrical circuit [1].

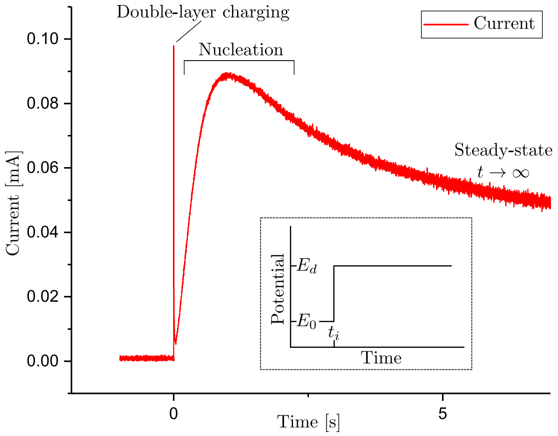

Figure 3. Demonstrative chronoamperometic curve obtained from electrodeposition of Pd^{2+} in a three-electrode cell illustrates the current spike associated with charging of the electrical double-layer followed by the nucleation peak. Author's own illustration.

Following the double-layer charging, the dissolved Pd^{2+} cations near the cathode reduce into metallic palladium, which is seen as an increase in the cell current. Surface features such as defects, steps or earlier deposited Pd sites are energetically more favorable for Pd^{2+} cations to deposit at, and are thus favored by the subsequent Pd ions to deposit at [6]. These nuclei of hemispherical islands grow over time and and start overlapping with each other, limiting the effective surface area for the Pd^{2+} deposition [7]. The palladium reduction reaction is in the end limited by the mass transfer of new Pd^{2+} cations from the bulk electrolyte to the electrode surface as $t \to \infty$ [5]. Electrodeposition and nucleation is described in more detail in Section 2.7.

2.4 Cyclic voltammetry

Like earlier alluded to, different reactions take place in an electrochemical cell depending on the instrument applied overpotential. These reactions can be investigated using cyclic voltammetry (CV) where a chosen potential window is scanned at some scan rate [V/s] and the corresponding current is recorded. Current–voltage profile shows characteristic responses that correspond to new reduction/oxidation reactions that initiate gradually at certain applied potentials [2]. The result of such a measurement is a cyclic voltammogram, also abbreviated as CV, and one such CV is presented in Figure 4. Starting from initial potential of E_0 and applying more negative potentials sees the reduction of the electroactive

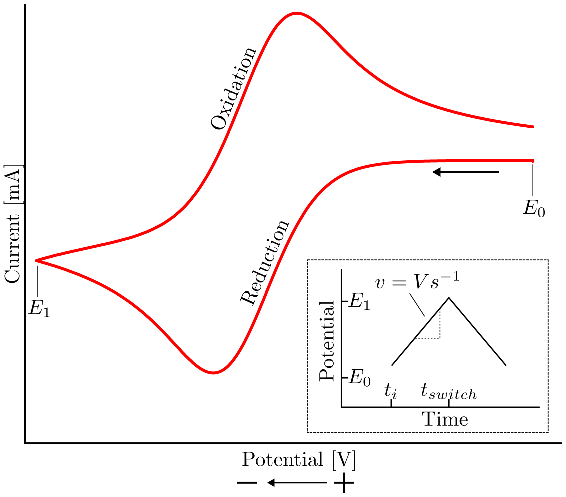

Figure 4. Simulation of a perfectly reversible reduction-oxidation cyclic voltammogram. Sweeping the applied potential from E_0 to E_1 the cathodic peak is associated with reduction of the electroactive species and on the reverse sweep the anodic oxidation peak is observed. Inset shows the potential profile of one CV cycle. Author's own illustration.

species initiating and eventually reaching the cathodic peak current before being limited by the transfer of new reducing species to the electrode surface [1]. On the return scan the oxidation of previously reduced species is seen, and after the anodic peak the transfer of reactants limits the current. This cycling can be repeated again multiple times.

The degree of reversibility of a given redox reaction can be deduced from the CV by examining the positions, i.e. potentials, and shapes of the cathodic and anodic peaks [8]. More symmetrical they are, the more reversible the reaction is. A deviation from perfect reversibility can indicate that some reaction products are created that are can no longer be returned to their original state, for example the generation of gaseous hydrogen in an electrolyzer. Another important observation can be made when examining multiple cycles of the same system: if the CVs are nearly identical over many cycles, that is an indication that the reactants are stable and generate little to no side products that would no longer participate in the main cell reaction. This kind of information is vital when examining reactants for e.g. rechargeable batteries.

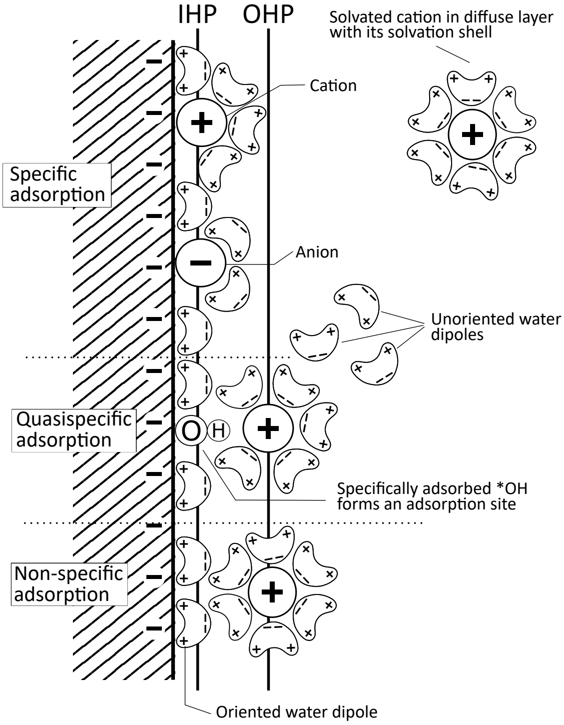

Figure 5. Structure of the electrical double-layer is composed of the inner Helmholtz plane situated in the plane of center of mass composed of the first adsorbed water monolayer and the specifically adsorbed ions chemibonded to the electrode surface. Outer Helmholtz plane resides at the center of mass of quasi- and nonspecifically adsorbed species with limited interaction with the electrode surface. Beyond the OHP lies the diffuse layer that is characterized by the concentration gradient of the excess of dissolved cations compared to the bulk electrolyte due to the electrostatic migration of the species. Author's own illustration based on [9, 10].

2.5 Electrical double-layer

Earlier for the case of palladium electrodeposition it was mentioned that when the potential step is applied, in the very first moments a sharp spike and subsequent drop in current are observed. This is due to the charging of the electrical double-layer. Electrochemical reactions take place in the vicinity of the electrode–electrolyte interface and in this region the behavior of the solvent molecules and dissolved ions differs from the bulk electrolyte. Unlike in the bulk electrolyte where for a given volumetric element the charge neutrality is conserved, near the electrodes the applied potential causes the polar solvent, usually H_2O, molecules to orient themselves and adsorb, along with the dissolved ions, on to the electrode surface. In an electrochemical cell, where a potential difference, i.e. electric field, is applied between two electrodes, most of the potential change occurs within the electrical double-layer due to the reordering of charges in the vicinity of the electrode. This means that the changes in the electric fields are confined within the sub-nanometer scale of the double-layer, causing extremely high derivatives in the electric field, which drives the rapid reorientation of the solvent molecules and rearrangement of the solvated ions. However, this approximation is valid only for electrodes composed of ideal Drude metals, such as Au or Pt, where there is no potential drop inside the electrode material [11, 12]. In graphite, part of the potential drop takes place within a thin surface layer of the electrode itself [13, 14]. Therefore, in addition to electrical double-layer charging, part of its capacitor-like behavior originates from reordering of the electronic structure of the electrode surface layers [15].

The region of adsorbed species in close vicinity of the electrode surface is known as inner Helmholtz plane (IHP). Adsorbed water molecules orient themselves into a monolayer along the interface, thus forming a hydrogen bonding network at the metal–electrolyte interface. Additionally dissolved ions can shed their solvation shells and adsorb onto the electrode surface, leading to specific adsorption. In non-specific adsorption, the dissolved species are unable to shed their solvation shells and are only electrostatically adsorbed onto the electrode surface without interacting with it directly. Adsorption can also be mediated by another specifically adsorbed species, such as an *OH-group that retains a considerable part of its negative charge after the partial electron transfer to the electrode, allowing adsorption that is dependent on the chemical properties of the mediator species and the cation, separating quasispecific adsorption from non-specific adsorption, where interaction with the electrode surface is purely electrostatic. Depending on the definition, the outer Helmholtz plane (OHP) is usually considered to be the plane of the center of mass of non-specifically adsorbed species, with the quasispecifically adsorbed species being located in its vicinity. Ions of the outer Helmholtz plane often act as intermediates for solvated ions that partially shed their solvation shells while bonding with some surface adsorbed species [10]. Figure 5 expands on the structure of the electrical double-layer.

2.6 Mass transfer

After the charging of the electrical double-layer, the current is now limited by either the kinetics of the cell reaction or by the movement of the charge carrying electrochemical species in the electrolyte. For a dissolved species to oxidize or reduce it needs to move from the bulk electrolyte close enough to the electrode

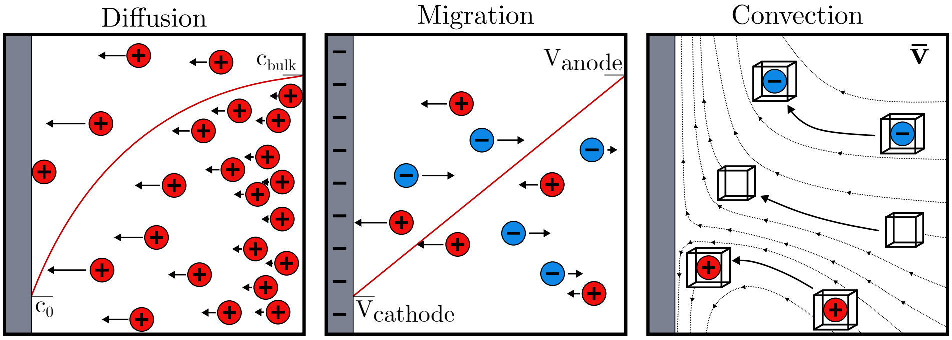

Figure 6. Mass transfer of active species is described by three mechanisms. Diffusion arising from Brownian motion sees the dissolved species on average counteracting concentration differences caused by the removal of the said species from the solution near electrode boundary. In migration, electric fields within a electrolyte solution apply forces on dissolved charged species causing their drift towards the electrode with the opposite charge. Convection is the flow of the solution itself originating from either physical stirring of the solution or by being induced by the first two mechanisms when they cause bulk motion of the solvent elements [5]. Author's own illustration.

surface for the electron transfer to occur. In inner sphere reactions the solvation shell is shed whereas in outer sphere reactions the electron is transferred via tunneling through the IHP. Thus the transfer of mass can be a considerable limiting factor for the overall redox process.

Mass is transferred by three different mechanisms; by Brownian diffusion following the ion concentration gradient, by migration of the charged particles along the gradient of the electric field, and by forced movement of the fluid itself i.e. convection. These are illustrated in Figure 6. In an equilibrium, mass flux $\mathbf{J}$ for chemical species j is described by steady-state Nernst-Planck equation:

$$\mathbf{J}_j = -D_j \nabla C_j - \frac{z_j F}{RT} D_j C_j \nabla \phi + C_j \mathbf{v}, \tag{3}$$

where D_j is the diffusion coefficient, C_j is the concentration and z_j is the charge of the species j, with ϕ and $\mathbf{v}$ being the electric potential and fluid velocity field, respectively. There are no drastic concentration differences in the bulk electrolyte meaning that mass transfer in bulk is usually driven by migration and convection but near the electrodes the concentration of the reactants varies greatly due to the reactant species being consumed by the reduction and oxidation reactions, respectively. So, near the electrode surfaces diffusion becomes a significant component of the overall mass transfer. Vicinity of electrode surfaces also affects the migration and convection. Most of the potential drop takes place in a few nanometers over the electrical double-layer and thus effectively shields the dissolved species in the diffuse layer from electrode's electric field thus considerably limiting the mass transfer through the Helmholtz planes. However, adsorption of dissolved species and the associated charge transfers affect the electrical double-layer locally, and thus the screening is not only a bulk phenomenon but rather it is also coupled with the interfacial chemistry [16]. Similarly, due to viscosity any fluid element necessarily has zero lateral velocity at the electrode surface, which limits the mass transfer by convection even to the diffuse layer [17]. Generally diffusion is the rate-determining process in mass transfer, especially if charge transfer is promoted by addition of a supporting electrolyte, where ionic salts that don't themselves affect the reaction of interest, are added to the electrolyte and carry most of the charge in the system [2]. With this, the approximation that the reactant of interest carries no current by migration, can be made, and then by taking the divergence of Equation 3, the non-steady-state Nernst-Planck equation can be derived into Fick's second law of diffusion by assuming the electrolyte is not stirred ($\mathbf{v} = 0$) and is incompressible ($\nabla \cdot \mathbf{v} = 0$) giving the following expression:

$$\frac{\partial C_j}{\partial t} = D_j \nabla^2 C_j. \tag{4}$$

Generally speaking, a large portion of electrochemical reactions are observed to be under diffusion control, and as such the rate of electron transfer at the electrode, i.e. current, is proportional to the reactant flux reaching the electrode by diffusion [1]. However, it is also possible that the kinetics of the electron transfer or the availability of energetically favorable adsorption sites limit the flow of charge more than the diffusion mass transfer [5].

2.7 Nucleation

When an overpotential is applied to the working electrode, which is defined respect to the reference electrode in a three-electrode cell, oxidation and reduction reactions initiate, with the reaction of interest taking place at the working electrode and the complementary reaction is sustained at the counter electrode. In the earlier case of electrodeposition of palladium the current can be limited not by the diffusion of palladium ions but rather by the availability of energetically favorable adsorption sites on the electrode surface for the ions to reduce at, known as active sites. Active sites are formed by imperfections of the electrode surface, such as interstitial atoms, vacancies, grain boundaries or steps, as those surface features can have lower free energies than the clean electrode surface. Dissolved metal ions are more likely to adsorb and reduce at these locations forming a nucleus.

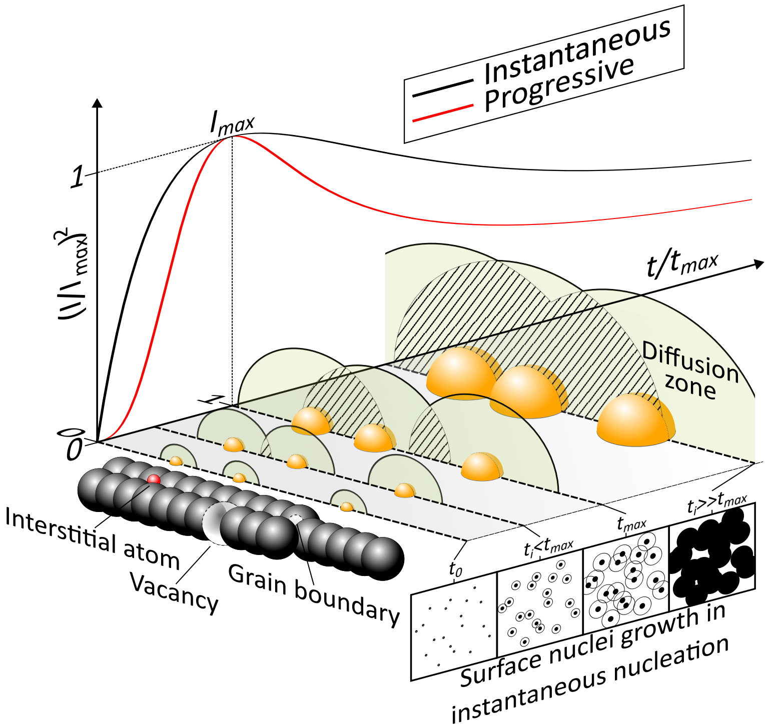

Figure 7. Surface defects are required for the formation and growth of nuclei in electrochemical nucleation. Each nucleus grows as dissolved species within its corresponding diffusion zone attach to the nucleus, resulting in gradual growth and eventual overlap of neighboring diffusion zones. The current reaches its maximum I_{max} at time t_{max} corresponding to the maximum non-overlapping surface area of the diffusion zones [7]. At $t > t_{max}$, the overlap of the diffusion zones of neighboring nuclei limits the incorporation of new ions into the nuclei, resulting in planar diffusion zones, and thus planar growth when $t \to \infty$. Here, instantaneous nucleation mechanism is depicted, where all nucleation sites are activated at t_0, resulting in homogeneous growth of nuclei. Author's own illustration.

Nuclei of the previously deposited ions are also energetically favorable sites for subsequent ions to deposit at, leading to the growth of the nuclei. Each nucleus can be thought as having its own hemispherical diffusion zone extending to the electrolyte from where any ion of the active species is likely to deposit on that nucleus. However, as the nuclei grow, so do their diffusion zones, which results in the diffusion zones of individual nuclei overlapping, limiting their growth. In such a system, the current reaches its maximum I_{max} at t_{max} when the electrode surface is maximally covered by non-overlapping diffusion zones [18]. Eventually, at $t >> t_{max}$ the diffusion zones overlap with each other maximally resulting a planar diffusion zone and planar metal deposition.

Prospective active sites are not created equal and as such, not all sites are necessarily activated at the onset of the applied potential. As opposed to instantaneous nucleation, where all sites activate immediately and grow at the same rate, in progressive nucleation the nucleation sites are activated over time after the more energetically favorable sites have been exhausted [19]. This results in heterogeneity in the growing nuclei, i.e. variation in their size and growth rate. As the nucleation mechanism in the end is determined by the thermodynamics of the deposition of individual ions, which in turn is affected by the surface material and structure as well as the type and concentration of the active species along with the solvent properties, the exact parameters that govern the nucleation mechanism are difficult to evaluate. Fortunately, the overpotential can be tuned precisely allowing for more selectivity in the nucleation mechanism, as e.g. with higher overpotentials more sites are activated immediately resulting in instantaneous nucleation mechanism being favored.

First theoretical description of the nucleation mechanisms for electrodeposition under diffusion control with overlapping hemispherical diffusion zones that extend to infinity was the Scharifker–Hills (S-H) model [7], where the experimental chronoamperometric curves are scaled by their maxima and the type of nucleation, whether instantaneous or progressive, could be deduced by comparing the scaled curves against theoretical ones given by the S-H model:

$$\frac{I^2}{I_{max}^2} = \frac{1.9542}{t/t_{max}} \left\{1 - \exp\left[-1.2564(t/t_{max})\right]\right\}^2 \quad \text{for instantaneous nucleation,} \tag{5}$$

$$\frac{I^2}{I_{max}^2} = \frac{1.2254}{t/t_{max}} \left\{1 - \exp\left[-2.3367(t/t_{max})^2\right]\right\}^2 \quad \text{for progressive nucleation.} \tag{6}$$

These two equations are plotted in Figure 7 along with a representation of growth of nuclei and diffusion zones in instantaneous nucleation. Multiple theoretical models have been built over the years to further explain the current behavior during electrodeposition processes. These improvements include adding a correction term to the S-H model [20], Heerman and Tarallo using Dawson's integral and physically relevant kinetic parameters [21], D'Ajello *et al.* restricting the diffusion zones to a limited region [22] and further refining of the limited diffusion following G. Luo *et al.* [23, 24]. In **Publication I**, the model developed by Heerman and Tarallo [21] was utilized to acquire three kinetic parameters of interest from the chronoamperometric curves. First, nucleation rate constant per site A

[s^{-1}] effectively describes how many new nuclei are created in an unit of time. Second, the number density of active sites N_0 [cm^{-2}] is the amount of active sites on an unit of electrode surface area. Lastly, diffusion coefficient D [cm^{2}s^{-1}] of the dissolved metal ions, the units of which describe the average surface area an ion's position spreads over time. These parameters can be extracted from the fitting parameters of the following expression for current density:

$$j(t) = zFDc\frac{1}{(\pi Dt)^{1/2}}\frac{\Phi}{\Theta}\left(1 - \exp\left[-\alpha N_0(\pi Dt)^{1/2}t^{1/2}\Theta\right]\right), \tag{7}$$

where

$$\Phi = 1 - \frac{\exp(-At)}{(At)^{1/2}}\int_0^{(At)^{1/2}} \exp\left(\lambda^2\right) d\lambda \tag{8}$$

$$\Theta = 1 - \frac{\left(1 - e^{-At}\right)}{At}, \tag{9}$$

with $\alpha = 2\pi(2MDc/\rho)^{1/2}$, c is bulk concentration of the metal precursor [mol/L], and M and ρ being the molar mass [g/mol] and density [g/cm^3] of the deposited metal, respectively. Purely mathematical integration variable λ is used in the non-elementary integral originating from the Dawson's function.

3 Hydrogen evolution reaction

In addition to electrodeposition, where the dissolved ions are reduced into solids, the products of electrochemical reactions can also be in gaseous form, as is the case in water electrolysis. In an electrolyzer cell, water molecules are electrochemically split into hydrogen and oxygen gases in their respective half-reactions. On the cathode side, hydrogen evolution reaction (HER) takes place where water molecules or H_3O^+ ions adsorb onto the cathode surface, charge transfer from the electrode to the reactant takes place, and reactant dissociates into OH^- ions or H_2O leaving behind adsorbed hydrogen H_{ads} atoms. An adsorbed hydrogen atom can recombine and desorb as hydrogen gas (H_2) with another H_{ads} or with a proton from the surrounding electrolyte. Simultaneously, on the anode oxygen gas is formed during oxygen evolution reaction (OER). Water electrolysis has seen limited use in producing hydrogen gas for over a century but its economic viability has only recently been demonstrated. Due to the tricky nature of the HER and OER, great progress is still being made in understanding the fundamental workings of these reactions and in using that knowledge to develop better catalysts. Especially the modern computational tools such as the ones based on density functional theory (DFT) have offered considerable insight into the detailed working processes of electrolyzers [25].

3.1 Thermodynamics

Water electrolysis in an electrolyzer has the overall reaction of

$$2\,\mathrm{H_2O} \rightarrow 2\,\mathrm{H}_{2,gas} + \mathrm{O}_{2,gas} \tag{10}$$

where H_2O molecules are split into hydrogen and oxygen gases. In standard conditions this reaction is not thermodynamically favorable, i.e. the initial water molecule has a lower Gibbs free energy G level than the end products. Thus, the change in Gibbs free energy ΔG is positive and the reaction does not occur spontaneously. ΔG is given as the change of enthalpy ΔH, which is the equal to the amount work required to break the chemical bonds plus the volumetric work done, minus the change in entropy ΔS, which measures how much the system's disorder increases as a function of temperature. Putting this together

$$\Delta G = \Delta H - T\Delta S. \tag{11}$$

For water electrolysis the change in enthalpy needed to break the water molecule bonds and form H_2 and O_2 molecules $\Delta H_{el} = +285.8$ kJ/mol, and $\Delta S_{el} = +0.0487 \frac{\mathrm{kJ}}{\mathrm{mol \cdot K}}$. In room temperatures the change in Gibbs free energy is

$$\begin{aligned} \Delta G_{el} &= \Delta H_{el} - T\Delta S_{el} \quad (12)\\ &= +285.8\ \frac{\mathrm{kJ}}{\mathrm{mol}} - 298\ \mathrm{K} \cdot 0.0487\ \frac{\mathrm{kJ}}{\mathrm{mol \cdot K}} \quad (13)\\ &= +237.2\ \frac{\mathrm{kJ}}{\mathrm{mol}}. \quad (14) \end{aligned}$$

Thus, this amount of external work must be supplied to the system in order to make water splitting thermodynamically favorable [26]. Of course, increasing the electrolyzer temperature makes the entropy term larger meaning that at high temperatures less external, non-thermal, work is needed for water electrolysis [27]. Gibbs free energy change can be related to the reversible cell potential E such that

$$\Delta G = -nFE, \tag{15}$$

where n is the number of transferred electrons. For water electrolysis $n = 2$ for each of the water molecules. In standard conditions this can be written as equilibrium potential E° for water electrolysis as

$$E^\circ = -\frac{\Delta G}{nF} = 1.23\ \mathrm{V}. \tag{16}$$

This represents the minimum voltage that is needed to make the water splitting thermodynamically favorable. To increase the reaction rates, most electrolyzers operate at higher potentials $E_{\mathrm{applied}} > E^\circ$ to overcome the charge transfer kinetic barriers and ohmic losses [28].

3.2 Kinetics

Reaction thermodynamics only determine whether or not a given reaction takes place spontaneously or not. However, the rate at which the reaction proceeds is also an important parameter. As an example, the corrosion of iron into rust is thermodynamically favorable ($\Delta G < 0$), but not all iron exposed to atmospheric

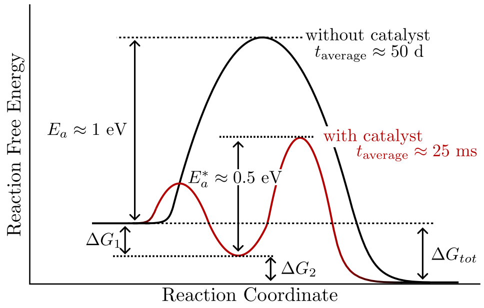

Figure 8. Chemical reactions are catalyzed by lowering the activation energy by introducing an intermediate state from which the activation energy to the end product is lower than the reaction without catalyst. Here the expected times to overcome the activation energy are reported for a single active site of the electrode surface. Author's own illustration based on [29].

oxygen immediately corrodes. This is due to the fact that the activation energies, i.e. energy barriers that must be overcome in order for the reaction to proceed are substantial and thus limit the overall reaction rate. Research in heterogeneous catalysis aims to increase the reaction rate by substituting one-step charge transfer reaction with large activation energy with two or more consecutive charge transfer steps that individually have lower energy barriers than the one-step reaction [30].

The basic operating principle of a catalyst is presented in Figure 8. The total change in Gibbs free energy ΔG_{tot} is the difference between the Gibbs free energy at the initial state G_i and final state G_f. When ΔG is negative, the reaction occurs spontaneously but activation energy barrier E_a needs to be overcome, generally by thermal motion of the reactants. As shown in the figure, the average time for the reaction to occur grows exponentially as a function of the activation energy and the reaction rate is slow when $E_a \approx 1$ eV. This changes with the addition of a catalyst that introduces an intermediate reaction state with a lower activation energy barrier $E_a^* \approx 0.5$ eV. Generally, the rate of the overall reaction is limited by the reaction step with the hightest activation energy. By introducing one or more intermediate steps, even if they have activation barriers of their own, the highest activation energy can be lowered, which can have drastic effects on the overall reaction rate [31].

Now, it needs to be noted that the use of catalyst materials shifts the chemical nature of the intermediate states, and while the catalyst participates in the charge transfer steps, it is not permanently altered when the reaction is finished. For water electrolysis these intermediate steps are found in the form of adsorbed states of hydrogen and oxygen species. The reaction product, H_2 molecule in HER, is released from the catalyst surface, enabling the catalyst surface to catalyze further reactions.

3.3 Hydrogen adsorption

When a potential above 1.23 V is applied between the electrodes of an electrolyzer cell, HER initiates on the cathode while OER starts on the anode. The hydrogen evolution reaction is characterized by three different steps. In the Volmer step, the protons are adsorbed and reduced into atomic hydrogen onto the catalyst surface, with the charge transfer being a fundamental factor to the Volmer step kinetics [32]. Following that, molecular hydrogen can be generated via two different pathways; in the Tafel step two adsorbed hydrogen atoms recombine into H_2, and in the Heyrovský step, one adsorbed hydrogen combines with a proton from the solvent into gaseous hydrogen [33]. These two pathways also vary based on the pH value of the electrolyte. The pH value describes the effective concentration of dissolved H^+ influenced by the proton activity in the solution and in a neutral electrolyte with pH 7 the H^+ concentration is 10^{-7} M (mol/L). As one can imagine, the concentration of charge carrying H^+ is of interest in water electrolysis. In strongly acidic conditions with nominal $\mathrm{pH} \approx 0$, the proton activity corresponds to an effective proton concentration in the order of 1 M. In these conditions the water electrolysis reaction is carried by the dissolved protons:

$$\text{Cathode reaction} \qquad 2\,\mathrm{H}^+_{aq} + 2\,\mathrm{e}^- \rightarrow \mathrm{H}_{2,gas} \tag{17}$$

$$\text{Anode reaction} \qquad 2\,\mathrm{H_2O} \rightarrow \mathrm{O}_{2,gas} + 4\,\mathrm{H}^+_{aq} + 4\,\mathrm{e}^- \tag{18}$$

In an acidic HER Volmer step, a proton is removed from the bulk water shell and is adsorbed to the cathode and reduced. Following that, in Volmer-Volmer-Tafel mechanism, another proton is adsorbed onto the electrode surface, which then proceed to combine and desorb as H_2 gas [34]. Alternatively in Volmer-Heyrovský mechanism, H_{ads} can receive an electron from the electrode and combine with H^+ from the electrolyte [34]. These reactions are generally written as:

$$\text{Volmer} \qquad \mathrm{H}^+ + \mathrm{e}^- \rightarrow \mathrm{H}_{ads} \tag{19}$$

$$\text{Tafel} \qquad \mathrm{H}_{ads} + \mathrm{H}_{ads} \rightarrow \mathrm{H}_2 \tag{20}$$

$$\text{Heyrovský} \qquad \mathrm{H}_{ads} + \mathrm{H}^+ + \mathrm{e}^- \rightarrow \mathrm{H}_2 \tag{21}$$

The overall Volmer-Volmer-Tafel and Volmer-Heyrovský mechanisms in an acidic electrolyte are illustrated in Figure 9.

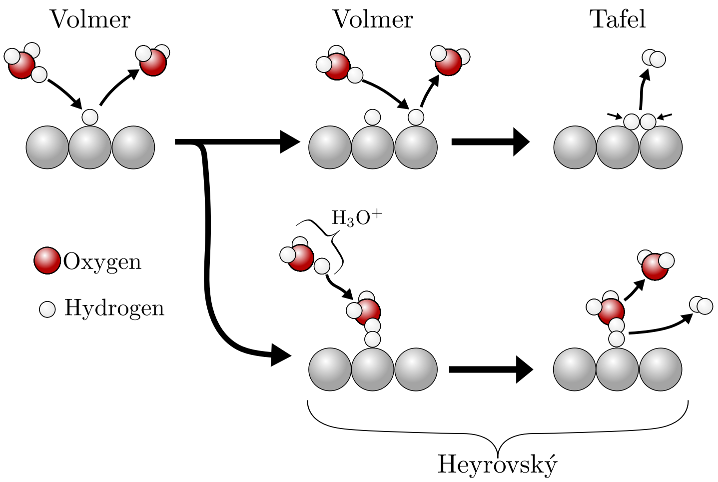

Figure 9. Two principle hydrogen evolution reaction mechanisms in an acidic environment. As its name implies, Volmer-Volmer-Tafel process is composed of adsorption of two hydrogen atoms which then recombine in to H_2 on the catalyst surface and desorb. Volmer-Heyrovský mechanism, on the other hand, has only one adsorption step and molecular hydrogen is formed between the H_{ads} and a dissolved electrolyte proton. Author's own illustration.

The HER process functions somewhat differently in alkaline pH 14 conditions due to the low effective concentration of free protons in the order of 10^{-14} M. In alkaline HER charge is transferred instead by the hydroxide ion OH^- and the electrode reactions change accordingly.

$$\text{Cathode reaction} \qquad 2\,H_2O + 2\,e^- \rightarrow H_{2,gas} + 2\,OH^-_{aq} \tag{22}$$

$$\text{Anode reaction} \qquad 2\,OH^-_{aq} \rightarrow \frac{1}{2}O_{2,gas} + H_2O + 2\,e^- \tag{23}$$

Now the protons for the HER are provided by the dissociation of the H_2O molecule during the Volmer step. Instead of simple proton adsorption, as is the case in acidic HER, prior to H_2O dissociation the water molecule itself must adsorb to the electrode surface and then dissociate into H^+ and OH^- [33]. In addition, the transfer of resulting hydroxide anions adds a further complication for the overall HER process. The HER mechanisms in alkaline environments are most commonly written as:

$$\text{Volmer} \qquad H_2O + e^- \rightarrow H_{ads} + OH^- \tag{24}$$

$$\text{Tafel} \qquad H_{ads} + H_{ads} \rightarrow H_2 \tag{25}$$

$$\text{Heyrovský} \qquad H_{ads} + H_2O + e^- \rightarrow H_2 + OH^-. \tag{26}$$

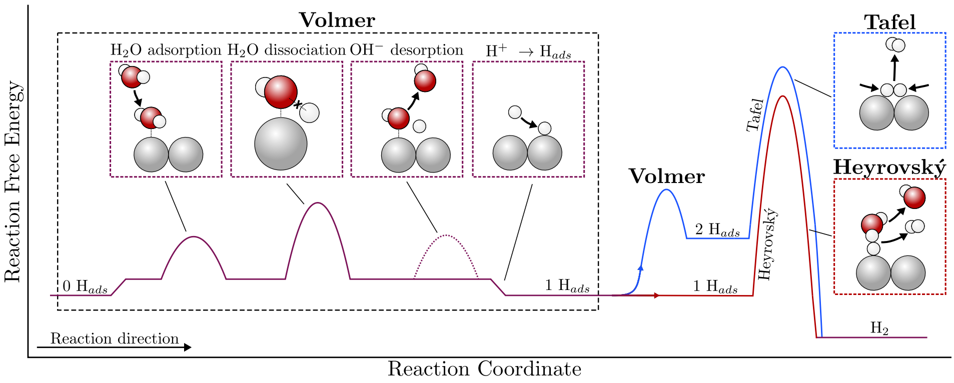

Figure 10. Free energy graph of Pt(111)-like surface Volmer-Volmer-Tafel (blue) and and Volmer-Heyrovský mechanisms in alkaline media where the Volmer step is more complex than in acidic media, requiring the adsorption and dissociation of H_2O molecules in addition to the simple hydrogen adsorption. Additionally, the OH^- ions must desorb during the HER reaction as to not inhibit H_2O adsorption. Author's own illustration based on data and description from [34, 36].

Free energy graphs of both mechanisms in alkaline conditions are presented in Figure 10. Each state along the reaction coordinates has its corresponding free energy and is separated by some activation energy from the next state. Volmer step consists of initial H_2O molecule adsorption followed by breaking of one of the O-H bonds, desorption of the hydroxide ion and the eventual energetically favorable H^+ adsorption and reduction. In the case of Heyrovský mechanism this is followed by the simultaneous dissociation and desorption of H_2O and H_{ads} into OH^- and H_2. In Tafel mechanism, a second proton is adsorbed in another Volmer step followed by the recombination of two H_{ads} and desorption of the resulting hydrogen molecule. The second Volmer step has a higher free energy than the first because high hydrogen coverage of the electrode surface inhibits the adsorption of additional protons [34–36].

3.4 HER bubble dynamics

Molecular hydrogen generated during HER forms gas bubbles that adhere to the cathode surface, grow as more hydrogen gas is evolved, and eventually detach from the surface into the bulk liquid. With higher current densities, these gas bubbles cover a significant portion of the electrode surface limiting the HER activity as less of the electrolyte is in direct contact with the electrode surface [37]. The dynamics of the electrolyte-electrode boundary region are made complex by

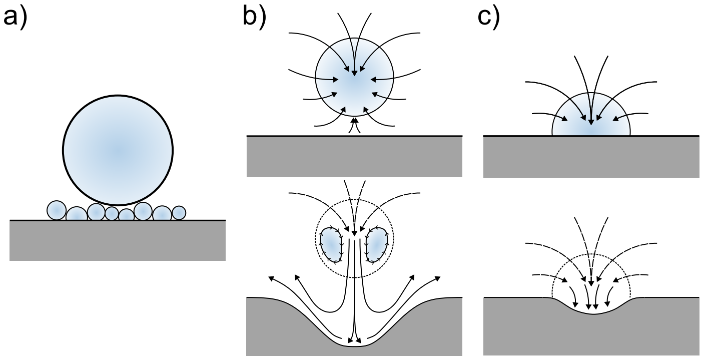

Figure 11. a) Nanoscale bubbles created during HER cover the electrode surface and proceed to coalesce into a microscale hydrogen bubble that is suspended on a nanobubble carpet [38]. b) Surrounding fluid rushes into the void left by the collapsing bubble. Fluid flow is impeded by nearby surfaces causing the far side of the bubble to collapse faster and resulting in jet formation. For a brief moment, the gas of the collapsing bubble is pressed into a toroidal shape while the jet impacts the surface damaging it. Fluid outflow after the initial impact further removes material. c) For high-contact angle surface bubbles, jet formation is interrupted prematurely by the surface resulting in a shallower damage profile and no added fluid outflow [39, 40]. Author's own illustration.

the time evolution of the gas bubbles. Initially, evolved gaseous hydrogen forms nanoscale bubbles, which grow and form a layer of nanobubbles. As the gas evolution proceeds, these nanobubbles coalesce into a microscale bubble suspended on top of the nanobubble layer. These microbubbles detach upon reaching critical dimensions [38]. Figure 11a shows a growing microbubble suspended on a nanobubble layer as would be the case in an electrolyzer.

Gaseous bubbles submerged in a liquid medium are subject to produce cavitation in their sudden collapse when the external fluid pressure exceeds the bubble's internal vapor pressure. High temperatures, shock waves and jet formation are associated with cavitation events [41]. Jets with peak velocities over 1 km/s are formed when the surrounding liquid rushes into fill the cavity of the collapsing bubble. Tangential fluid velocity on a solid surface is zero, resulting in a shear layer where lateral fluid velocities are lower than in the bulk liquid [42]. Due to the shear layer, the far side of the bubble collapses faster than the surface side, and a concentrated jet of fast flowing fluid moving toward the surface is created. Cavitation-induced jet impacts are known to induce mechanical damage on a wide range of materials [43]. Extent of the damage is dependent bubble collapse energy, jet velocity, and on the materials properties of the affected surface [44, 45].

In the case of nanoscale bubbles, the bubble collapse is generally not spontaneous, but rather are induced by shock waves or water hammer effects, such as the ones generated by collapse of nearby bubbles [46]. Bubbles generated during the HER on the electrode surface can either be spherical nanobubbles or surface nanobubbles, and they have their characteristic cavitation processes. Spherical nanobubbles have more time to develop their microjets before impacting on the electrode surface whereas for the surface nanobubbles the jet formation is not fully realized before impact. This leads to cavitation damage originating from the collapse of spherical nanobubbles to be generally deeper than damage originating from surface nanobubble cavitation on the same substrate [39]. The two nanobubble cavitation processes are visualized in Figures 11b and 11c.

3.5 HER catalysts

Hydrogen evolution reaction is limited by the slowest transition from one reaction state to the next. Typically, the Volmer step is the rate-determining step in the overall HER reaction and a lot of the catalyst research is spent on optimizing this step [47]. An ideal catalyst for the Volmer step would have high hydrogen binding energies meaning that the adsorption of hydrogen onto the catalyst would be extremely fast. Unfortunately, this has the side effect of making the recombination and desorption of adsorbed hydrogen more challenging during the Tafel and Heyrovský steps resulting in adsorption sites being blocked. As such, the best catalysts have hydrogen binding energies at just the right energy range as to expedite the Volmer step without inhibiting the desorption steps [48]. Additional considerations are required for HER catalysts in alkaline electrolytes as the dissociation of H_2O molecules is up to orders of magnitude slower than mere hydrogen adsorption.

For HER in acidic conditions, the ideal binding energies have been known for a long time to lie at the top of the Volcano plot presented in Figure 12a, where the exchange current density is plotted as a function of the metal–hydrogen bond strength for various metals. Fastest reaction rates are seen for catalysts near the top of the volcano plot with Pt-hydrogen binding energy value being close to the ideal one. This connection of HER rates and metal-hydrogen binding energies have been time and time again to be in good agreement with each other through computational and experimental works [49–51]. Despite this, the volcano plot's attempt to condense the complexity of catalytic reactions to a single descriptor, that of metal-hydrogen binding energies, leads to inaccuracies when considering kinetics of more complex reactions [52]. For instance, the hydrogen coverage

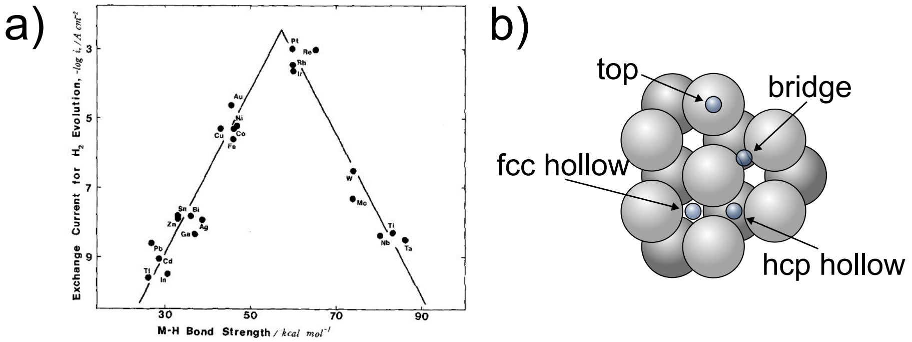

Figure 12. a) Volcano plot with exchange current density as a function of metal-hydrogen bond strength. The hydrogen binding energies for various materials are marked along the plot. Image reprinted with permission from [48]. Copyright 1972 Elsevier. b) On Pt(111) electrode surface, hydrogen can adsorb and/or diffuse to four distinct adsorption sites. When H_{ads} is found on top the Pt atoms, the site is logically known as an on-top site. The site between two Pt atoms is known as a bridge site. Lastly, when H_{ads} is found equidistant from three top layer Pt atoms, the site is either hcp hollow site or fcc hollow site, depending on whether the site is located directly above an second-layer Pt atom, or not, respectively. Figure adapted from **Publication III**.

and the specific sites of adsorbed hydrogen affect the water molecule orientation near the surface, significantly altering the transport of protons from the solvent side to the surface [53]. Additionally, due to the catalyst materials often being scarce noble metals, the use of bulk (surface) binding energies is inaccurate for real catalysts because it is not economically viable to use e.g. platinum in bulk quantities. In catalyst research, nanoscale structures are used to reduce the amount of required noble metals, and at nanoscales the effect of the surfaces is greatly magnified, rendering volcano plots less accurate.

In nanoscale structures the specific local environment of an adsorption site causes the nanoparticle to have wildly different properties to its bulk counterpart. Some materials with poor catalytic properties in bulk might be excellent catalysts when manufactured into nanoparticles with appropriate shape, crystal facets and size. Even for platinum, the HER process has been noted to be greatly affected by the crystal facet of the catalyst surface. For Pt(110) surface the reaction proceeds via the Volmer-Volmer-Tafel pathway but Volmer-Heyrovský pathway dominates on Pt(100) surface, and additionally both pathways have historically been suggested to dominate on Pt(111) surface in the literature [54]. The rate-determining step for HER on Pt(111) has been explained by density functional theory calculations to commonly be Volmer-Volmer-Tafel but despite this direct observation of the HER environment has been noted to be necessary to fully connect simulations and experimental results for these kinds of systems [50, 55]. There are multiple experimental works that have directly characterized hydrogen adsorption on Pt(111), such as Kunimatsu *et al.* [56] using surface-enhanced IR absorption spectroscopy (SEIRAS), Nanbu *et al.* [57] by the ways of Fourier-transform infrared reflection absorption spectroscopy (FT-IRAS) and Chang *et al.* [58] with surface enhanced infrared and Raman spectroscopies, which will be discussed more thoroughly in Chapter 8. However, to the best of the authors' knowledge, **Publication III** presented the first instance of electron paramagnetic resonance being used *in situ* to characterize the coordination number of adsorbed hydrogen and Pt atoms, offering insight into the adsorption site occupancies in the hydrogen underpotential deposition region, i.e. at potentials above the onset of hydrogen evolution.

4 Electron paramagnetic resonance

In **Publication III** electron paramagnetic resonance (EPR) spectroscopy was used to examine the adsorption of hydrogen on Pt(111) surface to probe its adsorption sites. EPR spectroscopy is based on splitting the spin states of unpaired electrons in a magnetic field and observing the different energy levels by changes in absorbance of electromagnetic waves. The basic operating principle is similar to nuclear magnetic resonance (NMR) spectroscopy with the distinction that whereas in NMR the spin energy states of atomic nuclei are probed, EPR only contends with valence electrons of atoms and molecules. This section outlines the basic operating principles of EPR spectroscopy based on two textbooks by Bertrand [59] and by Goldfarb and Stoll [60], and briefly summarizes how EPR has been used in electrochemical systems.

4.1 Electron spin states

Electrons are fundamental particles with three characteristic properties; mass m_e, electric charge q_e and spin. Of these properties, spin is the most challenging to describe accurately. It takes the form of intrinsic angular momentum, which could be understood as the electron spinning along an arbitrary axis, and even if this approach is not physically completely accurate, it serves as reasonable intuition for the purposes of this chapter [60]. Electron spin angular momentum S can only have two discrete values:

$$S = \pm\frac{\hbar}{2} = \pm\frac{1.05457 \cdot 10^{-34}\ \mathrm{J \cdot s}}{2}, \tag{27}$$

where $\hbar$ is the reduced Planck's constant. As spin can only have discrete values, it is said to be quantized, and thus given its corresponding half-integer spin quantum number $m_s = \pm\frac{1}{2}$ marking it as a fermion. Now, electrons are affected by magnetic fields and the magnitude of the torque an electron experiences is given by the electron magnetic moment μ as

$$\mu = g_e \frac{q_e \hbar}{2m_e} m_s = g_e \mu_B m_s, \tag{28}$$

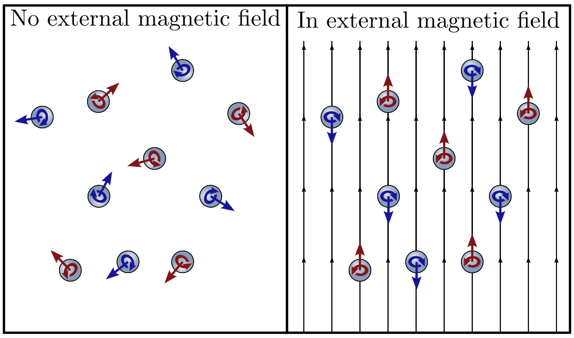

Figure 13. Without an external magnetic field electron spins are randomly oriented but when a magnetic field is applied, the electrons orient themselves parallel (spin-up) or antiparallel (spin-down) with respect to the local magnetic field. Author's own illustration.

where g_e is the free electron g-factor, which is effectively a correction term for quantum mechanical objects and will be described in greater detail later, and $\mu_B = \frac{q_e \hbar}{2m_e}$ is known as the Bohr magneton [60]. Electrons in an external magnetic field experience a torque that aligns them either parallel or antiparallel with respect to the magnetic field lines. This is illustrated in Figure 13. Electrons with $m_s = +\frac{1}{2}$ align themselves parallel to the magnetic field and are said to be in spin-up $\uparrow$ state, whereas electrons with $m_s = -\frac{1}{2}$ align antiparallel with respect to the magnetic field into so called spin-down $\downarrow$ state [59].

On their own these two spin states have the same energy, but when an external magnetic field, traditionally along the z-axis, is applied and the electrons align according to their spins, it is seen that the energies of the spin-up and spin-down states differ from each other. The antiparallel $\downarrow$-state will have a lower energy level in an external field than with zero magnetic field whereas the parallel $\uparrow$-state has a higher energy level [60]. The energy difference between the states is directly proportional to the strength of the magnetic field B_z:

$$\Delta E = g_e \mu_B B_z. \tag{29}$$

Electrons can move from one energy level to another, i.e. their spin states can be flipped. An electron can be excited from the lower energy spin-down state to the higher energy spin-up state by absorbing a photon with energy $h\nu$, where ν is the photon frequency, matching to ΔE as shown in Figure 14a. Similarly an electron's spin can flip from spin-up state to spin-down state by emitting a photon with the same wavelength [59].

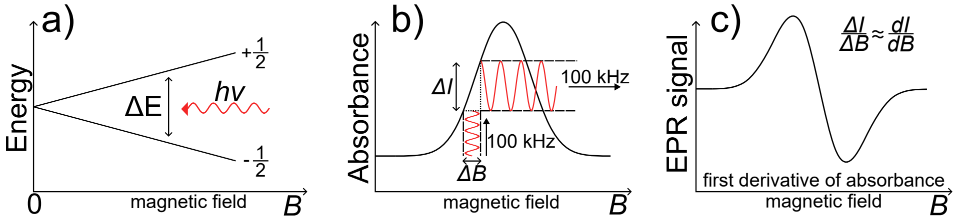

Figure 14. a) As the magnetic field strength is increased, the energy levels of the two electron spin states split. Electrons can flip their spin by absorbing or emitting a photon with wavelength matching the energy separation. b) Signal-to-noise ratio is improved by modulating the magnetic field strength during the sweep at a set frequency and setting the microwave detector to measure only at that frequency. c) Recorded $\frac{\Delta I}{\Delta B}$ is effectively the first derivative of absorbance. Adapted from **Publication III**.

Operation principle of EPR spectroscopy is that electromagnetic radiation at specified wavelength, generally in microwave range, is introduced into the EPR chamber and its absorbance is recorded while the magnetic field strength B_z is swept from initial B_i to final B_f value. When B_z is such that the resonance condition $g_e \mu_B B_z = h\nu$ applies, some of the microwaves are absorbed by the spin-down electrons, which are flipped to spin-up state, and this is observed as absorbance of the microwave radiation [59]. In practice, the signal-to-noise ratio of an EPR measurement is increased by applying a modulation to the sweeping magnetic field at a specific frequency, commonly 100 kHz, and this produces a close approximation of the first derivative of the absorbance instead [60]. With the use of frequency modulation any true signal arising from the chamber must also be at the modulation frequency meaning that signals at any other frequencies can be filtered out by the microwave detector [61]. This has been illustrated in Figures 14b and 14c.

Now, the question arises that don't the excited electrons relax quickly and emit a microwave photon at the same wavelength as the incident photon leading to net-zero microwave absorption? This indeed happens in an EPR chamber, electrons are absorbing and emitting photons constantly and preserving the average number of electrons in either spin state. As it happens, without an externally applied magnetic field, the probability of finding a given electron either in spin-up or in spin-down state is equal as their energy levels are the same. However, as the energy levels split when an external magnetic field is applied, thermodynamics dictate that any one electron is more likely to be found in the lower energy spin-down state. For a large collection of electrons in thermodynamic equilibrium, this is seen as the electrons being distributed to the energy states following

Boltzmann statistics [62]. The relative abundance of electrons in spin-up and spin-down states can be given as:

$$\frac{n_\uparrow}{n_\downarrow} = e^{-\frac{\Delta E}{k_B T}} = e^{-\frac{h\nu}{k_B T}}, \tag{30}$$

where k_B is the Boltzmann constant and T is the absolute temperature [62]. For a common EPR measurement at 9.5 GHz where $\Delta E \approx 40\ \mu\mathrm{eV}$, the relative abundance has the value of $\frac{n_\uparrow}{n_\downarrow} \approx 0.9984$ meaning that out of 10 000 electrons, approximately 4992 will be in spin-up state and 5008 will be in the spin-down state [63]. With this it's clear that there are more electrons that can absorb a photon than there are electrons that emit one, which leads to the observed overall microwave absorption.

4.2 Paramagnetism

Electrons are, however, generally not observed in isolation but rather as constituents of atoms and molecules where they are arranged on orbitals according to Pauli exclusion principle, which states that no two fermions, i.e. particles with non-integer spins, can occupy the same quantum state. For electrons, this means that any unique orbital can only have up to two electrons provided they have the opposite spin quantum numbers. Any such ”filled” orbital has no overall magnetic moment as the spin magnetic moments of the two electrons sum up to zero [64]. The presence of unpaired electrons is the prerequisite to EPR spectroscopy as paired electrons can't independently change from one spin-state to another on their orbital as then the two electrons would have to exist in the same quantum state. In equilibrium state, orbitals with paired electrons include all inner atomic or molecular orbitals and very commonly even the valence molecular orbitals [59]. Additionally the band structure of metals can have all the electrons effectively paired up [65]. Nevertheless, a great number of materials exhibit paramagnetism, i.e. overall magnetic moment, which arises from orbital(s) with unpaired electrons that when exposed to an external magnetic field align with (parallel) or against (antiparallel) the field providing a net magnetic moment. Orbitals with unpaired electrons can be found in individual atoms such as hydrogen, lithium and oxygen, or in molecules [59]. Any molecules with an odd number of electrons necessarily have an unpaired electron making them highly reactive radicals, such as $OH^\bullet$ and $NO^\bullet$, and have strong responses in EPR spectra [66, 67]. On the other hand, molecules with even number of electrons generally lack unpaired electrons with a few notable exceptions. For instance, the O_2 molecule has two unpaired electrons in ground state on different orbitals, i.e. it has a triplet state. Oxygen molecules have an exceptionally noticeable EPR response [68].

4.3 Hyperfine coupling

EPR would be relatively uninteresting characterization method if observations would be limited to only providing evidence of free or unpaired electrons in some systems. Fortunately, additional information is obtained by measuring how the magnetic moments of the atomic nuclei interact with the electrons giving rise to hyperfine coupling. As the constituents of atomic nuclei, protons and neutrons, are both fermions with half-integer spins, also they have their inherent spin magnetic numbers $m_p = \pm\frac{1}{2}$ and $m_n = \pm\frac{1}{2}$ [59]. When they form atomic nuclei, their spin magnetic moments can bestow the resulting nucleus with a total nuclear angular moment I. With an even number of nucleotides I is an integer or zero whereas with an odd number of nucleotides $I = \frac{n}{2}$, where $n = 1, 2, 3, ...$ This leads to different isotopes of an element having their unique responses to EPR through spin magnetic moment of an electron being coupled with the total angular magnetic moment of the nuclei in its vicinity [60]. As a result the electron energy levels are split further. This is illustrated in Figure 15. Let us consider one electron coupled with one hydrogen nucleus where $I = \frac{1}{2}$. In this system hyperfine splitting is observed as now there are four different energy levels corresponding to four electron-nucleus pairs. There are two possible electron spin transitions at different ΔE, which is observed in an EPR spectrum as splitting of the absorption peak into two peaks with similar intensity. Coupling the electron with an additional proton forming a H_2^+ ion further splits the energy levels, this time into three. There are now four possible proton spin configurations between them, either they are aligned with both protons in spin-up state $\uparrow_{p_1}\uparrow_{p_2}$ with $m_I = +1$, spin-down state $\downarrow_{p_1}\downarrow_{p_2}$ with $m_I = -1$, or misaligned in mixed states $\downarrow_{p_1}\uparrow_{p_2}$ or $\uparrow_{p_1}\downarrow_{p_2}$ both of which have $m_I = 0$. The two mixed states have the same energy and thus only three transitions are possible. However, it must be noted that all four proton spin configurations are equally likely, therefore the abundance of the mixed state energy level is twice that of either aligned state causing the absorbance of the central peak to be twice as large [62]. The hyperfine splitting caused by one or more atomic nuclei has characteristic responses to EPR based on the number of nuclei and, more importantly, their angular moments allowing the identification of specific structures. Knowledge of nuclear angular moments and the natural isotope ratios play a key role in the hyperfine splitting observed in real-life samples.

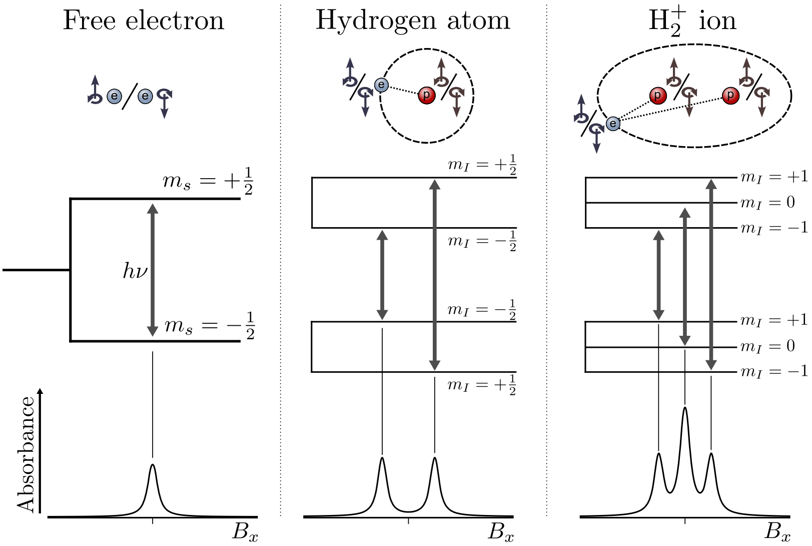

Figure 15. Free electrons in a magnetic field have two spin energy levels and only possible transition between the states is between electron spin-up and spin-down states resulting in a singular absorption peak. Bound to a hydrogen atom, the proton's magnetic moment couples with the electron spin magnetic moment, splitting the free electron energy states based on the nuclear spin alignment thus allowing for two distinct transitions, which are observed as two absorption peaks on both sides of the free electron transition energy. Coupling the electron further, with e.g. another hydrogen atom, further splits the energy levels, this time into a triplet. Author's own illustration based on [59] and [60].

4.4 g-factor

Earlier when presenting the spin magnetic moment of an electron, the g-factor term was added to correct for the fact that the experimentally observed electron magnetic moment differs from the classically calculated electron magnetic moment. For an unbound electron, the free electron g-factor g_e has been measured extremely precisely to the value $g_e = 2.00231930436082(52)$ [69]. Adding to this, a bound electron can have angular momentum based on its atomic orbital. Different orbitals are associated with their respective magnetic quantum numbers m_l. Electrons on spherical s-orbitals, where $m_l = 0$, have no orbital angular momentum but on p-orbitals ($m_l = -1, 0, +1$), d-orbitals ($m_l = -2, -1, 0, +1+2$), and f-orbitals ($m_l = -3, ..., 0, ..., +3$) impart their electrons a quantized orbital angular momentum. The torque experienced due to the orbital movement of charge is given by the orbital magnetic moment

$$\mu_L = g_L \mu_B m_l. \tag{31}$$

Here an orbital g-factor g_L must be added [63]. In a perfectly classical case, where the mass of the nucleus is infinite, $g_L = 1$, and $g_L \approx 1$ with nuclei of the heavier elements [70]. In lighter elements or when the electronic environment effectively changes the the orbital angular moment, the effect is seen in changes to g_L.

The orbital magnetic moment of the electron is coupled with its spin magnetic moment, i.e. the total magnetic moment μ_J of an electron is the sum of these two quantized magnetic moments, and similarly the total electron g-factor $g_J = g_e + g_L$, given as:

$$\mu_J = \mu_B(g_e m_s + g_L m_l) = g_J \mu_B(m_s + m_l). \tag{32}$$

This gives the energy of an electron with magnetic moment μ_J in an external magnetic field as

$$\begin{aligned} E &= \mu_J B_z && (33) \\ &= g_J \mu_B B_z(m_s + m_l) && (34) \end{aligned}$$

and the energy difference between spin-up ($m_s = +\frac{1}{2}$) and spin-down states ($m_s = -\frac{1}{2}$) is

$$\begin{aligned} \Delta E &= E_{+\frac{1}{2}m_s} - E_{-\frac{1}{2}m_s} && (35) \\ &= g_J \mu_B B_z \underbrace{\left[(+\frac{1}{2} + m_l) - (-\frac{1}{2} + m_l)\right]}_{=1} && (36) \\ &= g_J \mu_B B_z. && (37) \end{aligned}$$

Now, when the scanning the magnetic field strength, absorbance peaks are observed when the resonance condition $\Delta E = h\nu$ achieved at a specific B_z [59]. The total electron g-factor for that peak is then determined by

$$g_J = \frac{h\nu}{\mu_B B_z}. \tag{38}$$

With that, Equation 38 gives the g-factor of absorbance peak at some magnetic field strength B_z because microwave photon is kept constant.

In EPR spectroscopy, the total magnitude of g-factor is measured and as g_e can be assumed to stay constant, any deviation from the free electron g-factor value can be attributed to the electrons gaining or losing angular momentum through their orbital interactions. Absorption peaks of paramagnetic species have their unique g-factors so that knowledge in combination with the hyperfine coupling can be used to identify paramagnetic species or intermediates [59]. As the g-value is affected by the electronic environment in the vicinity of the paramagnetic species, their locations can be deduced from the g-factor values. Similarly, the electron delocalization is seen as an increase in the g-factor [60]. Finally, in some materials the atoms and their orbitals might be preferentially oriented leading to magnetic anisotropy and possibility of resolving different atomic orientations [60].

4.5 EPR in electrochemistry

From 1960's to 1990's EC-EPR was quite frequently used in electrocatalysis research to examine reaction mechanisms, in identification of paramagnetic radical species and to elucidate the kinetics parameters of electrode reactions. Later, however, EC-EPR yielded much of its domain to often more accessible and versatile techniques, such as FTIR, UV-VIS and Raman spectroscopies [71]. One of the great limitations for the use of EPR in electrochemical systems, is that any mass inside the EPR chamber, and especially water, lead to considerable dielectric losses in the microwave frequency range. Because of this, *in situ* EC-EPR cells have to be designed to function at very low surface areas and electrolyte volumes, which of course induces challenges in the electrochemical characterization of the system, and in the fact that the concentration of any paramagnetic species generated inside the cell can become too low to be detected [71, 72]. Depending on the microwave frequencies used, and the amount and type of cell materials, the maximum cell diameters range from 10 mm for X-band (9.5 GHz) spectrometers to 0.8 mm for W-band (95 GHz) spectrometers [71]. In addition to the limited volumes, and hence concentrations, the transient nature of many of the paramagnetic reaction intermediates of interest, such as oxygen-group or organic radicals and adsorbed states of hydrogen, further complicates their detection [73, 74]. In recent years, other forms of EPR, such as high field EPR and pulsed EPR, have been introduced to the electrochemical research community along with a new operando film-electrochemical EPR technique that largely solves the challenges involved with low sample volumes of earlier EPR techniques [71, 74]. Due to its relevancy to **Publication III**, the detection of adsorbed hydrogen must be discussed a bit further. A common approach to detect paramagnetic intermediates or adsorbed hydrogen is by employing spin-trapping agents, which are diamagnetic molecules that bind to the shortly-lived species of interest and produce a more persistent species that then detected using EPR. For instance, the surface concentration of adsorbed hydrogen generated on carbon-deposited palladium nanoparticles has been quantified using this approach [73]. Alternatively, the radicals can be stabilized by performing the experiments in cryogenic conditions or by freeze-quenching the system [71, 74]. Generally speaking, direct, site-sensitive detection of H_{ads} on metal electrocatalyst surface with potential control, in non-cryogenic temperatures, has not been achieved with EC-EPR systems, and specifically this has been done addressed in **Publication III**.

5 Experimental

Detailed descriptions of materials used in experiments are given in **Publications I**, **II** and **III**, respectively.

5.1 Ag and Pd electrodeposition

5.1.1 Cyclic Voltammetry

In **Publication I**, the electrodeposition of the active species, palladium and silver, for catalyst nanoparticle production in H_2O, D_2O and acetonitrile (MeCN), as shown in Table 1, on pencil graphite was investigated by recording polarization curves with cyclic voltammetry. Potential was cycled at 50 mV/s between +0.6 V and -0.6 V with respect to a self-made aqueous 3 M KCl Ag/AgCl reference electrode. The cell construction is shown in Figure 16. Solutions were deaerated with nitrogen gas for at least 30 minutes before the measurement in order to remove any dissolved oxygen from the cell. From the voltammograms it was possible to determine the approximate potential region where the electrodeposition of the active species took place. As a result, these potential regions were examined more thoroughly with chronoamperometry. Unless otherwise noted, the potentials were converted to overpotential scale by subtracting measured equilibrium potentials in Table 1 from the potential measured vs the Ag/AgCl RE.

Table 1. The different liquid samples used in the experiments and their equilibrium potentials with respect to 3 M KCl Ag/AgCl reference electrode. *For $AgNO_3$ in MeCN, the crossover potential where forward return scans intersect was taken as E_{eq}. Table from **Publication I**.

Active species	c [mM]	Supporting electrolyte	c [mM]	Solvent	E_{eq} [mV]
$AgNO_3$	1	NaCl	3000	H_2O	6
$AgNO_3$	1	NaCl	3000	D_2O	3.3
$AgNO_3$	1	$LiClO_4$	100	MeCN	-27*
$PdCl_2$	1	NaCl	3000	H_2O	24
$PdCl_2$	1	NaCl	3000	D_2O	26

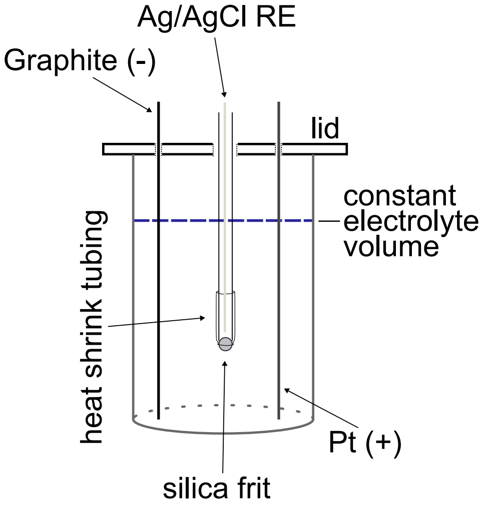

Figure 16. In **Publication I**, pencil graphite rods were inserted into the cell through a hole in the lid. A self-made Ag/AgCl reference electrode was used along with a Pt counter electrode to deposit dissolved Pd or Ag on the graphite surface in various electrolytes. The pencil graphite was exchanged after each individual chronoamperometric measurement and its surface area was controlled by using a constant electrolyte volume and by having the graphite rod make contact with the glass container bottom. Author's own illustration.

5.1.2 Chronoamperometry

Palladium and silver were electrodeposited on the pencil graphite electrodes by applying a potential step deviating from +0.6 V to some potential E_d and back to +0.6 V vs the reference electrode. The initial and final potentials were applied for 30 seconds each and the step potential was applied for 10 seconds. At a longer step durations, convective effects would disturb the otherwise diffusion-controlled system. The potential steps were chosen from the region of cathodic peaks in the sample's respective voltammogram. Pencil graphite rods were replaced with new ones after each potential step measurement.

5.1.3 Scanning Electron Microscopy

Surface morphologies of the Ag and Pd deposits were examined with scanning electron microscopy (SEM) for selected active species and deposition potential combinations. Electrons were accelerated with 2 kV acceleration voltage at a flux of 25 pA. Elastically scattered electrons of the incident beam were detected using a T1 backscattering detector. Backscattered electrons provide information on the atomic number of the sample atoms because heavier elements are more likely to scatter electrons elastically, thus giving rise to contrast in the SEM images between the lighter elements, such as carbon, and heavier electrodeposited metals [75].

5.2 CR-39 damage in electrochemical environments

Experimental work performed over two year in **Publication II** was composed of three main measurement sets. Each measurement set was focused on characterizing CR-39 polymer's response to different potentially damage inducing mechanisms. In the first measurement set, the palladium-electrodeposition (PdE) began by reproducing earlier palladium-hydrogen/deuterium co-deposition experiments reported in literature [76–79]. The second, recombination cell (RCC), measurement set consisted of experiments into CR-39 damage characterization when exposed to recombination of hydrogen and oxygen gases and its response to free radicals. Finally, the polymer cavitation damage (PCD) measurement set investigated the effect of ultrasound-induced cavitation to CR-39.

5.2.1 CR-39 polymer

Poly(allyl diglycol carbonate), CR-39 is a transparent plastic commonly used in corrective lenses and as a solid state nuclear track detector (SSNTD). CR-39 is a highly cross linked polymer network of its monomers, depicted in Figure 17a [80]. As a SSNTD, CR-39 operation principle is relatively simple. When exposed to energetic particles, such as alpha radiation, the particles break polymer chains along its flight path leaving a latent track [81]. After exposure, the CR-39 detectors are etched in highly alkaline solution during which the material is etched preferentially along the latent track. As a result, a micrometer scale conical track is formed, which can be observed with optical microscopy. This is illustrated in Figure 17b. Thus CR-39 is able to measure not only individual particles over extended periods of time but the track dimensions carry information about the incident particles themselves. Tracks produced by ^{241}Am source and their diametral distribution in **Publication II** are presented in Figures 18a and 18b, respectively. In addition to alpha particles, CR-39 can be used to detect protons [82], and with the use of proper pretreatments also neutron radiation [83, 84] and X-ray detection [85] is possible.

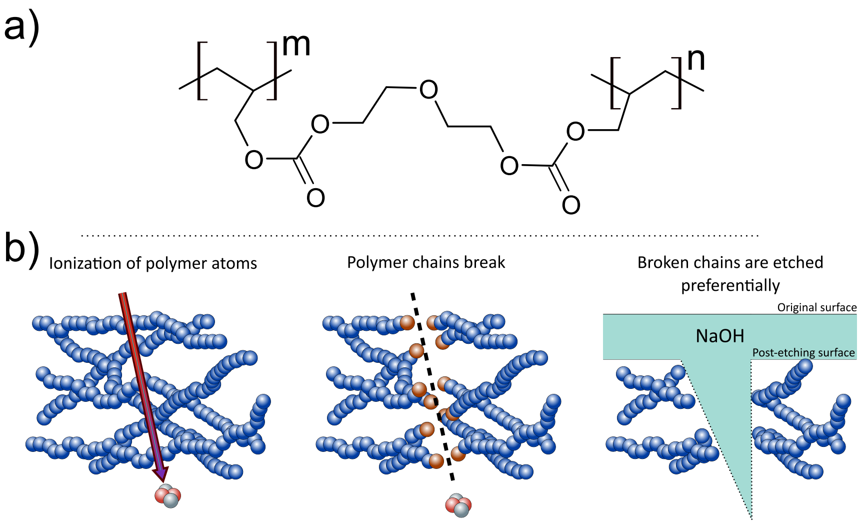

Figure 17. a) Polymer structure of CR-39. b) Energetic alpha particle ionizes atoms of the CR-39 polymer chains breaking them. The resulting latent track is preferentially attacked when etched with an alkaline etching solution forming a conical track where the particle had passed. The dimensions of the track and the knowledge of the etching rates can be used to determine incident particle energies. Author's own illustration based on [86].

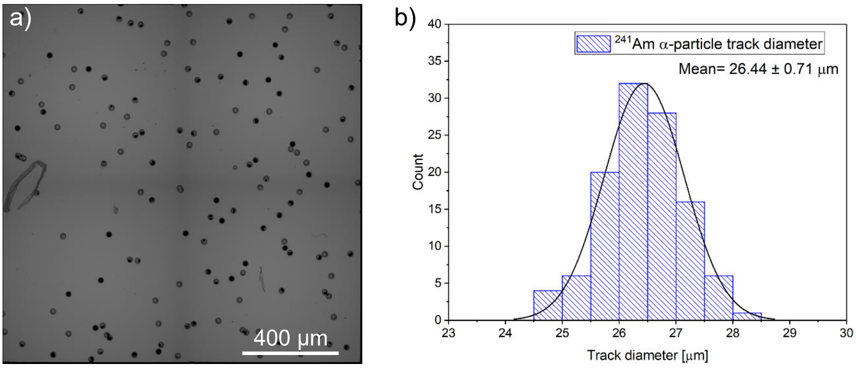

Figure 18. a) Tracks produced by ^{241}Am alpha particles after etching. b) Track diameters are normally distributed with around 26 µm average diameter. Figure from **Publication II**.

In the experimental work, the etching of the CR-39 detectors after a given experiment was performed within 48 h of the conclusion of the experiment. Detectors were etched by preparing a 5 M NaOH solution divided into narrow glass vials, diameter chosen so that the CR-39 pieces stay upright, partially submerged into silica oil heat bath which was then heated to 85 °C. After the etching solution had reached the desired temperature, CR-39 pieces were inserted into the their respective vials for 180 minutes, after which they were flushed thoroughly with tap water followed by distilled water before being gently tapped with technical wipes to dry them. Etched detectors were then stored in glass vials.

Detectors were initially imaged shortly after the etching process with optical microscopy. Smaller selection of detectors were imaged with a scanning 3D microscope. Track diameters were analyzed using Fiji software [87] and Image-J-Particle-detection-and-analysis macro [88].

5.2.2 Electrodeposition experiments

The first cell design used in PdE experiments is depicted in Figure 19a. Silver wire with 0.25 mm diameter was used as the working electrode and placed on top of the CR-39 pieces, which had been cut to ca. 1 cm by 2 cm dimensions. Nylon monofilament fishing line with 0.3 mm diameter was used to tie the Ag wire and the CR-39 to the polycarbonate support following the instructions in Mosier-Boss *et al.* [78]. Orientation of the detector was marked by scratching a small arrow at the top right corner of the detectors. Heat shrinking tubing was used to insulate the Ag wire on the support backside from the electrolyte. This cell design was later replaced with the 3D-printed (PLA) one presented in Figure 19b in order to simplify the cell assembly and to ease the utilization of protective films between the working electrode and the CR-39 piece. For the counter electrode, a coiled 0.5 mm diameter platinum wire with approximate surface area of 1.6 cm^2 was used. A few experiments used a dimensionally stabilized anode (DSA) composed of a titanium mesh with 8.5 cm^2 surface area coated with ruthenium and iridium oxides. All electrodes were washed in 10% nitric acid solution and rinsed with deionized water before being inserted into the cell. Two experiments utilized an H-cell with two 30 mL chambers separated by a Nafion-117 membrane.

Electrolytes were based on either deionized H_2O or 99.8% pure D_2O. Different metallic salts at 30 mM concentration were used as the active species. These include $PdCl_2$, $CuCl_2$, $PtCl_2$ and $Pd(NO_3)_2$ hydrate. Supporting electrolytes consisted of LiCl, KCl or $LiNO_3$ at 300 mM concentration. Cell and electrolyte

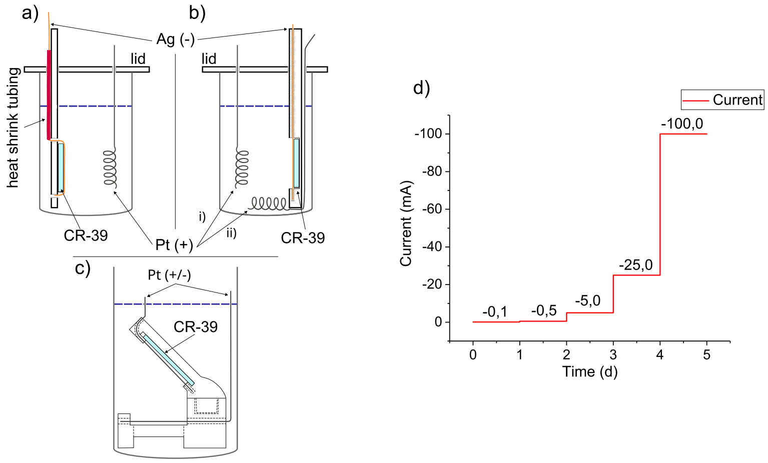

Figure 19. a) Initially CR-39 pieces were attached to a polycarbonate support with monofilament fishing line that also kept the Ag WE in contact with the detector surface. Heat shrink tubing was used to prevent deposition on the support backside. b) 3D-printed cell design simplified the cell assembly by eliminating the fishing line and heat shrink tubing with the added benefit of allowing the CE being placed underneath the working electrode. c) In investigating the recombination of hydrogen an oxygen gas bubbles, a third 3D-printed cell design was utilized, with the CR-39 surface being angled allowing the examination of WE-CE distance effects. Figure from **Publication II**. d) Cathodic current profile over the experimental period in PdE-experiments. Figure adapted from author's poster presented in International Society of Electrochemistry Regional Meeting, August 2022 in Prague, Czech Republic.

parameters used in PdE measurement set are presented in Table 2. A given experiment consisted of one to three individual cell replicates and often these experiments were performed in tandem with their control experiments. For example, PdE-001 and PdE-002 were otherwise identical with three cells marked with A, B and C each, except that PdE-002 electrolyte was based on D_2O rather than H_2O. Samples of the electrolytes before and after the experimental period were collected for later inductively coupled plasma mass spectrometry (ICP-MS) measurements into the electrolyte isotope contents.

Measurements in PdE measurement were carried out with a battery cycler in constant current mode, closely following the current profiles introduced by Mosier-Boss *et al.* [78]. The overall experiment duration was 120 hours where the current was increased in steps every 24 hours. The current profile used is shown in Figure 19d. Low initial currents were used to ensure stable deposition of the metal deposit without interference from gas evolution bubbles at higher currents. Final 100 mA current was often not achieved due to the low effective surface areas of the electrodes and the ohmic losses, and the 5.25 V potential limit of the Landt

Table 2. Experiment codes, electrolyte compositions and experimental parameters for the PdE measurement set. In twin experiments, differences in parameters between two cells are marked with boldface font, with other parameters being identical. Abbreviations used in the table: OPF – Original protective film, KPF – Kapton Polyimide film, 3DC – 3D-printed cell with the CE in either i) or ii) position of Figure 19b. Table from **Publication II**.

Exp. No.	Electrolyte [30 mM]	Supp. elec. [300 mM]	Solvent [50 mL]	Additives and conditions	No. of cells
PdE-001/**2**	$PdCl_2$	LiCl	$H_2O/\mathbf{D_2O}$		3/**3**
PdE-003/**4**	$CuCl_2$	LiCl	$H_2O/\mathbf{D_2O}$		3/**3**
PdE-005/**6**	$PdCl_2$	KCl	$H_2O/\mathbf{D_2O}$		3/**3**
PdE-007/**8**	$PdCl_2$	LiCl	D_2O	DSA CE, thermometer -/**0.1 mM** $\mathbf{PtCl_2}$	3/**3**
PdE-009/**10**	$PtCl_2$	LiCl/**LiCl***	$H_2O/\mathbf{D_2O}$	-/**10 mM** $\mathbf{D_2SO_4}$	1/**2**
PdE-015	$PdCl_2$	LiCl	D_2O	OPF, thermometer	3
PdE-016	$PdCl_2$	LiCl	50:50 H_2O/D_2O		1
PdE-017/**18**	$PdCl_2$	LiCl	$H_2O/\mathbf{D_2O}$	KPF	3/**3**
PdE-019	$PdCl_2$	LiCl	D_2O	Stirring	3
PdE-020/**22**	$PdCl_2$	LiCl	D_2O	KPF, 3DC(i)	3/**3**
PdE-021	$PdCl_2$	LiCl	D_2O†	H-cell, DSA CE	1
PdE-023	$PdCl_2$	LiCl	D_2O†	H-cell	1
PdE-024	$PdCl_2$	LiCl	D_2O	RE, 3DC(i)‡	3
PdE-025/**26**	$PdNO_3$	$LiNO_3$	$H_2O/\mathbf{D_2O}$	3DC(i)	3/**3**
PdE-027/**28**	$PdCl_2$	LiCl	$H_2O/\mathbf{D_2O}$	3DC(ii)	3/**3**
PdE-029/**30**	$CuCl_2$	LiCl	$H_2O/\mathbf{D_2O}$	3DC(ii)	3/**3**
PdE-031/**32**	$CuCl_2$	LiCl	$H_2O/\mathbf{D_2O}$	1 mM $PtCl_2$, 3DC(ii)	3/**3**

*In PdE-010 LiCl concentration was 1 M.

†30 mL volume per chamber, CE side of membrane had no $PdCl_2$.

‡Two cells used old cell design and instead of Ag/AgCl used a chlorinated Ag wire as RE.

Instruments G340A battery cycler. Due to the higher ohmic resistance of the H-cell experiments a Peaktech 6225A power supply with a higher voltage limit was used in the H-cell experiments. Experiments were performed in room temperature on a vibration dampening surface. Protective films of either a 6 µm Kapton polyimide film or the original 50 µm thick ethylene vinyl acetate film the CR-39 detectors come shipped with were used in a few experiments in order to limit the CR-39-electrolyte interaction. Any variation from these experimental parameters are described in detail in **Publication II** and its supporting information.

5.2.3 Recombination and radicals

RCC measurement set was aimed at examining CR-39 response to recombination of hydrogen and oxygen gas bubbles on its surface. Figure 19c depicts the 3D-printed PLA holders that used 0.5 mm diameter Pt wire as both WE and CE. These cells were submerged into beakers with 25 mL of electrolytes presented in Table

Table 3. Experiment codes and experimental parameters for recombination cell (RCC) and Fenton's reagent experiments. The CR-39 reaction in RCC experiments was determined by the current direction. Table from **Publication II**.

Exp. No.	Dissolved species	Solvent	Duration A/B/C/D [min]	CR-39 surface reaction	I [mA]
RCC-01	0.3 M LiCl	H_2O	10/30/60/120	HER	-46.4
RCC-02	0.3 M LiCl	H_2O	-/30/60/120	OER	42.9
RCC-03	0.3 M LiCl	D_2O	30/120	HER	-49.6
RCC-04	0.3 M LiCl	D_2O	30/120	OER	39.2
RCC-05	0.3 M LiCl + 0.01 M ascorbic acid	H_2O	30/120	HER	-54.2
RCC-06	0.3 M LiCl + 0.01 M ascorbic acid	H_2O	30/120	OER	53.2
Fenton-01	0.1 M $FeSO_4$	H_2O	5/10	-	-
Fenton-02	0.1 M $FeSO_4$ + 0.01 M ascorbic acid	H_2O	5/10	-	-
Fenton-03	0.1 M $FeSO_4$ + 0.1 M ascorbic acid	H_2O	5/10	-	-

3 along with the maximum current achieved at 5.25 V potential hold. Reaction taking place at the CR-39 was determined by changing the current direction. The table also shows the experiments that utilized Fenton's reagent to probe the CR-39 response to OH-group radicals, which were produced by combining hydrogen peroxide and iron(II) sulfate heptahydrate. Ascorbic acid was added at varying concentrations to function as a free radical scavenger.

5.2.4 Ultrasound cavitation

In the PCD measurement set CR-39 pieces submerged in solutions described in Table 4 were exposed to ultrasound-induced cavitation. CR-39 pieces were attached to the bottom of the containers that were subsequently filled with their respective solution. Larger containers (2 L) were used for the H_2O-based solutions, whereas D_2O-based samples had to be performed in a smaller (180 mL) 3D-printed PLA container. A submerged focusing transducer with a bowl-shaped piezo element in a 3D-printed housing was used generate the ultrasound pulses. Excitation signal was generated by an arbitrary signal generator and amplified with a power amplifier, which is fed to the transducer to generate a focusing acoustic field in the medium. Transducer-to-sample distance, and with that the focal point separation from the CR-39 samples, was calibrated using lower excitation amplitudes and observing the echo signal for distinct echoes produced by cavitation bubbles at the CR-39 surface. Once the transducer alignment was complete, high-amplitude ultrasound bursts were focused in a grid near the CR-39 surface. The transducer-to-sample distance was incrementally increased resulting

Table 4. Solutions used in different polymer cavitation damage (PCD) experiments and their codes. Table from **Publication II**.

Exp. No.	Solution
PCD-01	H_2O
PCD-02	H_2O + 0.3 M LiCl
PCD-03	H_2O + 0.3 M LiCl + 1 M ascorbic acid
PCD-04	D_2O
PCD-05	D_2O + 0.3 M LiCl + 1 M ascorbic acid

in the cavitation cloud being formed farther from the CR-39 piece. Each focal height was sonicated three times before moving to the next height. Stroboscopic Schlieren imaging system was used in H_2O-based solutions to visualize the ultrasound propagation and the resulting cavitation.

5.2.5 COMSOL etching simulation

Time evolution of CR-39 surface profiles during etching was simulated using COMSOL Multiphysics 6.2 software. Figure 20 shows the two-dimensional geometry with the initial seed damage. Quadratic equation $y = ax^2 + c$ was used to press the seed damage to the otherwise flat surface. Depth of the seed damage was controlled by the pre-exponential factor a and and the constant c by setting the boundary condition that the track radius along the surface should be equal, e.g. 100 nm, for all values of a used. Deformed geometry was applied to the surface being etched with prescribed normal mesh velocity, marked with red dashed lines in the Figure 20. Prescribed normal mesh displacement marked with blue dots was applied to the sides of the geometry thus allowing the etching to proceed only along the vertical axis at the edges. Etchant diffusion was modeled with the transport of diluted species physics model. Initial etchant concentration was set to the bulk etchant concentration of 5 M in the entire geometry but only the top of the geometry, marked with solid black line, had this concentration set as a boundary condition. Vertical boundaries were set to have no flux and the inward flux rate of the etched surface was calculated according to Ishigure *et al.* [89] model, which was, however, multiplied by a factor of ten in order to better represent the CR-39 etching behavior observed in the experiments. Different initial seed damage radii along surface and values of a were sampled using parametric sweep to obtain the surface profiles at different etching durations. Surface profiles were then exported and the track radii were compared by finding the points of maximum second derivatives along the surface using a Python script.

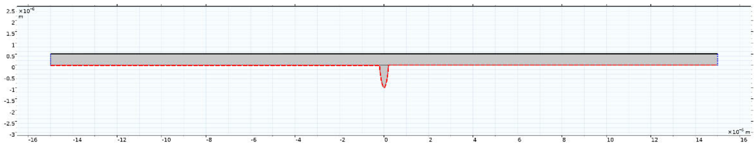

Figure 20. Geometry of the COMSOL simulation with the imprinted seed damage with parabolic shape. Figure from Supporting Information of **Publication II**.

5.3 EPR detection of adsorbed hydrogen

5.3.1 In-situ EC-EPR cell

In **Publication III**, measuring EPR spectra of hydrogen adsorption on Pt *in situ*, required the use of a three-electrode cell constructed inside a 0.8 mm inner diameter glass capillary, as depicted in Figure 21a. Pt wires with 0.2 mm diameter were used for all electrodes, with the reference electrode being insulated from the counter electrode by Teflon tubing. The WE and RE were soldered into their respective contacts, which in turn were covered by 2.0 mm inner diameter silicone tubing. Afterwards the solder contacts were sealed with silicone glue. With the surface area of the working electrode being limited in this cell design, its effective surface area was increased by eroding it. Erosion of the Pt wire was performed by submerging it in 1 M $NaNO_3$ and applying large amplitude sinusoidal voltammetry (LASV) at ± 10 V at 200 Hz for two 60-second periods separated by a 30-second observation period in air. The eroded wire was flushed with deionized water and stored in the electrolyte. Later, the eroded wire was examined with X-ray diffraction (XRD) crystallography and SEM imaging.

Cell assembly itself was performed in Ar atmosphere in order to eliminate the presence of oxygen in the cell, as O_2 has a strong EPR response [68]. Similarly, the electrolyte solution of 0.1 M $HClO_4$ was deaerated with Ar gas for 20 minutes before being transferred into the glove box, where it was injected into the capillary and mounting of WE and RE contacts with a syringe. It was noted that due to the surface tension of the electrolyte total elimination of an Ar bubble from the cell proved infeasible and as a result the cell was assembled in a way that the bubble could be contained at the bottom of the WE side of the cell. Once assembled, the cell was airtight and could be moved from the glove box into the EPR chamber where it was placed in an outer glass tube with a socket for the WE connection, as presented in Figures 21b and 21c.

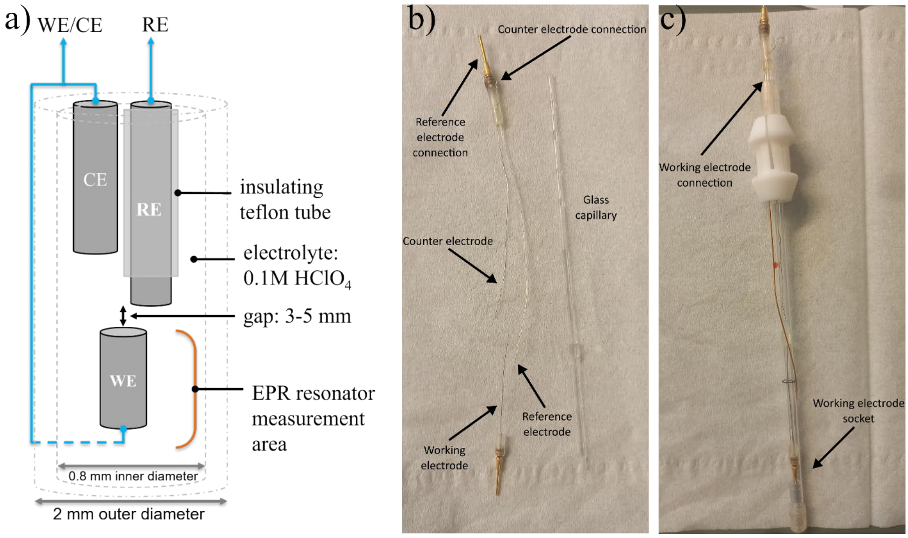

Figure 21. a) Schematic of the *in situ* EC-EPR cell. Cell components before b) and after c) assembly. Figures adapted from **Publication III** and its supporting material.

5.3.2 Electrochemical measurements

For the electrochemical measurements a BioLogic VSP-300 potentiostat was used. The measurement protocol was as follows: after the cell assembly and its insertion into the EPR cavity, the surface of the polycrystalline Pt wire was cleaned electrochemically by cycling the potential between -0.4 V and +0.4 V vs the Pt RE. The cycling was continued until the voltammogram showed a stable response over multiple cycles indicating a clear surface, after which the negative cut-off potential was set to -0.7 V and the cell was cycled again until a stable CV response was obtained. For EPR measurements performed with constant potential holds, the CV potential range was extended before potential holds in steps as presented in Figure 22.

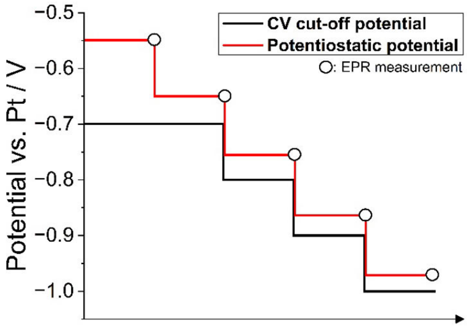

Figure 22. Negative potential CV cut-off potentials and the potentiostatic potentials for the EPR measurements. Figure from **Publication III**.

5.3.3 EPR spectrometry

SpinscanX CW-EPR spectrometer with 10^{14} spins/T sensitivity was used in the EC-EPR measurements with 9.418 GHz microwave frequency. Modulation frequency was set to 100 kHz and its amplitude to 200 µT. The experiments were performed at temperatures ranging from 43 °C to 46 °C within the EPR cavity. For each potentiostatic step, multiple EPR spectra were recorded at 120 s sweep time each. The resulting spectra were averaged, baseline-corrected and filtered with 25 Hz low-pass FFT-filter. For absorption spectra, the recorded EPR spectra were integrated and baseline-corrected.

6 Solvent isotope effects in electrodeposited Ag and Pd

Publication I explores the effects of solvent isotope in electrodeposition of silver and palladium. These noble metals are commonly used as catalysts for various electrochemical reactions such as water electrolysis. However, they are generally expensive and in order to minimize the costs associated with electrolyzers, they need to be manufactured into nanomaterials that have higher active surface areas with respect to their volume, thus reducing the required amount of valuable materials. Electrodeposition is one of the more straightforward methods for manufacturing nanoscale structures. The deposition process at this scale is affected by many factors and extended knowledge of the system's deposition kinetics, nucleation, growth process and diffusion is required to manufacture nanoparticles in desired shape, size and composition on a substrate [90]. Generally it is difficult to vary one of these parameters without influencing the others. One option that has not been widely studied is found in utilizing the different aqueous solvent isotopes. H_2O and D_2O have close to identical chemical properties, but due to the higher mass of D_2O molecules, the electrodeposition process has clear differences in electrolytes based on either heavy or light water. These differences could offer an additional degree of freedom by which the production of nanoparticles with specified properties could be tailored. Potentials in this section are reported vs Ag/AgCl (3 M KCl) reference electrode unless otherwise noted.

6.1 Cyclic voltammetry of Ag and Pd

Potential region for deposition of Ag and Pd from corresponding salts dissolved in H_2O, D_2O or acetonitrile on pencil graphite was evaluated with cyclic voltammetry. Two cycles between +0.6 V and -0.6 V vs Ag/AgCl at 50 mV/s were performed and the resulting voltammograms are presented in Figure 23. On the cathodic scan, the dissolved metal species are deposited onto the graphite surface. For silver deposition the cathodic current peaks were found to reside at -430 mV for both aqueous solvents and at -500 mV in MeCN. During palladium deposition,

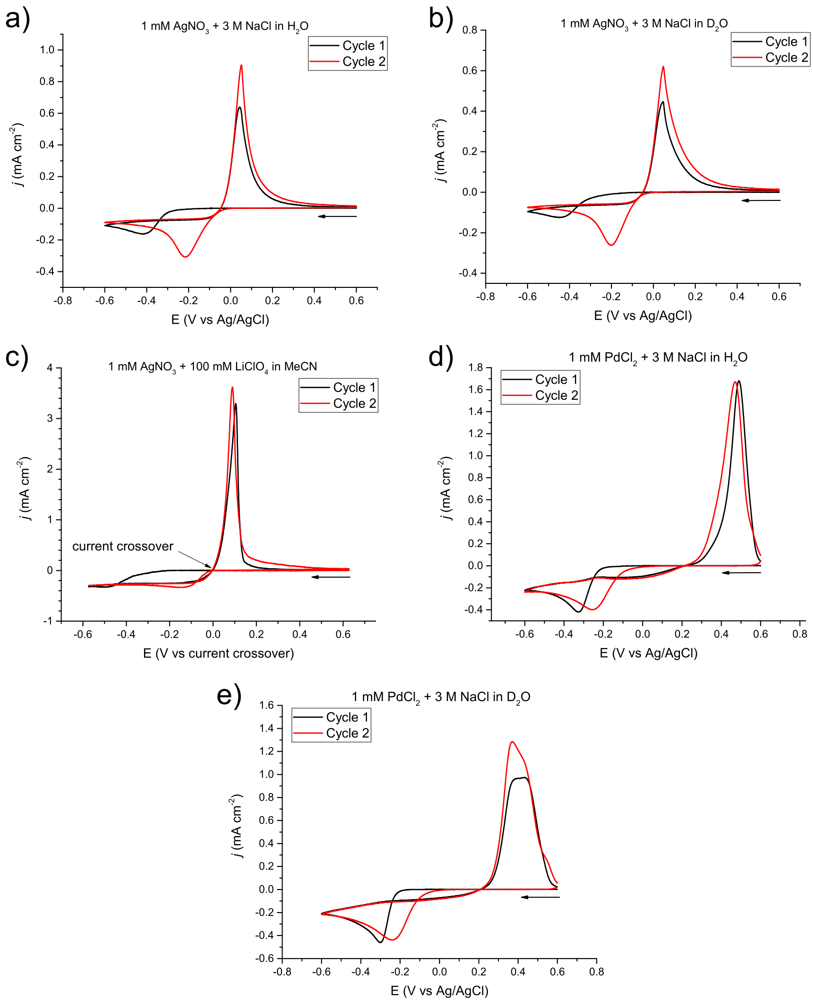

Figure 23. Cyclic voltammograms for Ag (a-c) and Pd (d-e) in their respective solvents recorded at 50 mV/s scan speed. For all voltammograms it is apparent that on the second sweep electrodeposition initiates at lower overpotentials due to remnant deposited metal on the graphite electrode surface that was not stripped during the reverse sweep. Figure adapted from **Publication I**.

the cathodic peaks were -326 mV and -300 mV for H_2O and D_2O respectively.

Deposited metals are dissolved into the solution during the return scan resulting in anodic peaks. For Ag dissolution the peaks were seen at 44, 46 and 105 mV in their respective solvents. Anodic peaks for Pd dissolution were observed at 490 mV for H_2O and 405 mV for D_2O. The anodic peak of Pd in D_2O in Figure 23e had the peak split in two, which was explained by Pd having actually two separate phases, palladium hydride and metallic palladium, undergoing dissolution at slightly different potentials [91]. The first anodic peak corresponds to dissolution of the palladium hydride phase and on later scans it dominates over the pure metallic palladium phase. This indicates that not all of the deposited Pd is stripped during the anodic scan, which results in leftover Pd atoms functioning as nucleation sites with lower activation energies, and thus facilitating the formation of hydride phase palladium. Similarly, on subsequent scans the deposition of the metal species begins at lower overpotential than on the first scan due to the leftover metal deposits. Potentials were scaled to overpotential scale by subtracting the respective equilibrium potentials from the potentials measured vs Ag/AgCl reference electrode with equilibrium potential for Ag in MeCN taken as the current crossover, i.e. the point where anodic sweep potential becomes positive, due to instability of the Ag/AgCl reference electrode in acetonitrile.

6.2 Nucleation of deposited species

With the electrodeposition potential regions selected for each metal–solvent sample from the CVs, the metal species were deposited by applying potential steps with ten second duration. At times $t << 1$ s, the current evolution was dominated by charging of the electrical double-layer, which is seen as rapid decay of initially high current spike, which was presented in Figure 3. This current spike is generally excluded from chronoamperometric curve data when examining the deposition processes, which is dominated by faradaic processes and nucleation phenomena. With onset of the applied potential, the formation of active nucleation sites and resulting growth of the nuclei is observed as a rising current reaching its maximum I_{max} at t_{max}, the point where the diffusion zones of growing individual nuclei have merged with their neighboring ones [92, 93]. Current starts to decay after t_{max} due to the ever increasing overlap between the diffusion zones eventually resulting in planar nucleation. When this decay is linear with respect to $t^{-1/2}$ the system is in diffusion control regime, as presented in Figure 24. At longer time periods, the current decay with Ag in MeCN deviates from linearity indicating departure from diffusion control due to natural convection induced by solvent molecule drift [94]. This was attributed to significantly higher partial molar volume of Ag in MeCN (-20 cm^3 mol^{-1}) with respect Ag in aqueous solution (-6.2 cm^3 mol^{-1}), and easier convection due to its lower viscosity [95–97].

When the nucleation processes are mostly under diffusion control, the Scharifker–Hills model described earlier in Chapter 2 could be used to determine the nucle-

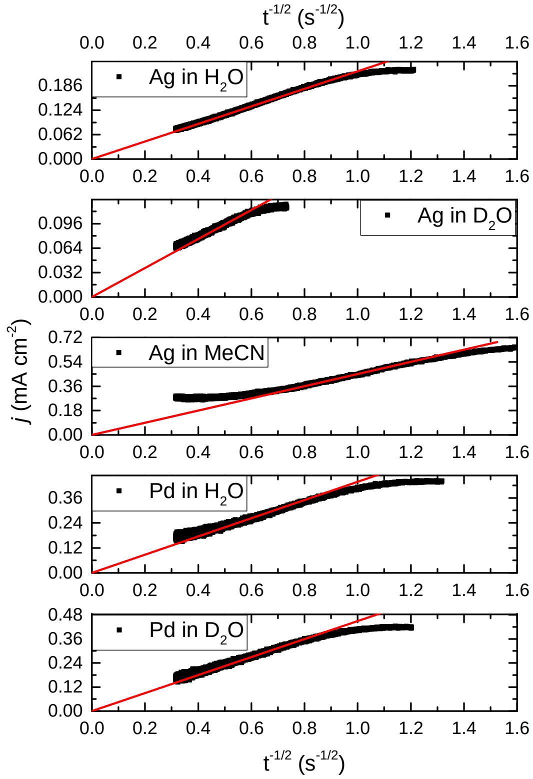

Figure 24. Cathodic peak chronoamperometric curves as a function of $t^{-1/2}$ for the different electrolytes. Linear behavior indicates the diffusion control with the note that for Ag in MeCN deviation at longer time periods is likely caused by earlier onset of natural convection when compared to H_2O and D_2O. Figure from **Publication I**.

ation mechanisms. Scaled current-time curves presented in Figure 25 are compared to theoretical guidelines from Equations 5 and 6 for instantaneous and progressive nucleation mechanisms, respectively. Nucleation mechanism was found to be progressive for electrodeposition of Ag in H_2O, D_2O and MeCN, and similarly for Pd in H_2O and D_2O, which was consistent with literary sources for these potential ranges. Deviations during Pd deposition from the progressive nucleation theoretical curve at longer time periods was understood to have been caused by concurrent catalysis of hydrogen evolution and adsorption creating a saturated H_{ads} layer that blocks some of the metal ions from being deposited on the substrate thus limiting the deposition rate and with that, the current.

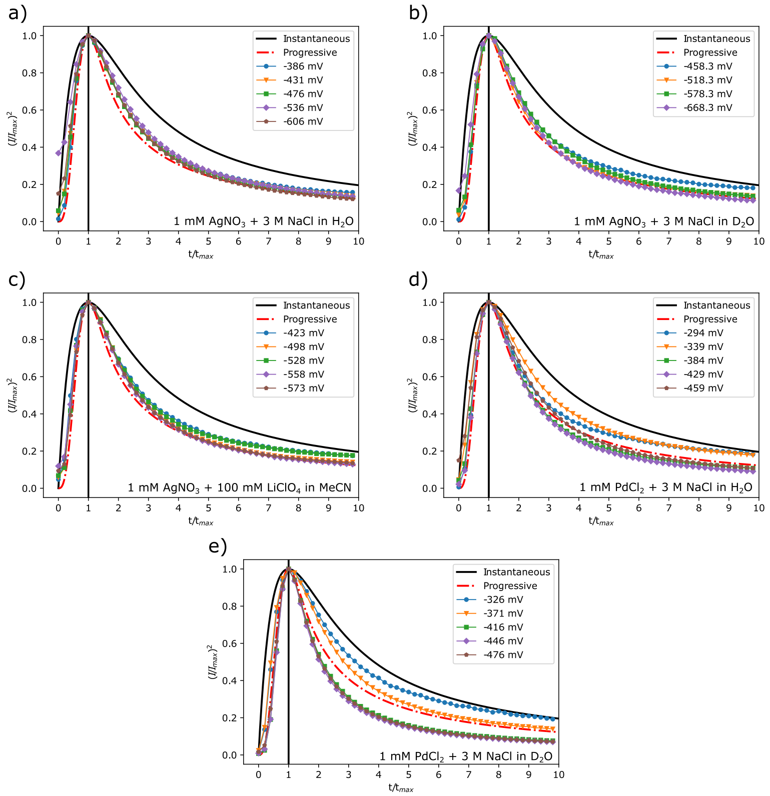

Figure 25. Normalized current transients at indicated overpotentials for Ag electrodeposition in a) H_2O, b) D_2O, and c) MeCN, and for Pd in d) H_2O, e) D_2O. Theoretical chronoamperometric curves for instantaneous (solid black line) and progressive (red dash-dotted line) nucleation mechanisms are plotted as given by the SH-model. For silver electrodeposition the nucleation mechanism is progressive in nature and mostly for Pd as well with clear deviations from the theoretical guide lines at $t > t_{max}$. Figure from **Publication I.**

6.3 Kinetic parameters

In addition to the nucleation mechanisms, also the kinetic parameters of nucleation and growth were extracted from the current transients by curve fitting the Heerman–Tarallo model, giving access to nucleation rate constant per site A that describes the growth rate of an individual nucleus, number density of active sites N_0 and the diffusion coefficient of the dissolved metal ion D. Over the potential range of the measurements, the model gave reasonably good fits, as shown in Figure 26 for Pd deposition in D_2O, and the kinetic parameters were determined from the fitting parameters. Values of the kinetic parameters A and N_0 are shown as a function of overpotential in Figure 27.

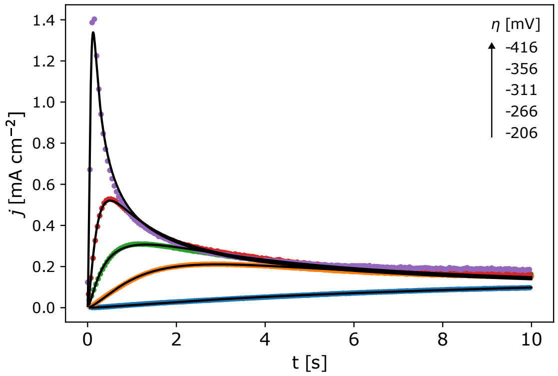

Figure 26. Experimental chronoamperometric curves (dots) of Pd electrodeposition from 1 mM $PdCl_2$ with 3 M KCl in D_2O at varying overpotentials η fitted with the theoretical curves (solid lines). The fitting parameters provide values for the nucleation rate constant per site A, the number density of active sites N_0 and the dissolved species diffusion coefficient D. Figure from **Publication I**.

From the graphs, it is evident that the number density of active sites increases as the cathodic overpotential is increased, demonstrating the site activation energies existing on an energy distribution [98]. Similarly to the nucleation rate constants, logarithmic behavior was also apparent for the nucleation rate constants per site for both Ag and Pd deposition. Comparable behavior had been reported in literature and allowed us to draw a conclusion that the underlying site activation energy distribution is non-linear and affected by the solvent isotope [99–101].

In the case of silver electrodeposition, the values for A in H_2O were similar to ones observed in literature with highly oriented pyrolytic graphite electrode in this experiment's potential range but values have not been reported in literature for Ag electrodeposition in D_2O or MeCN. Behavior of the nucleation rate constant is, however, similar between the solvents for Ag, although a deviation is seen at low overpotentials when depositing Ag from MeCN. This could be due to potential dependency of the deposition mechanism but this was not examined further in the publication due to limited literary sources.

Hydration of Ag^+ in aqueous solutions is known to be more complex than for most other metal species, like Pd. Hydration behavior of silver is affected not only by the inner hydration shell where the Ag^+ ion forms bonds with two water molecules, but also by the mobile water molecules, that form a second hydration shell, which interact weakly with the ion itself or create hydrogen bonds with the first shell water molecules [102]. When dissolved to MeCN, the silver ion is

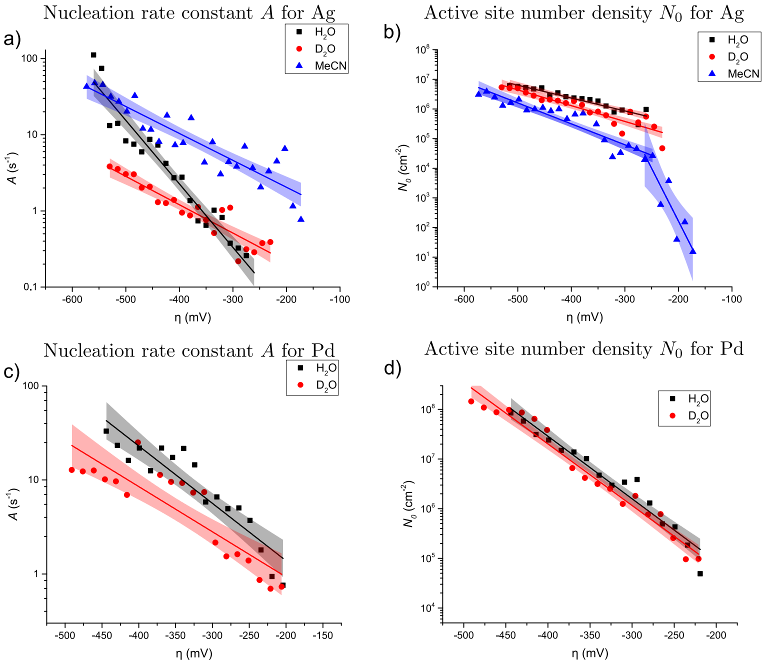

Figure 27. Kinetic parameters nucleation rate constant per site A for (a,c), and number density of nucleation sites N_0 (b,d), for Ag and Pd, respectively, obtained from fitting the Heerman–Tarallo model to the chronoamperometric curves as a function of overpotential. 95% confidence bands are shown for the linear fits on logarithmic scales. Figures adapted from **Publication I**.

bonded with four acetonitrile molecules, and this solvation shell has been found to preferential in mixtures of MeCN and H_2O or methanol [103]. Due to the two-shell structure and strong MeCN binding, the solvation behavior of Ag is much more dependent on the solvent composition than Pd solvation behavior.

In the case of Pd, the slopes do not differ significantly between the aqueous solvent isotopes, however the nucleation rates are consistently higher in H_2O when compared to D_2O, possibly explained by the relatively sluggish movement of D_2O molecules in solvent when compared to H_2O. These experiments demonstrate the slope of nucleation rate constant per site A with respect to η is higher in H_2O for both Ag and Pd electrodeposition than in the other solvents. Dissolved Ag^+ and Pd^{2+} form complexes with chlorine and the surrounding solvation shell in aqueous solutions, whereas in MeCN Ag^+ is complexed with CH_3CN [104, 105]. The thermodynamics of the electrodeposition process dictate that cations must first dissolve their solvation shells and complexes before depositing on a nucleus. Transfer process should be favorable in D_2O and MeCN due to the enthalpies of transfer for Ag^+ and small cations, such as Na^+, being slightly positive (< 3 kJ/mol) when going from H_2O to D_2O while for small anions like chlorine the transfer is slightly negative [106], also when transferring from H_2O to MeCN [107, 108]. Unfortunately, the entropies of transfer were not reported in literature meaning the examination of Gibbs energies of transfer are not known. Thermodynamic effects are, however, unlikely to explain the observed differences in the kinetic parameters as the effect on equilibrium potentials between H_2O and D_2O would not have been negligible. The viscosity of heavy water is 20% higher than light water, so the differences can also originate from merely the slower reorganization of the cation hydration shells and the complexed chlorine ions [109].

Kinetic limitation was deemed not to have been caused by the speed at which the solvent molecules reorganize at the nuclear site because the solvent reorganization energies were evaluated to differ by less than 1%, as derived from Marcus theory [110]. Solvent reorganization energies are split into inner and outer components:

$$\lambda = \lambda_i + \lambda_o, \tag{39}$$

where the inner solvation energies λ_i relate to central elements of the precursor states, which can theoretically be calculated by integrating over the precursor complexes normal vibrational modes, and the outer solvation energies λ_o arising from the solvent. Outer component is evaluated by assuming reactant's sphericity and approximating the solvent as a dielectric continuum resulting in

$$\lambda_o = \frac{e^2}{8\pi\varepsilon_0}\left(\frac{1}{a_O} - \frac{1}{R}\right)\left(\frac{1}{\varepsilon_{op}} - \frac{1}{\varepsilon_s}\right), \tag{40}$$

with a_O being the radius of the solvated species O, R is double the molecule-electrode distance, and ε_{op} and ε_s are the optical and static dielectric constants, respectively. Noting that the a_O and R are identical between the solvent isotopes, the outer reorganization energies differ only due to differences in optical and static dielectric constants with ε_{op} being 1.776889 and 1.763574 and ε_s being 78.39 and 76.06 for H_2O and D_2O, respectively. Inserting these values into Equation 40 evaluates the relative difference of H/D to be 0.9924, which is negligible. However, it should be noted that this consideration of solvent reorganization is not conclusive. In literature it is repeatedly noted that the rate of electrodeposition is significantly influenced by the reorganization of the solvent molecules [111]. In zinc electrodeposition, desolvation has been noted to be the rate-determining step during the transform from Zn-H_2O complex to the desolvated state within the inner Helmholtz plane, which in turn governs if the ion can pass to the interface and transfer charge, or not [112]. Especially for Ag deposition, the strong, yet complex, bonding with solvent ions, and chlorine, it is no wonder that shedding of the solvation shell and subsequent ion rearrangement limit the electrosorption process [113]. For palladium electrodeposition, the rate-determining step is likely not related to the solvation shell, possibly in part due to its higher metal-metal bonding energy(-3.89 eV for Pd vs -2.95 eV for Ag), but rather by the interactions with hydrogen during the deposition process [114]. Pd-hydride formation has been shown to dominate the kinetics of the Pd electrodeposition and this has been linked to mainly the electrode potentials, not the solvent isotopes [115, 116]. As such Pd deposition is more deposition-limited than ion-transport limited. In short timescales, the interfacial properties of the electronic double-layer structure, specific adsorption, solvent orientation and hydrogen bonding affect the initial adsorption and 2D nucleation. On the other hand, 3D nucleation is mostly limited by the diffusion-controlled mass transfer from the bulk electrolyte [104, 117]. Additionally, bulk processes affect the interfacial processes naturally through the solvation behavior of the complexed species. Especially for silver the complexed Cl^- ions are known to compete with the Ag deposition [118].

In respect to the nucleation site densities, the N_0 values are marginally smaller for Ag in D_2O and significantly smaller in MeCN with respect to H_2O, with virtually no difference for Pd in either water isotope. It would be expected that nucleation should occur more readily in D_2O due to its slightly smaller differential capacitance arising from stronger hydrogen bonding network and reduced electrode surface interaction, but this was not observed [119, 120]. Rather, with more chlorine being specifically adsorbed on the electrode surface in D_2O, some of the active sites are blocked, in junction with slower release of active sites from chlorine due to D_2O's higher viscosity are were used to explain the reduced number of active sites when compared to H_2O. Similarly, nucleation should be facilitated in MeCN, as it has lower double-layer capacitance [121] and viscosity [122], but this is not seen due to what is explained by the organic solvent molecules adsorbing preferentially on the surface of the grown nuclei thus inhibiting reactant adsorption [104]. With respect to solvent viscosity the literary resources were limited when it comes to its effects on nucleation and growth rates in electrodeposition context.

These findings indicate that changing the aqueous solvent isotope could be used as an additional parameter to tune when manufacturing nanoparticles. Number density of active deposition sites does not change significantly between H_2O and D_2O solvents but at some potential regions the growth of the nuclei is up to an order of magnitude slower with D_2O as the solvent. This result implies that the effective surface area of the electrode could be increased by depositing the electrocatalytic species at high densities but limiting the growth of the nuclei themselves and preventing planar deposition. To the author's best knowledge, there are no prior studies on altering the electrodeposition process of nanoparticles with isotope substitution. In production of gold nanoparticles by sodium citrate reduction, substituting H_2O for D_2O has reduced the resulting nanoparticle diameters from 9.0 nm to 5.3 nm, and noted that with the D_2O-based synthesis gold nanoparticles with 2-3 nm diameters could be isolated using standard techniques [123]. In a seed-mediated synthesis, gold nanorods with high aspect ratios, on average 8-19, have been produced in D2O-based solvent, whereas using light water average aspect ratio was below 4 [124]. It seems clear that isotope substitution has considerable unexplored potential in both chemical and electrochemical nanoparticle synthesis.

6.4 Surface morphology

Scanning electron microscopy was used to characterize and image the graphite electrode surfaces after the Ag and Pd deposition. The resulting SEM micrographs are presented in Figure 28. It should be noted that here the potentials are given vs Ag/AgCl RE, and the equilibrium potentials presented in the Experimental section should be subtracted from those values to receive overpotentials for accurate comparison. However, due to the relatively small E_{eq} values, these values can be used for qualitative comparisons. Ag deposition exhibited spherical metal deposits with the larger islands being in the order of 130 nm in diameter in H_2O whereas in heavy water the size distribution was more uniform averaging 80 nm with pronounced agglomeration. Larger spherical deposits similar to ones seen in Ag were not observed in Pd deposition where the nuclei were considerably smaller. Diameters of the nuclei were in the order of 20 nm and generally grew together with some exclusion zones due to H/D evolution or bubble formation in between. Smaller size of Pd nuclei is in line with larger active site densities observed in Pd deposition when compared to Ag deposition [117, 125]. Deposited Pd in Figure 28d showed the nuclei growing together to form layers which in turn would continue to grow by one-dimensional growth rather than the 3D growth ob-

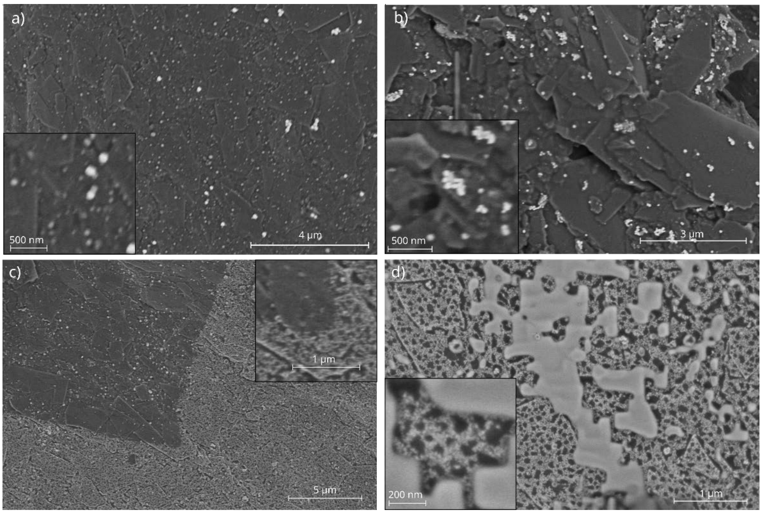

Figure 28. Graphite electrode surfaces after deposition were examined with SEM imaging with 2 kV acceleration voltage, 25 pA current and using a T1 backscattering detector. a) Ag deposited in H_2O at -0.470 V vs Ag/AgCl RE for 10 seconds is seen as bright spots and b) similar, though smaller, are seen also for Ag deposited in D_2O with the same potential and duration. c) Deposited Pd from H_2O at -0.270 V vs Ag/AgCl for 10 seconds has regions without palladium accumulation, likely due to being covered by a since detached clay particle. d) Lastly, with Pd deposited from D_2O at -0.405 V vs Ag/AgCl, certain areas of Pd nuclei had grown together forming layers that would continue plating in uniform layers. Figures from **Publication I**.

served at early moments of deposition process. This observation was suggested to explain the deviation of Pd growth in the normalized current transients from the theoretical ones at $t > t_{max}$ when using higher overpotentials. Pd has been noted to transition from 2D growth to 3D growth relatively quickly, suggesting that the a second layer can start depositing even before the first layer has fully deposited [126]. In the same article it was discussed that the growth rate of the nuclei in Pd deposition on graphite is determined only by the imposed potential, and that diffusion plays a smaller part in the reaction dominated by surface or near surface domains.

7 Polymer damage during metal-hydride co-deposition

Publication II investigated the damage observed on CR-39 surfaces when palladium and hydrogen/deuterium were deposited onto the working electrode simultaneously. Previously there have been literary reports that tracks on CR-39 detectors would be indicative of nuclear events taking place during co-deposition of palladium and deuterium [76–79]. Investigations began by reproducing their results and control experiments. After successfully obtaining tracks during Pd-D co-deposition, additional factors affecting track formation were investigated. In later experiments tracks could be produced without the use of deuterium or even palladium. HER catalyst properties of the deposited metal seemed to be the main factor on whether or not tracks were observed along with the bubble dynamics of the electrolysis cell. Tracks themselves were imaged using a scanning 3D microscope to extract and analyze their dimensional distribution. As a result it would seem that the tracks originate from cavitation-like events taking place near the CR-39 surface providing a seed damage that is subsequently amplified during the etching process.

7.1 Pd-H/D co-deposition

CR-39 damage during metal-hydride co-deposition was examined initially by reproducing earlier experiments by P. Mosier-Boss and L. Forsley [77, 78]. In the first cells, PdE-001 and PdE-002, with H_2O and D_2O as the solvents, respectively, the cathodic current was increased successively as described in the Experimental section. During the first 48 hours the palladium deposited slowly on the working electrode with the potential difference between the two electrodes being at most around 1.0 V. Increasing the current to 5 mA increased the cell voltage to around 2.0 V, causing the rapid and dendritic deposition of the remaining palladium, and the onset of both HER and OER. Generated hydrogen and oxygen bubbles disrupted the sensitive dendritically deposited palladium breaking it apart and leading to the metallic palladium accumulating at the bottom of the cell. During the

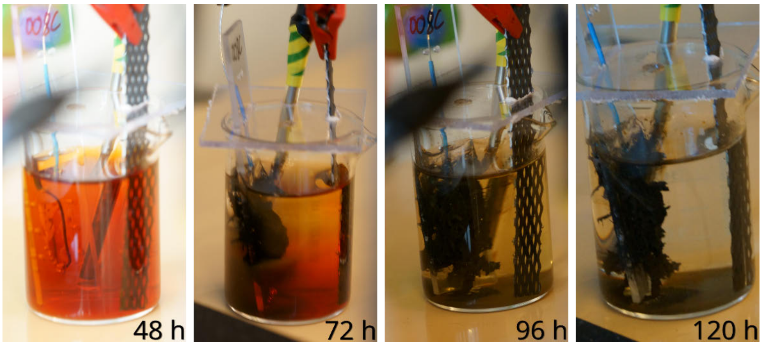

Figure 29. Pd-D co-deposition cell (PdE-008C) at different times over the experimental period. At higher currents, corresponding to higher applied potentials, the dissolved palladium deposits on the Ag working electrode dendritically and grows toward the counter electrode. Bubbles created by the gas evolution reactions disrupted the dendritic growth of the palladium deposit breaking parts of the deposit off, which proceeded to precipitate at bottom of the cell. Figure from **Publication II**.

last 48 hours of the five day experimental period, the current was again increased resulting in higher HER and OER rates, with the last 24 hours at 100 mA current requiring over 5 V potentials, which were not always achieved due to the voltage limit of the potentiostat. Similar cell and its time evolution are depicted in Figure 29.

Any local damage accrued on the CR-39 surface during the experimental period was amplified during the etching process to dimensions observable with visible-light microscopy. Scanning optical microscope images of the entire detector and a selected region of interested are shown in Figures 30a and 30b for the H_2O-based (PdE-001A) experiment, and Figures 30c and 30d for D_2O-based (PdE-002B). Highly circular tracks were in observed in both detectors, with diametral distributions presented in Figure 31 show peaks at around 5 µm, 10 µm and 25 µm ranges. Smaller tracks with sub-10 µm diameters were significantly more numerous when co-deposition was done from D_2O-based electrolyte. These tracks were most concentrated in the vicinity of the silver working electrode, unlike the larger tracks with 25 µm diameter, which were not spatially coordinated with the location of the working electrode. These larger tracks were deemed to have originated from ^{222}Rn background due to the longer wait period between experiment's conclusion and CR-39 etching because the track diameter closely matched tracks produced by an ^{241}Am source used to calibrate the CR-39 detectors. Both radioactive isotopes produce alpha particles with around 5.5 MeV energies during their decay. Tracks produced by an ^{241}Am source are shown in the first panel of

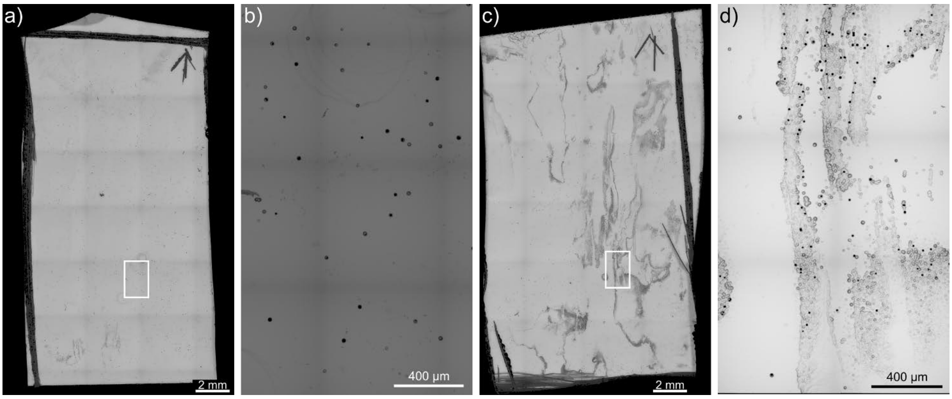

Figure 30. Micrographs of the etched detectors after the Pd-H/D co-deposition experiments. a) In H_2O-based PdE-001A, the number of observed tracks was relatively low and there were very limited amount of large scale track patterns. Most tracks were spread randomly over the entire detector area. White rectangle marks the close-up in b), where relatively uniform highly circular tracks were seen. c) In D_2O-based PdE-002B, the greatest track densities were found along the area where the Ag WE was located during the experiment. d) Tracks in the close-up of the white rectangle in c) exhibited larger variation in their dimensions and spatial distribution with some regions having tracks overlap each other whereas other regions were nearly devoid of any tracks. Figure from **Publication II**.

Figure 32. In subsequent experiments, the CR-39 detectors were etched within 24 hours of a given experiments conclusion, which reduced the quantity of observed background tracks to close to zero.

After demonstrating that the tracks were much more prevalent when heavy water was used as the electrolyte, different system parameters were varied to hone in on the factors that effect if and at what quantity tracks would be observed. The experiments performed included: a) Substituting palladium chloride for copper or platinum chloride. b) Eliminating lithium from the system by substituting lithium chloride with potassium chloride. c) Switching palladium and lithium chlorides for their respective nitrates, thus removing chlorine from the system. d) Changing counter electrodes to platinum-less dimensionally stabilized anode counter electrodes. e) Combining H_2O and D_2O in one-to-one volumetric ratio. The result of these experiments was the initial conclusion that tracks similar to the ones depicted in Figure 30b were only observed when depositing palladium from D_2O-containing electrolyte.

Control experiments suggested by Mosier-Boss *et al.* [77, 78] were performed to exclude non-nuclear CR-39 damaging sources. Protective films were placed between the electrolyte and the CR-39 surface to protect its surface from chemi-

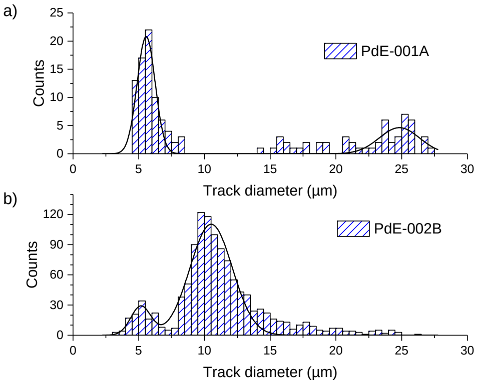

Figure 31. Distribution of the track diameters in a) H_2O-based PdE-001A and b) D_2O-based PdE-002B both presented tracks of different average sizes, one or two peaks in the 5-10 μm range, and larger ones with around 25 μm diameter, which were concluded to have originated from radon background exposure. Figure from **Publication II**.

cal and mechanical damage; either by leaving the 50 μm thick protective film the detectors come shipped with in place, or by adding a separate 6 μm polyimide film. Protective films eliminated the presence of tracks in areas where the films had stayed in contact with the CR-39 surface. In at least one case the original protective film had come loose at the detector edges and palladium had managed to deposit over the unprotected region. The presence of tracks was limited to this region in the etched detector. Applying a forced flow to the electrolyte with a magnetic stirrer had the palladium deposit very close to the working electrode as dendritic growth was suppressed by the fluid movement, with the result that tracks were only observed in the immediate vicinity of the working electrode, unlike in the cells without forced flow where tracks could be found over the detector surface provided that metal had deposited within that region. Temperature of the electrolyte was measured in a three different experiments over the experimental duration. Electrolyte temperatures followed the day-to-day variation ($\sim$ 21 $^{\circ}C \pm 1.5$ $^{\circ}C$) of the laboratory temperature, with other heating of solutions being marginal in comparison.

7.2 Recombination and radicals

Alternative mechanisms for the observed CR-39 damage were also considered. Recombination of oxygen and hydrogen gases, i.e. combustion, produced during HER and OER had been suggested [127] as a possible explanation for the tracks observed in Mosier-Boss experiments. Initially, a similar experiment was

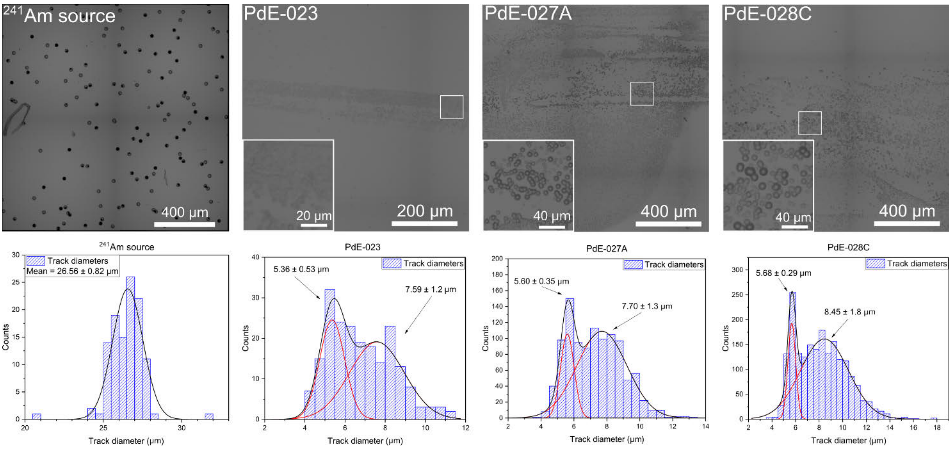

Figure 32. Micrographs of selected areas of analyzed regions of interest from their respective detectors with their track diameter distributions marked with mean track diameters as given by fitted normal distributions. Regions shown in insets with greater magnification are outlined with white squares. Figure from **Publication II**.

performed in an H-cell where the HER and OER take place in their respective cell halves separated by a cation exchange membrane. This did, however, also increase the ohmic losses of the cell and necessitated higher overpotentials than in the base experiments, up to 20 V were required to drive 100 mA of current through the cell. Experiment PdE-023 in Figure 32 shows tracks from one such experiment where tracks were observed only directly below the working electrode, and their size distribution that is in line with the track diameters observed in our earlier experiments.

Direct recombination of oxygen and hydrogen gases generated during the electrolysis was investigated using a different cell design where the different gases would be allowed to come into contact with each other near a slanted CR-39 piece. In these cells the rates of HER and OER were, however, so high that the CR-39 surface was fully saturated with macroscopic bubbles and prevented recombination, if any, from taking place near enough to the detector surface to inflict any damage upon it. Additionally, due to the bubble coverage reducing the attainable electrode surface areas, ohmic heating was considerable as the CR-39 piece was damaged by the heat. Only thermal damage characterized by millimeter scale smooth depressions was observed on the CR-39 surface in these experiments.

Free radicals, such as hydroxyl ($^{\bullet}$OH) and hydroperoxide (HOO$^{\bullet}$) radicals are known to be created during recombination of oxygen and hydrogen gases in electrolysis cells through the formation of hydrogen peroxide [128, 129]. Their potential to damage CR-39 polymer was investigated by exposing CR-39 to radicals generated with Fenton's reagent. No observable damage on the CR-39 surface was observed in these experiments excluding free radicals as a potential explanation for the CR-39 surface damage during electrolysis.

Additional consideration of promoting oxygen and hydrogen gases coming into contact with each other in the original experimental cell was investigated by placing the counter electrode underneath the working electrode, rather than on the other side of the cell. This minor change had a considerable effect on track formation as tracks with similar dimensions and numbers could now be seen when depositing palladium from both H_2O-based electrolyte (PdE-027A) and D_2O-based electrolyte (PdE-028C) in Figure 32. Tracks could be produced even when palladium chloride was replaced with copper chloride provided that a small concentration of platinum chloride was also added to the system. Presumably the additional HER activity provided by the platinum was necessary. These results indicated that the presence of oxygen and/or bubble flow is linked with the observation of tracks on the CR-39 surface.

7.3 Ultrasound cavitation

Cavitation was examined as another alternative non-nuclear explanation for observed CR-39 damage. Cavitation is known to damage multitude of different materials and if tracks produced by cavitation were similar to the ones observed in the co-deposition experiments, this could be used as evidence for there being cavitation-producing mechanisms within the electrolysis cell [43]. This was investigated using ultrasound cavitation where a focusing transducer is used to generate ultrasound pulses that intersect at a focal point and interfere constructively producing pressure gradient large enough to form a cavitation bubble cloud where individual bubbles oscillate between collapsing, rebounding and a further collapse for a limited time. The travel of these ultrasound pulses and the formation of the cavitation bubble cloud were imaged with Schlieren imaging method. The resulting images at 1 µs intervals are shown in Figure 33a.

Cavitation bubbles created in the vicinity of the CR-39 surface produced microjets that visibly damaged the detector surface, even before etching in areas that were used to focus the ultrasound focal point, the same area after etching can be seen in the top left corner of Figure 33b. Subsequently, individual pulses at different focal heights were generated with 100 µm, 200 µm, 400 µm, 600 µm and

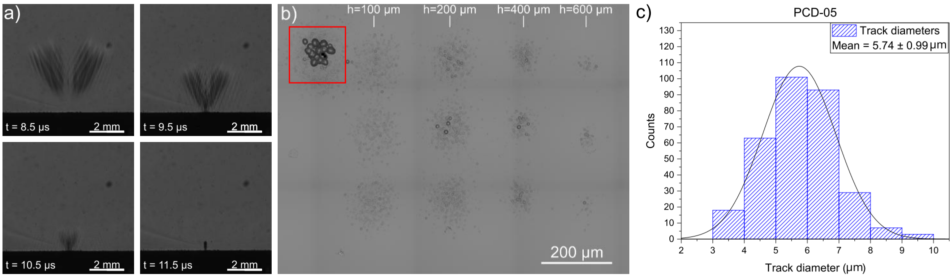

Figure 33. a) Schlieren images showing ultrasound pulse propagation and the formation cavitation bubble cloud at different time delays. b) Tracks seen in etched PCD-05 detector (D_2O-based with 1 M ascorbic acid) produced by cavitation events with varying focal heights. Tracks seen in the top left corner (red square) are the results of continuous cavitation produced at that location during focal point calibration. c) Distribution of track diameters from b) at all heights fitted with a normal distribution. Mean track diameter was found to be 5.74 μm. Figure from **Publication II**.

800 μm vertical separations. Damage produced by these individual pulses was only observed post-etching and the track diameters were noted to be mostly independent from the focal height, only the number of tracks was reduced when the focal point was further from the CR-39 with 800 μm separation showing no tracks at all. It is clear that the generated bubble cloud contained individual bubbles at different vertical separations, and only some of the bubbles were close enough to the detector surface to form a microjet capable of damaging the surface. The tracks produced by ultrasound cavitation were found to be highly circular and average diameters in the range of six micrometers, as shown in Figure 33c, and thus very similar in both aspects to the tracks observed in the earlier co-deposition experiments.

7.4 Cavitation origin

Result of the metal-hydride/deuteride co-deposition experiments was that CR-39 surface is damaged when gas evolution reactions take place in its vicinity, and these damages are observed as tracks after the etching process. Tracks seemed to be more readily observed when heavy water was used as the solvent. In addition, these tracks occur in clusters near the metal deposits. Track diameters tabulated in Table 5 were generally normally distributed, with bifurcation of the distribution observed in many cases. One diameter peak was usually in 5-6 μm and the other approximately 8-10 μm range. Ratio of the distribution peak positions was 0.61 on average. This peak bifurcation was, however, not observed when the CR-39 pieces were exposed to ultrasound-induced cavitation, even if the track diameter

Table 5. Peak positions of the fitted normal distributions along with their standard deviations. Table from **Publication II**.

	Replicate A	Replicate B	Replicate C
Exp. No.	$\overline{d}$ [µm]	$\overline{d}$ [µm]	$\overline{d}$ [µm]
PdE-001	5.46 ± 0.43, 10.7 ± 1.7	8.56 ± 1.5	5.65 ± 0.62
PdE-002	-	5.16 ± 0.65, 10.5 ± 1.4	5.59 ± 0.49, 10.3 ± 1.4
PdE-006	6.87 ± 1.2	5.21 ± 0.88	5.04 ± 0.44, 7.97 ± 1.8
PdE-023	4.94 ± 0.69	-	-
PdE-027	5.60 ± 0.35, 7.70 ± 1.3	5.56 ± 0.60	5.50 ± 0.33, 7.65 ± 1.3
PdE-028	7.35 ± 1.3	7.38 ± 1.5	5.68 ± 0.29, 8.45 ± 1.8
PdE-031	5.39 ± 0.65, 9.16 ± 1.1	-	-
PdE-032	-	4.56 ± 0.48	4.58 ± 0.73
PCD-01	6.49 ± 0.53	-	-
PCD-03	5.09 ± 0.99	-	-
PCD-04	6.55 ± 0.84	-	-
PCD-05	5.74 ± 0.99	-	-
KPF	16.3 ± 0.48	-	-
OPF	4.43 ± 0.33	-	-
^{241}Am	26.56 ± 0.82	-	-
PdE-006/010-control	14.9 ± 1.1	-	-

distributions were very similar. Diametral distribution peak bifurcation and shallow track depths would not be observed if the tracks originated from energetic particles. Because of this, it was concluded that tracks in this diameter range were more likely to originate from cavitation events during HER than from nuclear reactions as suggested in literature. Tracks originating from alpha particles were found to penetrate considerably deeper into the CR-39 bulk whereas tracks formed during co-deposition were limited to only a few micrometers in depth. Penetration depths in selected CR-39 pieces are presented in Figure 34. Tracks from ^{241}Am source were not only larger in diameter at around 26-27 μm range but also penetrated up to 20 micrometers into the CR-39. Background tracks in the first region of interest of PdE-001A also permeated to these depths, unlike the tracks observed near the WE in the second region of interest in PdE-001A. This supported the claim that the background tracks originated from radon exposure. On the other hand, there are no reasonable reaction pathways that could produce the observed peak bifurcation, and as such the nuclear origin on the tracks formed during Pd-D co-deposition was dismissed [130]. Adding to this, transmutations of Pd nuclei into other isotopes of palladium or to other elements have been claimed by some sources [131–133] to take place during Pd-D co-deposition but those claims were not supported by ICP-MS analysis of the electrolyte samples. Elemental and isotopic composition of the electrolyte samples taken before and after

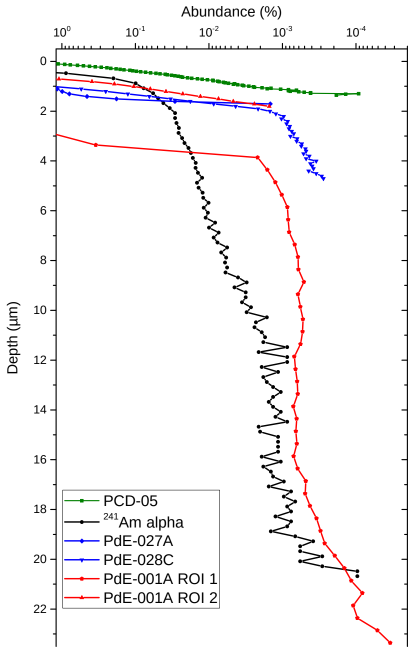

Figure 34. Relative abundance of CR-39 detector surface points at increasing depths. Alpha particle tracks from either a ^{241}Am source and radon tracks in PdE-001A region of interest (ROI) 1 permeate significantly deeper into the polymer than tracks that are spatially coordinated with the Ag WE location during the co-deposition experiments (PdE-001A (ROI 2), PdE-027A and PdE-028C) or the ones produced by ultrasound cavitation (PCD-05). Figure from **Publication II**.

the PdE experiments were measured with ICP-MS. Measured compositions were compared to natural Pd isotope ratio but not statistically significant changes in the isotope content were observed. Traces of transmuted elements such as Ag or Ru were not detected.

Free radicals were also dismissed as a possible cause for the CR-39 surface damage due the CR-39 being surprisingly resistant toward radicals created using Fenton's reagent, not exhibiting any track formation. This left cavitation effects being the likely suspect. Hydrogen and oxygen nanobubbles are generated during HER and OER, respectively [134], on the electrode surface, which then coalesce into larger bubbles that detach into the bulk medium once they have grown to a critical size or disturbed externally [135, 136]. While growing these microscale bubbles reside on top a carpet of hemispherical and spherical nanobubbles [38]. The dimensions of the hemispherical surface nanobubbles generated during HER are affected by the overpotential, with larger overpotentials leading to larger nanobubbles. Typical surface hydrogen bubble radii range from 25 nanometers to up to 100 nanometers [137, 138], meaning that they are generally smaller than spherical nanobubbles observed in bulk liquid at around 200 nm diameters [37]. Cavitation arising from the collapse of spherical nanobubbles and high contact angle (HCA) surface nanobubbles producing two distinct damage profiles on the CR-39 was suggested as an explanation for the observed bifurcation of diametral distributions. Gaseous bubbles collapsing due to the external pressure are prone to produce micro- and nanojets. Due to the nearby surfaces impeding the flow of liquid on the surface side of the bubble collapses slower than the far side resulting in a jet toward the surface [139]. Spontaneous collapse of nanobubbles in ambient pressures usually dominated by viscosity effects, meaning that they do not exhibit jetting behavior as such [140, 141]. However, when nanobubbles are exposed to shock waves, e.g. created by the collapse of nearby bubbles, their cavitation collapse is associated with jetting [46]. On the other hand, merging of hydrogen and oxygen nanobubbles into oxyhydrogen and their combustion had also been suggested in literature [142–144]. The merger of two bubbles is thermodynamically favored over the merger of two bubbles of the same gas thus producing oxyhydrogen bubbles with close to stoichiometric ratio of both gases. Surface-assisted combustion reaction, possibly due to dissociation of H_2 molecules at the surface active sites, ignites the oxyhydrogen bubbles, which proceed to expand into micrometer scale before rapidly collapsing due to the liquid pressure producing jetting behavior either directly or by creating secondary cavitation bubbles [145].

The ignition of oxyhydrogen bubbles themselves is not catalyzed by the metal deposits, and as such the overall HER/OER activity can be considered having more influence on whether such cavitation effects would be observed. This was in line with our observation that track formation was only achieved during Cu deposition when Pt was introduced into the electrolyte to better catalyze HER [143]. Additionally, track formation was more prevalent when the CE was placed underneath the WE in order to facilitate the mixing of oxygen and hydrogen bubbles, further supporting that promoting bubble evolution and interactions is associated with increased track formation. However, track formation in the H-cell experiments where the HER and OER were physically separated by a Nafion membrane, which limited gas crossover considerably, is in opposition of oxyhydrogen bubble combustion as the likely cause along with the lacking explanation of the diametral distribution bifurcation. Oxygen is known to permeate Nafion membranes to a degree so low concentrations of oxygen and thus possibility for oxyhydrogen bubbles in the cathode chamber of the H-cell could not be excluded [146].

Another explored hypothesis contended with shock-induced collapse of nanobubbles, which had been shown in computational studies by Dockar *et al.* [39] to produce pits with similar diameters to the projection of the nanobubbles that created them on amorphous silicon substrate. They separated two different types of collapsing nanobubbles, high contact angle surface nanobubbles and spherical nanobubbles, with the collapse of the latter type producing pits approximately three times as deep as the former type. In comparison to amorphous silicon, CR-39 exposed to similar cavitation events would exhibit considerably greater damage due to its lower tensile strength [147], which is associated with cavitation resistance [43]. Likewise, cavitation during alternating polarity water electrolysis has been shown to mechanically damage Pt, Pd, Au, Ti and W electrodes with the harder materials being more resistant to being damaged [143, 144]. With this in mind, it would be reasonable that the diametral distribution bifurcation is the result of two types of initial seed damages, originating from the collapse of spherical and HCA surface nanobubbles, and that the differences in initial damage dimensions are preserved during the etching process. Collapse of the spherical nanobubbles leads to deeper initial damages that are etched more strongly and thus responsible for the tracks on the CR-39 detectors with 8-10 $\mu\mathrm{m}$ diameters.

Preservation of relative initial damage dimensions over the etching process were confirmed with COMSOL Multiphysics simulations. Figure 35 shows the simulated damage profiles at the beginning of the etching process ($t = 0$ min) and at its end ($t = 180$ min). These simulations for initial damage radii 50, 75, 100 and 200 nm along the CR-39 surface showed that greater track depths result in tracks with larger diameters after etching and that the relative magnitudes of the track depths are more or less preserved. Using the observation from Dockar *et al.* [39] that the HCA bubbles produce tracks with depths approximately one third of the spherical bubble depths, it was noted that in the etching simulation for tracks with the same surface radius, the ratio of radii (post-etching radius with smaller initial depth divided by the on with larger depth) was quite similar (e.g. $\frac{a_{0.33}}{a_1} = 0.68$ for 200 nm radius tracks) to the ratio of the peak positions in the co-deposition experiments.

Differences in the track formation between the light and heavy water were considered but it was noted that the research on heavy water electrolysis was limited and to our knowledge bubble dynamics of D_2 gas during deuterium evolution reaction have not been studied in literature. Thus direct comparisons of the two aqueous isotopes in the case of cavitation could not be examined more thoroughly. D_2 bubbles grow and detach slower than H_2 bubbles during their gas evolution reactions as the reaction rate is greater for HER, and the differences in reaction rate between the isotopes of water are magnified as the overpotential is increased [148]. Higher D_2 nanobubble surface coverages due to the lower reaction rate at high overpotentials was considered as a possible explanation for the greater prevalence of tracks in D_2O-based solutions. Additionally, surface tension of the gas bubbles had been reported in literature to be proportional to the lifetime and larger detachment radii of the evolved bubbles [149]. However, considering that the values for static surface tension of H_2O and D_2O are close to identical and as such unlikely to explain the differences, the dynamic surface tension is likely to differ between the water isotopes. It was considered reasonable that e.g. the higher viscosity of D_2O with respect to H_2O is likely to affect the bubble dynamics of the evolved nanobubbles [150, 151]. It was noted that further research on bubble dynamics in D_2O would be required to investigate cavitation events in heavy water electrolysis. This research provides a possible tool for characterizing cavitation damage over long time spans in gas evolution environments of either aqueous isotope, such as in fuel cells or electrolyzers, provided that the CR-39 response to cavitation is quantitatively calibrated in future research.

Research into ultrasonic cavitation has shown that due to the physical nature of the produced damage, the degradation of polymers exposed to cavitation is largely unaffected the chemical composition of the polymers themselves, but rather depends on the dimensions of the polymer chain [152]. This finding could relatively reasonably be extended to the conclusion that CR-39 cavitation response could be also be used to characterize bubble collapse damage in systems with other polymer-based materials. In proton exchange membrane electrolyzers, the gas bubble dynamics have been identified as a considerable factor to the overall cell durability. Detaching bubbles cause stresses onto the catalyst materials, and the magnitude of the stress has been shown to be directly proportional to the bubble detachment diameter. Without more thorough study, it is difficult to estimate if CR-39 would also be sensitive to this kind of damage, in addition to the possible nanobubble collapse damage, to be used in characterizing PEM electrolyzer degradation, but this avenue could be of interest to those developing more durable catalysts for PEM electrolyzers [153]. Zhao *et al.* [154] have highlighted that the studies on the contribution of evolved gas bubbles in HER and OER have not been paid much attention, even if bubbles have been long considered to be a potential cause for mechanical damage for the surrounding catalyst materials. They directly state as the reason for this the challenges associated with obtaining direct evidence of degradation caused by gas bubbles. It is worth emphasizing that CR-39 does not discriminate between nanoscale and microscale damaging events, and as such, even damage caused by bubble detachment could be recorded using properly prepared CR-39 detectors. For these applications CR-39 has the distinct advantage of not requiring complex optical setups or acoustic measurement devices, and due to its ability to detect and characterize individual cavitation events taking place in the immediate vicinity of the solid surfaces of such electrochemical cells.

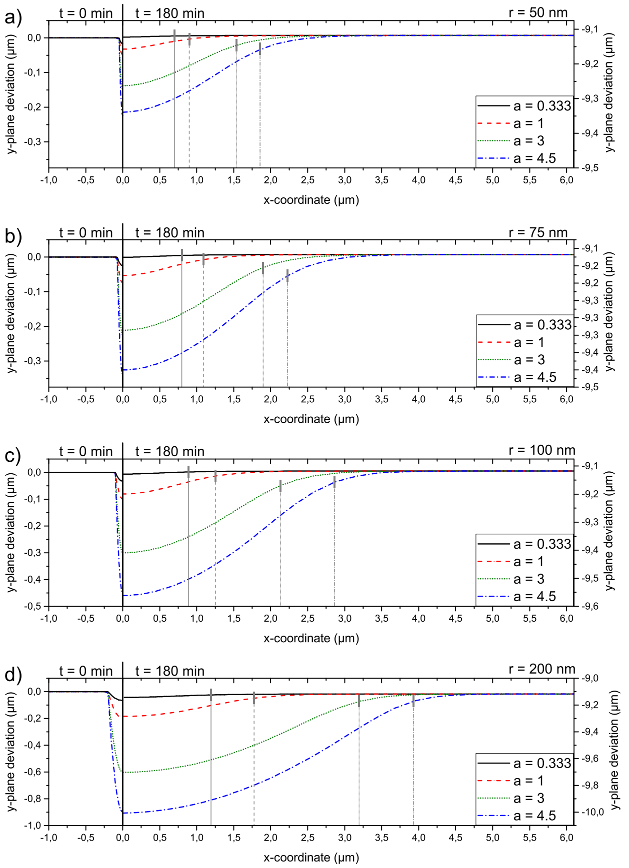

Figure 35. Surface profiles of simulated CR-39 pieces before etching at $t = 0$ min with initial surface track radii of a) 50 nm, b) 75 nm, c) 100 nm, and d) 200 nm, and post-etching at $t = 180$ min. Initial track depth was changed by varying the pre-exponential term of the quadratic equation used to create the initial seed damage. Edges of the etched tracks were selected as the points of maximum curvature change, marked with gray vertical lines. It can be seen that the relative dimensions of the seed damages are preserved when detectors are etched in the same conditions. Figure from **Publication II**.

8 In situ electrochemical EPR and hydrogen adsorption

In **Publication III** the adsorption sites of hydrogen on Pt electrode were examined using EPR spectroscopy. Adsorption of hydrogen on Pt(111) has been notoriously difficult to characterize in realistic conditions due to the complex reaction environment composed of the electrode surface, the near-surface electrolyte layers and the bulk solvent obscuring the adsorption environment from most types of spectroscopy. In electrochemical systems, Kunimatsu *et al.* [56] have observed the vibrational mode characteristic of on-top adsorption of hydrogen for hydrogen deposited at potentials closer to overpotential deposited hydrogen H_{opd} using surface-enhanced infrared absorption spectroscopy (SEIRAS) and theorize the adsorption site of H_{upd} being fcc hollow, but could not definitely attribute any signal to H_{upd} sites. They noted that full occupation of fcc hollow H_{upd} sites could be a prerequisite for H_{opd} adsorption. Nanbu *et al.* [57] were able to reach a similar conclusion some years prior by FT-IRAS measurements of CO_2 being reduced to on-top adsorbed CO using on-top H_{ads} as an intermediate and measuring Pt-CO vibrational modes. In general, hydrogen adsorbed to on-top sites has been relatively well characterized but detection of hydrogen adsorbed to hollow sites, i.e. coordinated with three Pt atoms, has been much more challenging. Bădescu *et al.* [155] were able to observe signals attributed to on-top and fcc/hcp hollow sites on high hydrogen coverage Pt(111) surface using high resolution electron energy loss spectroscopy (HREELS) but rather than an electrochemical system they examined hydrogen adsorption from gas phase.

Due to these challenges in detecting specifically hydrogen adsorbed on fcc hollow sites, as suggested by many computational works, our EC-EPR experiments were considered to try to fill this gap. Hydrogen adsorption sites are directly related to the number of Pt atoms a given hydrogen is coordinated with, and through hyperfine coupling of the adsorbed hydrogen and Pt nuclei, both on-top and fcc/hcp hollow sites could be in theory be detected from the microwave adsorption spectra. Hydrogen adsorption on carbon-supported has been researched with EPR by

Katayama and Kita in 1970's [156], where they were able to show that adsorption of hydrogen was linked to changes in the EPR signal and that the change in the signal was dependent on both electrode potential and pH of the solution. Differences were linked to two cathodic peaks explained as strong and weak hydrogen adsorption with the strong adsorption being near the onset of HER. Additionally, they discussed the reaction pathways being what would now be described as Volmer-Tafel for acidic HER and Volmer-Heyrovský for alkaline HER. They, however, did not examine adsorption site specific responses to the EPR signal, i.e. effects of hyperfine coupling, nor was their carbon-deposited Pt examined with respect to the crystalline facets of the electrode.

In electrochemical systems, hydrogen adsorption is generally investigated with single-crystal surfaces with the redox peak positions being characteristic of their respective crystal facets [157, 158]. However, this approach was not viable for the case of *in situ* EC-EPR measurements as the cell dimensions and the dampening effects of thicker metals restricted the WE choice into a thin polycrystalline platinum (Pt(pc)) wire. Pt(pc) is known to consist of mostly large Pt(111) domains and when the electrode was eroded to increase its effective surface area, the WE could be assumed to be mostly Pt(111) [159, 160]. In the Publication this was supported with XRD measurement and SEM imaging of the Pt(pc) wire. Hydrogen adsorption precedes HER and is initiated at lower overpotentials. By limiting the overpotentials to H_{upd} region, only the adsorption and desorption of hydrogen takes place. Hydrogen can be adsorbed to different adsorption sites, which were presented earlier in Figure 12b, and thus be located next to one, two or three Pt atoms. Adsorbed hydrogen is EPR active in certain conditions [156] and depending on the number of Pt atoms adsorbed hydrogen atoms are coordinated with, a characteristic hyperfine splitting of the hydrogen spectra can be observed, which can be linked back to the adsorption sites. The results from the EPR measurements were supported by a co-author's DFT and ab initio molecular dynamics (MD) simulations of the system.

8.1 Cyclic voltammetry

After cell assembly and the surface cleaning procedures described in Chapter 5, the current response during the CV scan in the EPR chamber presented in Figure 36a was recorded. Qualitative similarity of features in Pt(111) an Pt(pc) CVs shown in Figure 37 is clear, matching literary sources [159, 160]. It should be noted that the sharpness of the CV features is reduced as the electrode surface area becomes smaller, as is the case in the capillary cell. Figure 36b shows a close-up of the cathodic peak with potentials where the EPR response was later measured indicated with circles.

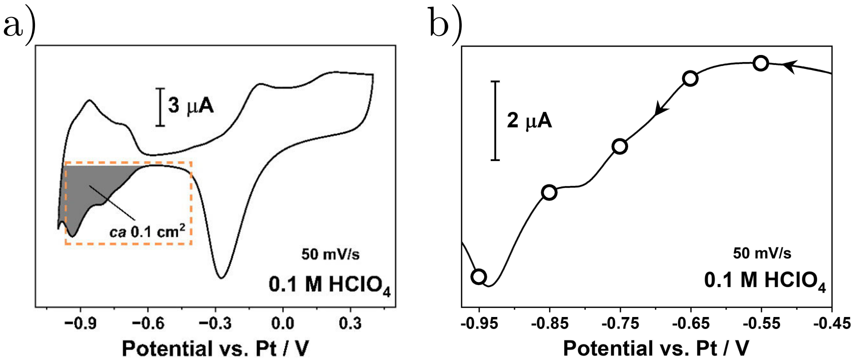

Figure 36. a) Cyclic voltammogram recorded at 50 mV/s of the eroded Pt wire in the EC-EPR cell showed current response characteristic of polycrystalline platinum. b) Close-up of the same voltammogram in the H_{upd} region with the held potentials where the EPR spectra were recorded indicated. Figure from **Publication III**.

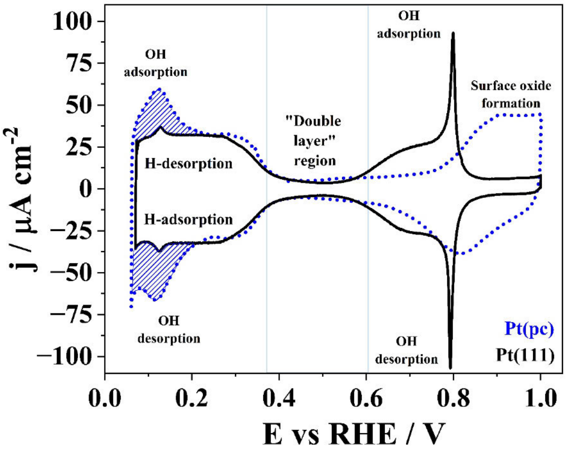

Figure 37. Cyclic voltammograms of polycrystalline Pt (blue dashed line) and Pt(111) (solid black line) in deaerated 0.1 M $HClO_4$ solution measured with scan speed of 50 mV/s illustrates the different potential regions of hydrogen adsorption and desorption. It should be noted that these voltammograms were not performed in the EPR capillary cell. Figure from **Publication III**.

8.2 EPR spectra

Dissolved protons H^+ are not paramagnetic and as such are invisible in the EPR measurements. Once a proton adsorbs onto the Pt(111) surface and reduces, the resulting H_{ads} becomes EPR active and the adsorbed hydrogen is coordinated with one, two or three Pt atoms depending on the adsorption site. Figure 38 shows the simulated EPR responses of an hydrogen atom, or more specifically its electron, coordinated with one (Pt-H), two (Pt_2-H) and three (Pt_3-H) ^{195}Pt atoms and their corresponding hyperfine splitting effects. Nuclear spin of one ^{195} Pt atom is $\frac{1}{2}$ and in Pt-H this causes two absorbance peaks to be observed. Similar to the illustration presented in Figure 15, in Pt_2-H the addition of a second nucleus would result in hyperfine splitting in 1:2:1 intensity ratio, and for Pt_3-H the result would be four peaks with 1:2:2:1 intensity distribution.

The in situ EPR cell itself and the electrolyte have their own EPR responses. Due to this, each part of the cell was also measured separately to gauge their effect in the EPR spectra measured during the actual measurements. The EPR spectra for the assembled cell shown in Figure 39a without an applied potential show two peaks close to free electron g-factor ($g_e \approx 2.0023$) that are attributed to paramagnetic defects in the glass capillaries and to the Pt wires. The dry cell with normal air inside shows additional responses by mostly oxygen. This background

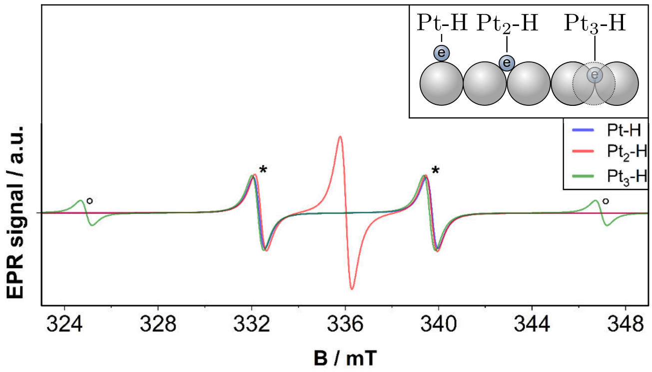

Figure 38. Simulated EPR spectra showing the effects of hyperfine splitting of the electron of adsorbed hydrogen when coordinated with one, two or three ^{195}Pt atoms. The number of coordinated Pt atoms is associated with their respective hydrogen adsorption sites as shown in the inset. Figure adapted from **Publication III**.

closely matches the simulated background spectrum shown in Figure 39b.

In the hydrogen underpotential deposition experiments, the EPR spectra were measured at potential holds ranging from -0.55 V to -0.95 V vs Pt RE but as the first potentials were still well within the double-layer region and showed little to no hydrogen adsorption, only the spectra in the H_{upd} potential region, -0.75 V, -0.85 V and -0.95 V vs Pt RE, are presented in Figure 40. It is clear that the satellite peaks matching to the adsorbed hydrogen being coordinated with one or three Pt atoms are the best defined at -0.85 V potential and that they have mostly disappeared at -0.95 V. This indicates that the maximum H_{ads} coverage is seen at -0.85 V potential and that it is close to the onset of the hydrogen evolution reaction potentials where the EPR-inactive molecular hydrogen is produced. Comparing this experimental result to the simulated spectra in Figure 41 it becomes clear that the satellite peaks are in good agreement for Pt-H, which is also representative of Pt_3-H, and Pt_2-H. A deviation is observed for simulated Pt_2-H close to the central line marked with an arrow. Absence of such deviation from the measured spectra indicates that it is unlikely that hydrogen atoms coordinated with two Pt atoms, i.e. twofold bridge sites, have contributed to the recorded spectra as only Pt-H (on-top sites) and Pt_3-H (hollow sites) are in agreement with both experiment and simulation. In the publication this result was further supported by ab initio molecular dynamics simulations.

While these results, especially when considered alongside the computational part of the work, demonstrate that on-top and fcc hollow sites are the predominant ad-

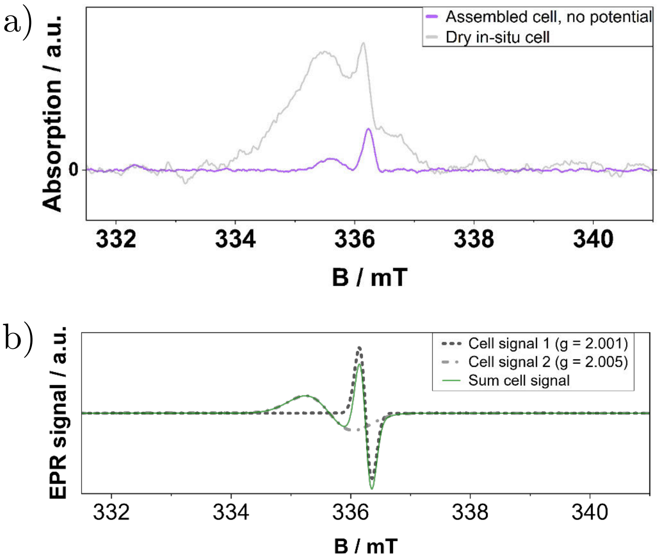

Figure 39. a) Recorded EPR spectra for the degassed and assembled EC-EPR cell in chamber with no applied potential, and the spectrum for the same cell without an electrolyte. b) The spectrum matches closely that of simulated background spectrum with one broad signal at $g = 2.005$ and one narrow one at $g = 2.001$. Figures from **Publication III**.

sorption sites of hydrogen, valid criticism for this kind of EPR measurement was given by the referees during the peer-review process of this publication. Hyperfine coupling between hydrogen and Pt nuclei is only observable when the Pt nuclei in question have non-zero nuclear spin, and of the naturally abundant Pt isotopes, only ^{195}Pt ($\sim 34\%$ abundance) has nuclear spin of $\frac{1}{2}$. This makes hydrogen coupling configurations that can be measured with more ^{195}Pt atoms increasingly unlikely, and leading to reduced bridge and hollow site detectability. Additionally, Pt_1-H and Pt_3-H have close to similar EPR responses in the recorded magnetic field sweep range, and wider sweep range measurements would be needed to detect specifically the satellite peaks originating from Pt_3-H. This type of EC-EPR might be better suited for examining hydrogen adsorption on catalysts with higher abundance of non-zero nuclear spin isotopes, such as Rh, Ir, Au, Ag, Re, In, Cu, Co or Bi [122].

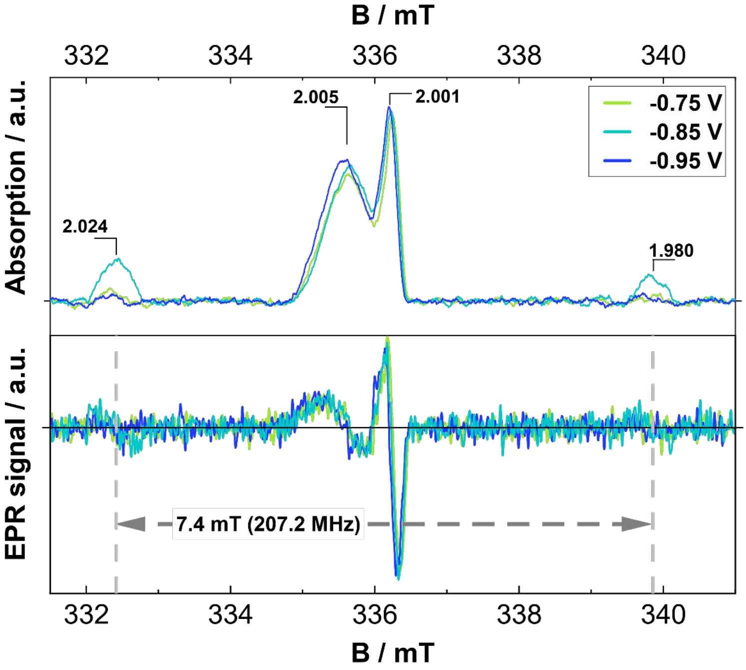

Figure 40. Recorded absorption and raw baseline corrected EPR spectra for potential holds at -0.75 V, -0.85 V and -0.95 V vs Pt with the g-factors marked for absorption peaks. Side peaks caused by hyperfine splitting are more easily identified from the absorption peaks noting that the peaks are the most pronounced when the potential was held at -0.85 V. Figure from **Publication III**.

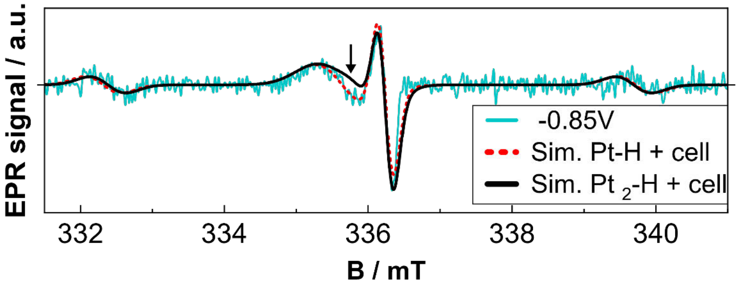

Figure 41. Signal recorded at -0.85 V vs Pt showed the most deviating response of the selected H_{upd} potentials. When compared to simulated spectra Pt-H and Pt_2-H spectra, the deviation between Pt_2-H and the recorded spectrum marked with arrow indicates the absence of two-fold hydrogen adsorption. Figure from **Publication III**.

8.3 DFT-MD energy states of Pt(111) surface

Based on the experimental and simulated EPR results, it seemed that on Pt(111) surface the adsorbed hydrogen would not be found in the twofold bridge sites. Additional atomistic ab initio DFT molecular dynamics simulations were performed by our co-author in high hydrogen coverage conditions. In Figure 42a, the lateral trajectories of adsorbed hydrogen atoms on the Pt surface are shown and it is seen that most of the hydrogen movement takes place in the vicinity of the on-top and fcc hollow sites. Height distribution of the hydrogen atoms with respect to the Pt top layer shown in Figure 42b clearly presents that hydrogen atoms were most likely to be found at heights corresponding to fcc hollow and on-top sites [161].

Simulated two-dimensional Helmholtz free energy profile of the system shown in Figure 43a, exhibited two energy minima for hydrogen adsorption better illustrated in Figure 43b as a free energy line profile. Helmholtz free energy is analogous to Gibbs free energy in constant temperatures. In Figure 43a, the on-top site marked with a red cross in the figure is a local minimum separated from the global minimum of fcc hollow site (pink cross) by a considerable energy barrier. The other threefold site, hcp hollow (yellow cross) is also a local minimum but due to the low energy barrier adsorbed hydrogen atoms quickly move from hcp hollow through the bridge site (cyan cross) into the fcc hollow. These results indicate that as the twofold bridge site is not even a local minimum, the probability of finding hydrogen on that site quickly approaches zero, as supported by the adsorption site occupancy probability convergences in Figure 43c. Thus the hydrogen adsorption on Pt(111) takes place mainly at fcc hollow and on-top sites in this system.

The inner workings of hydrogen adsorption on Pt(111) have been elusive for decades, but these questions are close to being answered, at least computationally. Relatively recently Raffone *et al.* [53] have presented convincing evidence for their explanation on what happens at the Pt surface during hydrogen adsorption and evolution. H_{upd} starts depositing on fcc hollow sites at around 0.4 V vs RHE. The maximum surface coverage for H_{upd} seems to be around 0.66 monolayers on Pt(111), but at potentials slightly above RHE H_{opd} starts depositing to on-top sites, and hydrogen coverages exceed 0.66 monolayers. This behavior coincides what Katayama and Kita [156] termed strongly and weakly adsorbed hydrogen for H_{upd} and H_{opd}, respectively, in their EPR examination of hydrogen adsorption on Pt. Raffone *et al.* clarify that both types of adsorbed hydrogen are always present on the Pt surface and hydrogen continues to adsorb to fcc hollow sites at potentials needed for onset of HER. H_{upd} potential region is linked

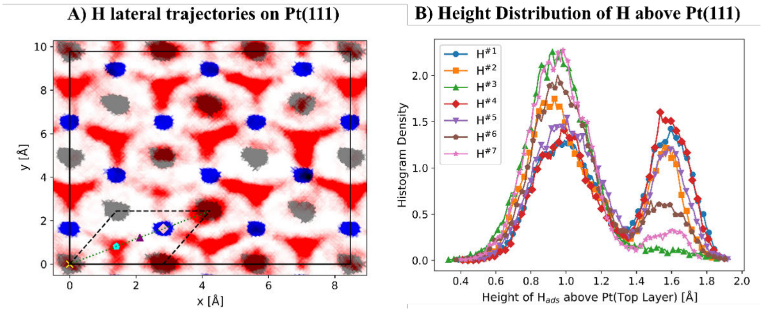

Figure 42. a) Ab initio molecular dynamics simulation of adsorbed hydrogen atoms (red points) trajectories projected onto xy-plane with the top and the second Pt layers marked with gray and blue, respectively. Adsorption sites are marked separately with yellow cross, cyan pentagon, purple triangle and pink diamond for on-top, fcc hollow, bridge and hcp hollow sites, respectively, outlined by the surface unit cell. b) Height distribution with respect to Pt top layer of selected hydrogen atoms ($H^{\#}$) at specified time intervals shows hydrogen atoms being most likely at heights corresponding to fcc hollow and on-top sites. Figure from **Publication III**.

with the solvent water molecules being oriented with oxygen atoms facing the electrode surface, causing the surface to become highly hydrophilic, and inhibits proton transfer. Once H_{opd} starts forming, the surface becomes slightly hydrophobic as the water molecules orient so that their hydrogen atoms point towards the electrode surface, which makes the proton transfer much more efficient. Their findings nicely connect the experimental observations of Katayama and Kita, and those of Kunimatsu *et al.* [56] into a theoretical framework that might finally demystify the hydrogen adsorption processes on Pt(111).

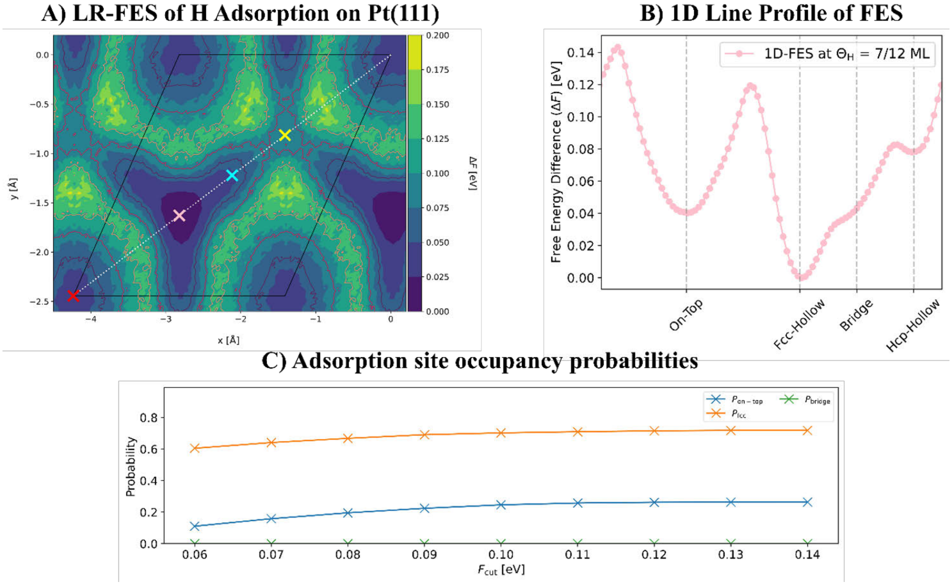

Figure 43. a) Laterally resolved free energy surface of hydrogen adsorption within the Pt(111) unit cell with colored crosses for on-top (red), fcc hollow (pink), bridge (cyan) and hcp hollow (yellow) sites. b) Hydrogen adsorption energy profile along the line connecting the adsorption sites shows fcc hollow and on-top sites as the primary energy minima. c) Occupancy probabilities of the sites converge as the free energy cutoff F_{cut} is increased. Figure from **Publication III**.

9 Conclusions and Outlook

This dissertation focuses on hydrogen production by investigating electrodeposition of catalyst metals in relation to hydrogen evolution reaction from three different angles. Better understanding of HER catalysis enables the production of more efficient catalyst nanostructures that minimize the quantities of valuable materials required. In addition, various polymers are used in electrolyzer cells, and by better understanding of the nature of the damage they accrue in HER environments, cell durability and thus lifetime can be increased. Characterizing hydrogen adsorption sites *in situ* enables better understanding of catalyst behavior in real systems, rather than merely in laboratory setting.

In **Publication I**, nucleation and growth of nanoparticles of Ag and Pd from their salts dissolved into H_2O and D_2O on graphite electrodes during electrodeposition was investigated. First, cyclic voltammetry was used to determine the deposition potential range. Chronoamperometric curves were recorded and analyzed using Scharifker-Hills model to determine the nucleation mechanisms. Fitting the chronoamperometric curves to Heerman-Tarallo model was used to extract kinetic parameters of the deposition process. It was found that the nucleation mechanism was generally progressive in nature leading to heterogeneity in the growth of the nanoparticles. Nucleation mechanism was not affected by the solvent isotope, but the kinetic parameters of deposition process had clear variation between the two aqueous isotopes. The nucleation rate was consistently higher in H_2O-based solvents and for silver electrodeposition this effect was magnified at higher overpotentials. Chemically H_2O and D_2O are close to identical, and as such, it is possible to fine-tune the nanoparticle deposition process for manufacturing e.g. HER catalysts by utilizing different solvent isotopes to either promote or suppress the nucleation rate of active sites, leading to alternative nanoparticle dimensions and distributions. It was noted that using isotope substitution for tuning nanoparticle synthesis has not been explored much in the scientific literature.

Hydrogen evolution reaction is relative simple as far as electrochemical reactions go, but it has been historically challenging to describe accurately due to the complex interplay between water molecules, catalyst surfaces, evolving gas bubbles and charge transfer. Often individual elements of the overall HER are considered in isolation, and their potential interactions can induce considerable challenges to the interpretation of experimental results. In **Publication II**, it was found that when HER active metals are electrodeposited during hydrogen gas evolution, the evolved nanoscale gas bubbles are prone to collapse in cavitation events, which damages CR-39 polymer, and these damages are magnified when CR-39 pieces are etched. CR-39 is commonly used to measure low-flux radiation exposure and thus it was concluded that it is important to consider this alternative damaging mechanism when CR-39 detectors are being utilized in gas evolution environments, and as such prone to this type of cavitation damage. Considerable part of this study was spent in identifying cell parameters, such as electrolyte composition or the cell geometry, that would affect whether or not tracks could be observed on the CR-39 detectors. Initial results suggested that tracks were produced mainly when palladium was electrodeposited concurrently with deuterium gas evolution, but further examinations concluded that the bubble dynamics play a deciding role in the track formation. Furthermore, a convincing explanation for the observed damage was offered by comparisons to CR-39 response to ultrasound-induced cavitation. More precisely, the two types of cavitation events, the collapses of high contact angle surface nanobubbles and spherical nanobubbles, were identified in the diametral distribution of the tracks imaged with 3D-microscopy, and that these tracks were considerably shallower than tracks produced by energetic particles.

HER catalytic properties of a given catalyst material is highly dependent on the nature of the surface adsorption sites. Adsorbed states of hydrogen are, however, challenging to measure *in situ*. In **Publication III**, electron paramagnetic resonance spectroscopy was used to probe the coupling of the adsorbed hydrogen atoms with the nearby platinum atoms in the underpotential deposition region. Using an eroded Pt(111)-like platinum wire working electrode, a miniature three-electrode cell constructed within a capillary. Using this cell setup, electrochemical measurements, cyclic voltammetry and chronoamperometry, were performed while recording the EPR response of the cell. EPR absorption spectra indicated that at 0.85 V vs Pt RE potential, the adsorbed hydrogen atoms are not coupled with two platinum nuclei, i.e., the bridge adsorption site, implying that the on-top site and three-fold sites to be more occupied. Computational ab initio molecular dynamics simulations of Pt(111) surface supported this hypothesis by showing that the probabilities of finding adsorbed hydrogen on bridge sites converge to zero. This insight that hydrogen is preferentially adsorbed on on-top sites and three-fold sites is important for designing nanostructures that maximizes the number of in particular on-top sites that participate the most on H_{opd} and HER. Additionally, this work demonstrated the potential use of EPR in detecting adsorbed hydrogen on catalyst surfaces, possibly enabling more convenient characterization methods for hydrogen adsorption, especially for catalysts with higher abundance of hyperfine coupling capable nuclei.

In the future, the research presented in these works could be expanded by considering larger sets of materials and cell conditions. Additionally, new tools for characterizing material damages in electrolyzers with the use of CR-39, or alternative approaches to examine complex phenomena *in situ* EC-EPR, could be developed based on the findings in these works. It is clear that current literature into many relatively basic electrochemical phenomena is quite limited when it comes to the uses of different aqueous isotopes as the solvent to alter the reaction processes. Further research into D_2O-based electrodeposition and gas evolution reactions might not only give rise to improved manufacturing methods, but also help illuminate the still obscure parts of hydrogen evolution reaction environment. I have hope that, with time and through great effort, hydrogen-based energy infrastructure will have its time in the sun, and eventually, perchance humanity's fate lies beyond this rocky planet – deep within the stars.

List of References

[1] A.J. Bard and L.R. Faulkner. *Electrochemical Methods: Fundamentals and Applications*. Wiley, 2012. ISBN: 9781118312803.

[2] Cynthia Zoski. *Handbook of Electrochemistry*. Elsevier Science, Jan. 2007. ISBN: 9780444519580. DOI: `10.1016/B978-0-444-51958-0.X5000-9`.

[3] Kimmo Pyyhtiä. „Electrodeposition of palladium in H2O and D2O". Master's thesis. Turku, Finland: University of Turku, May 2022. Available at `https://urn.fi/URN:NBN:fi-fe2022060844090`.

[4] Charles Kittel. *Introduction to Solid State Physics*. 8th ed. Wiley, 2004. ISBN: 9780471415268.

[5] Weiwei Cai et al. „2 - Electrode Kinetics of Electron-Transfer Reaction and Reactant Transport in Electrolyte Solution". In: *Rotating Electrode Methods and Oxygen Reduction Electrocatalysts*. Ed. by Wei Xing, Geping Yin, and Jiujun Zhang. Amsterdam: Elsevier, 2014, pp. 33–65. ISBN: 978-0-444-63278-4. DOI: `https://doi.org/10.1016/B978-0-444-63278-4.00002-1`.

[6] E. Budevski, G. Staikov, and W. J. Lorenz. *Electrochemical Phase Formation and Growth: An Introduction to the Initial Stages of Metal Deposition*. Wiley, June 1996. ISBN: 9783527614936. DOI: `10.1002/9783527614936`.

[7] Benjamin Scharifker and Graham Hills. „Theoretical and experimental studies of multiple nucleation". In: *Electrochimica Acta* 28.7 (July 1983), pp. 879–889. DOI: `10.1016/0013-4686(83)85163-9`.

[8] Noémie Elgrishi et al. „A Practical Beginner's Guide to Cyclic Voltammetry". In: *Journal of Chemical Education* 95.2 (2018), pp. 197–206. DOI: `10.1021/acs.jchemed.7b00361`.

[9] C.H. Hamann, A. Hamnett, and W. Vielstich. *Electrochemistry*. Wiley, 2007. ISBN: 9783527310692.

[10] Matthias M. Waegele et al. „How cations affect the electric double layer and the rates and selectivity of electrocatalytic processes". In: *Journal of Chemical Physics* 151.16 (2019), 1DUMMT. DOI: `10.1063/1.5124878`.

[11] S. Amokrane and J. P. Badiali. „Analysis of the Capacitance of the Metal—Solution Interface: Role of the Metal and the Metal—Solvent Coupling". In: *Modern Aspects of Electrochemistry No.22*. Springer US, 1992, 1–95. ISBN: 9781461533764. DOI: `10.1007/978-1-4615-3376-4_1`.

[12] Neil W. Ashcroft and N. David Mermin. *Solid State Physics*. Philadelphia: Saunders College Publishing, 1976.

[13] Sergio Trasatti and Enn Lust. „The Potential of Zero Charge". In: *Modern Aspects of Electrochemistry*. Ed. by Ralph E. White, J. O'M. Bockris, and B. E. Conway. Boston, MA: Springer US, 1999, pp. 1–215. ISBN: 978-0-306-46917-6. DOI: `10.1007/0-306-46917-0_1`.

[14] J. W. McClure. „Band Structure of Graphite and de Haas-van Alphen Effect“. In: *Physical Review* 108.3 (Nov. 1957), 612–618. DOI: `10.1103/physrev.108.612`.

[15] Ezequiel Leiva and Wolfgang Schmickler. „The double-layer capacity of sp metals“. In: *Journal of Electroanalytical Chemistry and Interfacial Electrochemistry* 205.1–2 (June 1986), 323–328. DOI: `10.1016/0022-0728(86)90244-5`.

[16] Christian M. Schott et al. „How to Assess and Predict Electrical Double Layer Properties. Implications for Electrocatalysis“. In: *Chemical Reviews* 124.22 (Nov. 2024), 12391–12462. DOI: `10.1021/acs.chemrev.3c00806`.

[17] A. Einstein. „Eine neue Bestimmung der Moleküldimensionen“. In: *Annalen der Physik* 324.2 (Jan. 1906), 289–306. DOI: `10.1002/andp.19063240204`.

[18] Aashutosh Mistry and Venkat Srinivasan. „On our limited understanding of electrodeposition“. In: *MRS Advances* 4.51-52 (2019), pp. 2843–2861. DOI: `10.1557/adv.2019.443`.

[19] Yuliy D. Gamburg and Giovanni Zangari. *Theory and Practice of Metal Electrodeposition*. Springer New York, 2011. ISBN: 9781441996695. DOI: `10.1007/978-1-4419-9669-5`.

[20] BR Scharifker and J Mostany. „Three-dimensional nucleation with diffusion controlled growth Part I. Number density of active sites and nucleation rates per site“. In: *Journal of electroanalytical chemistry* 177 (1984), pp. 13–23. URL: `http://www.sciencedirect.com/science/article/pii/0022072884802077`.

[21] Luc Heerman and Anthony Tarallo. „Theory of the chronoamperometric transient for electrochemical nucleation with diffusion-controlled growth“. In: *Journal of Electroanalytical Chemistry* 470.1 (July 1999), pp. 70–76. DOI: `10.1016/S0022-0728(99)00221-1`.

[22] P. C. T. D'Ajello, M. L. Munford, and A. A. Pasa. „Transient equations for multiple nucleation on solid electrodes: A stochastic description“. In: *The Journal of Chemical Physics* 111.9 (Sept. 1999), pp. 4267–4272. DOI: `10.1063/1.479724`.

[23] Gong Luo et al. „Potentiostatic Current Transient for Multiple Nucleation: A Limited-Diffusion Process Description“. In: *Journal of The Electrochemical Society* 165.3 (2018), pp. D147–D151. DOI: `10.1149/2.0711803jes`.

[24] Gong Luo et al. „Current Transition of Nucleation and Growth under Diffusion-Controlled Electrocrystallization: A Brief Review“. In: *Coatings* 12.8 (2022), pp. 1–14. DOI: `10.3390/coatings12081195`.

[25] Arthur Shih et al. „Water electrolysis“. In: *Nature Reviews Methods Primers* 2 (Oct. 2022), p. 84. DOI: `10.1038/s43586-022-00164-0`.

[26] Agata Godula-Jopek, Detlef Stolten, and Cyril Bourasseau. *Hydrogen production : by electrolysis*. 1st ed. Weinheim, Germany: WILEY-VCH Verlag GmbH & Co. KGaA, 2015. ISBN: 9783527676538.

[27] Gyubin Min, Saeyoung Choi, and Jongsup Hong. „A review of solid oxide steam-electrolysis cell systems: Thermodynamics and thermal integration“. In: *Applied Energy* 328 (2022), p. 120145. DOI: `https://doi.org/10.1016/j.apenergy.2022.120145`.

[28] Matheus T. de Groot, Joost Kraakman, and Rodrigo Lira Garcia Barros. „Optimal operating parameters for advanced alkaline water electrolysis“. In: *International Journal of Hydrogen Energy* 47.82 (2022), pp. 34773–34783. DOI: `https://doi.org/10.1016/j.ijhydene.2022.08.075`.

[29] Jenni J. Jarju, Marta C. Figueiredo, and Yury V. Kolen'ko. „Chapter 8 - Electrocatalysis using nanomaterials“. In: *Nanoscale Electrochemistry*. Ed. by Andrew J. Wain and Edmund J.F. Dickinson. Vol. 18. Frontiers of Nanoscience. Elsevier, 2021, pp. 343–420. DOI: `https://doi.org/10.1016/B978-0-12-820055-1.00002-2`.

[30] Volkan Cicek. „The Thermodynamics of Corrosion“. In: *Corrosion Engineering*. John Wiley & Sons, Ltd, 2014. Chap. 6, pp. 83–100. ISBN: 9781118720837. DOI: `https://doi.org/10.1002/9781118720837.ch6`.

[31] Marc T.M. Koper. „Analysis of electrocatalytic reaction schemes: Distinction between rate-determining and potential-determining steps“. In: *Journal of Solid State Electrochemistry* 17.2 (2013), pp. 339–344. DOI: `10.1007/s10008-012-1918-x`.

[32] Noémie Elgrishi et al. „Reaction Pathways of Hydrogen-Evolving Electrocatalysts: Electrochemical and Spectroscopic Studies of Proton-Coupled Electron Transfer Processes“. In: *ACS Catalysis* 6.6 (2016), pp. 3644–3659. DOI: `10.1021/acscatal.6b00778`.

[33] Martí López et al. „Theoretical study of the mechanism of the hydrogen evolution reaction on the V2C MXene: Thermodynamic and kinetic aspects“. In: *Journal of Catalysis* 421 (May 2023), 252–263. DOI: `10.1016/j.jcat.2023.03.027`.

[34] Michael T. Tang et al. „Modeling Hydrogen Evolution Reaction Kinetics through Explicit Water–Metal Interfaces“. In: *The Journal of Physical Chemistry C* 124.51 (2020), pp. 28083–28092. DOI: `10.1021/acs.jpcc.0c08310`.

[35] Saad Intikhab, Joshua D Snyder, and Maureen H Tang. „Adsorbed Hydroxide Does Not Participate in the Volmer Step of Alkaline Hydrogen Electrocatalysis“. In: *ACS Catalysis* 7.12 (2017), pp. 8314–8319. DOI: `10.1021/acscatal.7b02787`.

[36] Samuel Akinlolu Ogunkunle et al. „Navigating Alkaline Hydrogen Evolution Reaction Descriptors for Electrocatalyst Design“. In: *Catalysts* 14.9 (2024). DOI: `10.3390/catal14090608`.

[37] Qing-Nan Wang et al. „Bubble Dynamics during Hydrogen Evolution Reaction over Fluidizable Electrocatalyst Particles“. In: *Industrial & Engineering Chemistry Research* 64.9 (2025), pp. 5087–5098. DOI: `10.1021/acs.iecr.4c04934`.

[38] Sunghak Park et al. „Combined effects of electrode morphology and electrolyte composition on single H2 gas bubble detachment during hydrogen evolution reaction“. In: *Nanoscale* 17 (16 2025), pp. 10020–10034. DOI: `10.1039/D5NR00234F`.

[39] Duncan Dockar, Livio Gibelli, and Matthew K. Borg. „Shock-induced collapse of surface nanobubbles“. In: *Soft Matter* 17 (28 2021), pp. 6884–6898. DOI: `10.1039/D1SM00498K`.

[40] Adarsh Shekhar et al. „Nanobubble Collapse on a Silica Surface in Water: Billion-Atom Reactive Molecular Dynamics Simulations“. In: *Phys. Rev. Lett.* 111 (18 Oct. 2013), p. 184503. DOI: `10.1103/PhysRevLett.111.184503`.

[41] Jean-Pierre Franc and Jean-Marie Michel. *Fundamentals of Cavitation*. Springer Netherlands, 2005. ISBN: 9781402022333. DOI: `10.1007/1-4020-2233-6`.

[42] Hermann Schlichting and Klaus Gersten. *Boundary-Layer Theory*. Springer Berlin Heidelberg, 2017. ISBN: 9783662529195. DOI: `10.1007/978-3-662-52919-5`.

[43] Alicja Krystyna Krella. „Degradation and Protection of Materials from Cavitation Erosion: A Review“. In: *Materials* 16.5 (2023). DOI: `10.3390/ma16052058`.

[44] A. Karimi and J. L. Martin. „Cavitation erosion of materials“. In: *International Metals Reviews* 31.1 (1986), pp. 1–26. DOI: `10.1179/imtr.1986.31.1.1`.

[45] Christopher Brennen. „Cavitation and Bubble Dynamics“. In: *Cavitation and Bubble Dynamics* 44 (Jan. 1995). DOI: `10.1017/CBO9781107338760`.

[46] Ding Ma et al. „Characterization of the Dynamic Behavior of Multinanobubble System under Shock Wave Influence“. In: *Langmuir* 40.17 (2024). PMID: 38628152, pp. 9068–9081. DOI: `10.1021/acs.langmuir.4c00449`.

[47] Jaya Verma and Saurav Goel. „Cost-effective electrocatalysts for Hydrogen Evolution Reactions (HER): Challenges and Prospects“. In: *International Journal of Hydrogen Energy* 47.92 (2022), pp. 38964–38982. DOI: `https://doi.org/10.1016/j.ijhydene.2022.09.075`.

[48] Sergio Trasatti. „Work function, electronegativity, and electrochemical behaviour of metals. III. Electrolytic hydrogen evolution in acid solutions“. In: *Journal of Electroanalytical Chemistry* 39.1 (1972), pp. 163–184. DOI: `10.1016/S0022-0728(72)80485-6`.

[49] J. K. Nørskov et al. „Trends in the Exchange Current for Hydrogen Evolution“. In: *Journal of The Electrochemical Society* 152.3 (Jan. 2005), J23. DOI: `10.1149/1.1856988`.

[50] Egill Skúlason et al. „Modeling the Electrochemical Hydrogen Oxidation and Evolution Reactions on the Basis of Density Functional Theory Calculations“. In: *The Journal of Physical Chemistry C* 114.42 (2010), pp. 18182–18197. DOI: `10.1021/jp1048887`.

[51] Timothy T. Yang et al. „Revisiting trends in the exchange current for hydrogen evolution“. In: *Catal. Sci. Technol.* 11 (20 2021), pp. 6832–6838. DOI: `10.1039/D1CY01170G`.

[52] Paola Quaino et al. „Volcano plots in hydrogen electrocatalysis – uses and abuses“. In: *Beilstein Journal of Nanotechnology* 5 (June 2014), 846–854. DOI: `10.3762/bjnano.5.96`.

[53] Federico Raffone et al. „Revealing the molecular interplay of coverage, wettability, and capacitive response at the Pt(111)-water solution interface under bias“. In: *Communications Chemistry* 8.1 (Feb. 2025). DOI: `10.1038/s42004-025-01446-w`.

[54] Egill Skúlason et al. „Density functional theory calculations for the hydrogen evolution reaction in an electrochemical double layer on the Pt(111) electrode“. In: *Phys. Chem. Chem. Phys.* 9 (25 2007), pp. 3241–3250. DOI: `10.1039/B700099E`.

[55] Keiji Kunimatsu et al. „A combined surface-enhanced infrared and electrochemical kinetics study of hydrogen adsorption and evolution on a Pt electrode“. In: *Chemical Physics Letters* 401.4 (2005), pp. 451–454. DOI: `https://doi.org/10.1016/j.cplett.2004.11.100`.

[56] Keiji Kunimatsu et al. „Hydrogen adsorption and hydrogen evolution reaction on a polycrystalline Pt electrode studied by surface-enhanced infrared absorption spectroscopy“. In: *Electrochimica Acta* 52.18 (2007). Surface Imaging/Spectroscopy at Solid/Liquid Interface (ISSIS), pp. 5715–5724. DOI: `https://doi.org/10.1016/j.electacta.2006.12.007`.

[57] Noritoshi Nanbu et al. „Adsorption of atomic hydrogen on a polycrystalline Pt electrode surface studied by FT-IRAS: the influence of adsorbed carbon monoxide on the spectral feature“. In: *Journal of Electroanalytical Chemistry* 485.2 (2000), pp. 128–134. DOI: `https://doi.org/10.1016/S0022-0728(00)00104-2`.

[58] Xiaoxia Chang et al. „Understanding the complementarities of surface-enhanced infrared and Raman spectroscopies in CO adsorption and electrochemical reduction“. In: *Nature Communications* 13.1 (May 2022). DOI: `10.1038/s41467-022-30262-2`.

[59] Patrick Bertrand. *Electron Paramagnetic Resonance Spectroscopy: Fundamentals*. Springer International Publishing, 2020. ISBN: 9783030396633. DOI: `10.1007/978-3-030-39663-3`.

[60] Daniella Goldfarb and Stefan Stoll. *EPR spectroscopy : fundamentals and methods*. eng. 1st ed. eMagRes Books. Chichester, West Sussex, England: Wiley, 2018. ISBN: 9781119162971.

[61] Moritz Kälin, Igor Gromov, and Arthur Schweiger. „The continuous wave electron paramagnetic resonance experiment revisited“. In: *Journal of Magnetic Resonance* 160.2 (Feb. 2003), 166–182. DOI: `10.1016/s1090-7807(02)00186-6`.

[62] Peter B. Ayscough. *Electron Spin Resonance in Chemistry*. Open Library edition OL5642493M. London and New York: Methuen and Barnes & Noble, 1967, p. 451.

[63] P B Ayscough. *Electron Spin Resonance*. The Royal Society of Chemistry, Jan. 1983. ISBN: 978-0-85186-821-9. DOI: `10.1039/9781847553416`.

[64] Hugh D. Young and Roger A. Freedman. *University Physics with Modern Physics*. English. 15th. Boston, MA: Pearson Education, 2019, p. 1608. ISBN: 9780135159552.

[65] John A. Weil and James R. Bolton. *Electron Paramagnetic Resonance: Elementary Theory and Practical Applications*. Wiley, May 2006. ISBN: 9780470084984. DOI: `10.1002/0470084987`.

[66] Clare L. Hawkins and Michael J. Davies. „Detection and characterisation of radicals in biological materials using EPR methodology". In: *Biochimica et Biophysica Acta (BBA) - General Subjects* 1840.2 (2014). Current methods to study reactive oxygen species - pros and cons, pp. 708–721. DOI: `https://doi.org/10.1016/j.bbagen.2013.03.034`.

[67] Yinfeng Zhang, Menghong Dai, and Zonghui Yuan. „Methods for the detection of reactive oxygen species". In: *Anal. Methods* 10 (38 2018), pp. 4625–4638. DOI: `10.1039/C8AY01339J`.

[68] Thomas J. Cook et al. „Gas phase EPR of vibrationally excited O2". In: *The Journal of Chemical Physics* 58.4 (Feb. 1973), pp. 1548–1552. DOI: `10.1063/1.1679393`.

[69] J.J. Wittmann et al. „High-precision measurement of the electron spin g factor of trapped atomic nitrogen in the endohedral fullerene N@C60". In: *Journal of Magnetic Resonance* 290 (May 2018), 12–17. DOI: `10.1016/j.jmr.2018.02.019`.

[70] Willis E. Lamb. „Fine Structure of the Hydrogen Atom. III". In: *Phys. Rev.* 85 (2 Jan. 1952), pp. 259–276. DOI: `10.1103/PhysRev.85.259`.

[71] Stephan den Hartog et al. „Electrocatalysis under a magnetic lens: A combined electrochemistry and electron paramagnetic resonance review". In: *Electrochimica Acta* 407 (2022), p. 139704. ISSN: 0013-4686. DOI: `https://doi.org/10.1016/j.electacta.2021.139704`.

[72] Mika A. Tamski et al. „Electrochemical electron paramagnetic resonance utilizing loop gap resonators and micro-electrochemical cells". In: *Physical Chemistry Chemical Physics* 17.36 (2015), 23438–23447. DOI: `10.1039/c5cp04259c`.

[73] Genping Yi et al. „Identification and quantification of electron-generated atomic hydrogen through in-situ electron spin resonance and density functional theory". In: *Chemical Engineering Journal* 483 (2024), p. 149226. DOI: `https://doi.org/10.1016/j.cej.2024.149226`.

[74] Maryam Seif-Eddine et al. „Operando film-electrochemical EPR spectroscopy tracks radical intermediates in surface-immobilized catalysts". In: *Nature Chemistry* 16.6 (Feb. 2024), 1015–1023. DOI: `10.1038/s41557-024-01450-y`.

[75] Anwar Ul-Hamid. *A Beginners' Guide to Scanning Electron Microscopy*. Springer International Publishing, 2018. ISBN: 9783319984827. DOI: `10.1007/978-3-319-98482-7`.

[76] Stanislaw Szpak, Pamela Boss, and Frank Gordon. „Further evidence of nuclear reactions in the Pd/D lattice: Emission of charged particles". In: *Die Naturwissenschaften* 94 (July 2007), pp. 511–4. DOI: `10.1007/s00114-007-0221-7`.

[77] P.A. Mosier-Boss et al. „Detection of high energy particles using CR-39 detectors part 1: Results of microscopic examination, scanning, and LET analysis". In: *International Journal of Hydrogen Energy* 42.1 (2017), pp. 416–428. DOI: `https://doi.org/10.1016/j.ijhydene.2016.09.223`.

[78] Pamela Boss and Lawrence Forsley. „Energetic Particle Emission in Pd/D Co-deposition: An Undergraduate Research Project to Replicate a New Scientific Phenomenon". In: *Journal of Laboratory Chemical Education* 6 (June 2018). DOI: `10.5923/j.jlce.20180604.01`.

[79] P.A. Mosier-Boss and L.P. Forsley. „Chapter 2 - Review of Pd/D co-deposition". In: *Cold Fusion*. Ed. by Jean-Paul Biberian. Elsevier, 2020, pp. 17–36. ISBN: 978-0-12-815944-6. DOI: `https://doi.org/10.1016/B978-0-12-815944-6.00002-6`.

[80] T. Portwood and J. Stejny. „Analysis of CR-39 and the effect of additives.“ In: *Nuclear Tracks and Radiation Measurements (1982)* 8.1 (1984). Special Volume: Solid State Nuclear Track Detectors, pp. 151–154. DOI: `https://doi.org/10.1016/0735-245X(84)90076-0`.

[81] A. F. Saad, N. M. Al-Faitory, and R. A. Mohamed. „Study of the optical properties of etched alpha tracks in annealed and non-annealed CR-39 polymeric detectors“. In: *Radiation Physics and Chemistry* 97 (2014), pp. 188–197. DOI: `10.1016/j.radphyschem.2013.11.021`.

[82] M.I. Al-Jarallah et al. „Investigation of proton response of CR-39“. In: *Nuclear Instruments and Methods in Physics Research Section B: Beam Interactions with Materials and Atoms* 73.4 (1993), pp. 507–511. DOI: `https://doi.org/10.1016/0168-583X(93)95833-Q`.

[83] Matiullah et al. „A review of the use of CR-39 track detector in personnel neutron dosimetry and spectrometry“. In: *Nuclear Instruments and Methods in Physics Research Section B: Beam Interactions with Materials and Atoms* 51.1 (1990), pp. 76–84. DOI: `https://doi.org/10.1016/0168-583X(90)90542-3`.

[84] G.S. Sahoo et al. „Effects of neutron irradiation on optical and chemical properties of CR-39: Potential application in neutron dosimetry“. In: *Applied Radiation and Isotopes* 94 (2014), pp. 200–205. DOI: `https://doi.org/10.1016/j.apradiso.2014.08.012`.

[85] Hirokazu Miyoshi et al. „Optical property of CR-39 synthesized by doping with methylviologen-encapsulated SiO2 nanocapsules as a solid-state X-ray plate detector“. In: *Optical Materials* 55 (2016), pp. 109–114. DOI: `10.1016/j.optmat.2016.02.042`.

[86] Erik P Ziehm and George H Miley. „On the detection of alpha emission from a low-voltage DC deuterium discharge with palladium electrodes“. In: *arXiv preprint arXiv:2402.05117* (2024), pp. 1–18. arXiv: `arXiv:2402.05117v1`.

[87] Johannes Schindelin et al. „Fiji: An open-source platform for biological-image analysis“. In: *Nature Methods* 9.7 (2012), pp. 676–682. DOI: `10.1038/nmeth.2019`.

[88] Arne Vancleed. *ImageJ-Particle-detection-and-analysis*. 2020. URL: `https://github.com/ArneVancleef/ImageJ-Particle-detection-and-analysis` (visited on 04/18/2025).

[89] Nobuhito Ishigure and Osamu . Matsuoka. „Bulk-etch rate of CR-39 detector under various conditions of temperature and concentration of NaOH solution“. In: *Hoken Butsuri* 18.1 (Mar. 1983), 17–21.

[90] Mangesh Pise et al. „Instantaneous-Progressive nucleation and growth of palladium during electrodeposition“. In: *Results in Surfaces and Interfaces* 6.January (2022), p. 100044. DOI: `10.1016/j.rsurfi.2022.100044`.

[91] M. Palomar-Pardavé et al. „Nucleation and diffusion-controlled growth of electroactive centers: Reduction of protons during cobalt electrodeposition“. In: *Electrochimica Acta* 50.24 (Aug. 2005), pp. 4736–4745. DOI: `10.1016/j.electacta.2005.03.004`.

[92] Tibebu Alemu, Birhanu D. Assresahegn, and Tesfaye R. Soreta. „Tuning the initial electronucleation mechanism of palladium on glassy carbon electrode“. In: *Portugaliae Electrochimica Acta* 32.1 (2014), pp. 21–33. DOI: `10.4152/pea.201401021`.

[93] A. E. Bolzán. „Electrodeposition of copper on glassy carbon electrodes in the presence of picolinic acid“. In: *Electrochimica Acta* 113 (Dec. 2013), pp. 706–718. DOI: `10.1016/J.ELECTACTA.2013.09.132`.

[94] Y. Gimeno et al. „Electrochemical formation of palladium islands on HOPG: Kinetics, morphology, and growth mechanisms“. In: *Journal of Physical Chemistry B* 106.16 (2002), pp. 4232–4244. DOI: `10.1021/jp014176e`.

[95] Yizhak Marcus. „Thermodynamics of solvation of ions. Part 6.—The standard partial molar volumes of aqueous ions at 298.15 K“. In: *J. Chem. Soc., Faraday Trans.* 89.4 (1993), 713–718. DOI: `10.1039/ft9938900713`.

[96] Yizhak Marcus and Glenn Hefter. „Standard Partial Molar Volumes of Electrolytes and Ions in Nonaqueous Solvents“. In: *Chemical Reviews* 104.7 (June 2004), 3405–3452. DOI: `10.1021/cr030047d`.

[97] Javor K. Novev, Shaltiel Eloul, and Richard G. Compton. „Influence of Reaction-Induced Thermal Convection on the Electrical Currents Measured in Chronoamperometry and Cyclic Voltammetry“. In: *The Journal of Physical Chemistry C* 120.25 (June 2016), pp. 13549–13562. DOI: `10.1021/acs.jpcc.6b03413`.

[98] Daniel Torres et al. „Distribution of Copper Electrochemical Nucleation Activities on Glassy Carbon: A New Perspective Based on Local Electrochemistry“. In: *Journal of The Electrochemical Society* 169.10 (Oct. 2022), p. 102513. DOI: `10.1149/1945-7111/ac9717`.

[99] Aleksandar Radisic et al. „Nucleation and Growth of Copper on TiN from Pyrophosphate Solution“. In: *Journal of The Electrochemical Society* 148.1 (2001), p. C41. DOI: `10.1149/1.1344539`.

[100] A. E. Alvarez and D. R. Salinas. „Formation of Cu/Pd bimetallic crystals by electrochemical deposition“. In: *Electrochimica Acta* 55.11 (Apr. 2010), pp. 3714–3720. DOI: `10.1016/J.ELECTACTA.2010.01.076`.

[101] J. Mostany et al. „Electrochemical nucleation and the classical theory: Overpotential and temperature dependence of the nucleation rate“. In: *Russian Journal of Electrochemistry* 44.6 (June 2008), 652–658. DOI: `10.1134/s1023193508060049`.

[102] Matteo Busato et al. „Elusive Coordination of the Ag+ Ion in Aqueous Solution: Evidence for a Linear Structure“. In: *Inorganic Chemistry* 59.23 (2020). PMID: 33233885, pp. 17291–17302. DOI: `10.1021/acs.inorgchem.0c02494`.

[103] Jose M. Alia and Howell G.M. Edwards. „Preferential solvation of Ag+ ions in acrylonitrile/water mixtures studied by FT-Raman spectroscopy“. In: *Vibrational Spectroscopy* 34.2 (2004), pp. 225–230. DOI: `https://doi.org/10.1016/j.vibspec.2003.10.004`.

[104] Claudio Mele et al. „Silver electrodeposition from water-acetonitrile mixed solvents and mixed electrolytes in the presence of tetrabutylammonium perchlorate. Part I-electrochemical nucleation on glassy carbon electrode“. In: *Journal of Solid State Electrochemistry* 13.10 (2009), pp. 1577–1584. DOI: `10.1007/s10008-008-0732-y`.

[105] Colin B. Baddiel, Malcolm J. Tait, and George J. Janz. „Nonaqueous silver nitrate solutions. Spectral studies in acetonitrile“. In: *Journal of Physical Chemistry* 69.10 (1965), pp. 3634–3638. DOI: `10.1021/j100894a068`.

[106] C. V. Krishnan and H. L. Friedman. „Solvation enthalpies of various ions in water and heavy water“. In: *Journal of Physical Chemistry* 74.11 (1970), pp. 2356–2362. DOI: `10.1021/j100705a020`.

[107] Ewa Kamieńska-Piotrowicz and Halina Inerowicz. „Ionic enthalpies of transfer in acetonitrile–water mixtures“. In: *J. Chem. Soc., Faraday Trans.* 86 (20 1990), pp. 3391–3394. DOI: `10.1039/FT9908603391`.

[108] Franz Hörzenberger and Gerhard Gritzner. „Gibbs energies, entropies and enthalpies of transfer for monovalent cations from acetonitrile to several solvents“. In: *J. Chem. Soc., Faraday Trans.* 89 (19 1993), pp. 3557–3564. DOI: `10.1039/FT9938903557`.

[109] Robert C. Hardy and Robert L. Cottington. „Viscosity of deuterium oxide and water in the range 5 to 125 C“. In: *Journal of Research of the National Bureau of Standards* 42.6 (1949), p. 573. DOI: `10.6028/jres.042.049`.

[110] R.A. Marcus and Norman Sutin. „Electron transfers in chemistry and biology“. In: *Biochimica et Biophysica Acta (BBA) - Reviews on Bioenergetics* 811.3 (1985), pp. 265–322. DOI: `https://doi.org/10.1016/0304-4173(85)90014-X`.

[111] Shayantan Chaudhuri and Reinhard J. Maurer. „Challenges in the Theory and Atomistic Simulation of Metal Electrodeposition“. In: *ACS Electrochemistry* 1.7 (2025), pp. 1014–1032. DOI: `10.1021/acselectrochem.4c00102`.

[112] Mengpei Qi et al. „Achieving reversible zinc electrodeposition through a holistic interfacial energy framework“. In: *Chem. Commun.* (2026), pp. –. DOI: `10.1039/D5CC06981E`.

[113] Magdalena Skompska et al. „Mixed solutions of silver cation and chloride anion in acetonitrile: Voltammetric and EQCM study“. In: *Phys. Chem. Chem. Phys.* 12 (35 2010), pp. 10525–10535. DOI: `10.1039/C003332D`.

[114] Bo Kou et al. „Surface phase stability of surface segregated AgPd and AgCu nanoalloys in an oxygen atmosphere“. In: *Applied Physics A* 127.6 (May 2021). ISSN: 1432-0630. DOI: `10.1007/s00339-021-04569-8`. URL: `http://dx.doi.org/10.1007/s00339-021-04569-8`.

[115] Giuseppe Abbondanza et al. „Hydride formation and dynamic phase changes during template-assisted Pd electrodeposition“. In: *Nanotechnology* 34.50 (Oct. 2023), p. 505605. DOI: `10.1088/1361-6528/acf66e`.

[116] Andrzej Czerwinski and Roberto Marassi. „The absorption of hydrogen and deuterium in thin palladium electrodes: Part II: Basic solutions“. In: *Journal of Electroanalytical Chemistry* 322.1 (1992). An International Journal Devoted to all Aspects of Electrode Kinetics, Interfacial Structure, Properties of Electrolytes, Colloid and Biological Electrochemistry, pp. 373–381. DOI: `https://doi.org/10.1016/0022-0728(92)80089-M`.

[117] Milad Rezaei, Seyed Hadi Tabaian, and Davoud Fatmehsari Haghshenas. „Nucleation and growth of Pd nanoparticles during electrocrystallization on pencil graphite“. In: *Electrochimica Acta* 59 (2012), pp. 360–366. DOI: `https://doi.org/10.1016/j.electacta.2011.10.081`.

[118] Silvia Ardizzone et al. „Adsorption competition effects in the electrocatalytic reduction of organic halides on silver“. In: *Journal of Electroanalytical Chemistry* 532.1 (2002), pp. 285–293. DOI: `https://doi.org/10.1016/S0022-0728(02)00950-6`.

[119] Roger Parsons, Robert M. Reeves, and Paul N. Taylor. „The electrical double layer in D2O“. In: *Journal of Electroanalytical Chemistry and Interfacial Electrochemistry* 50.1 (1974), pp. 149–152. DOI: `https://doi.org/10.1016/S0022-0728(74)80287-1`.

[120] Stanisław Lamperski. „A theoretical analysis of the Hg/D2O interface“. In: *Journal of Electroanalytical Chemistry and Interfacial Electrochemistry* 289.1 (1990), pp. 285–289. DOI: `https://doi.org/10.1016/0022-0728(90)87223-7`.

[121] Koichi Jeremiah Aoki, Jingyuan Chen, and Peng Tang. „Double Layer Impedance in Mixtures of Acetonitrile and Water“. In: *Electroanalysis* 30.8 (2018), pp. 1626–1633. DOI: `10.1002/elan.201800025`.

[122] CRC Handbook. *CRC Handbook of Chemistry and Physics, 88th Edition*. 88th ed. CRC Press, 2007. ISBN: 0849304881.

[123] Isaac Ojea-Jiménez et al. „Small Gold Nanoparticles Synthesized with Sodium Citrate and Heavy Water: Insights into the Reaction Mechanism“. In: *The Journal of Physical Chemistry C* 114.4 (2010), pp. 1800–1804. DOI: `10.1021/jp9091305`.

[124] Susanne Koeppl et al. „Usage of the isotope effect for the synthesis of ultrahigh aspect ratio gold nanorods“. In: *Journal of Materials Chemistry* 22.29 (2012), p. 14594. DOI: `10.1039/c2jm30648d`.

[125] Debasis Bera, Suresh C. Kuiry, and Sudipta Seal. „Kinetics and Growth Mechanism of Electrodeposited Palladium Nanocrystallites“. In: *The Journal of Physical Chemistry B* 108.2 (2004), pp. 556–562. DOI: `10.1021/jp036327e`.

[126] Iman Danaee. „2D–3D nucleation and growth of palladium on graphite electrode“. In: *Journal of Industrial and Engineering Chemistry* 19.3 (2013), pp. 1008–1013. DOI: `https://doi.org/10.1016/j.jiec.2012.11.024`.

[127] Micah Karahadian and Austin Smith. „Investigation of Track Formation in CR-39 for Various Hydrated Environments“. In: Jan. 2020. DOI: `10.13140/RG.2.2.34005.86244`.

[128] A. P. Young et al. „Ionomer Degradation in Polymer Electrolyte Membrane Fuel Cells“. In: *Journal of The Electrochemical Society* 157.3 (2010), B425. DOI: `10.1149/1.3281899`.

[129] M. Zatoń, J. Rozière, and D. J. Jones. „Current understanding of chemical degradation mechanisms of perfluorosulfonic acid membranes and their mitigation strategies: a review“. In: *Sustainable Energy Fuels* 1 (3 2017), pp. 409–438. DOI: `10.1039/C7SE00038C`.

[130] Edward Morse. *Nuclear Fusion*. Springer International Publishing, 2018. ISBN: 9783319981710. DOI: `10.1007/978-3-319-98171-0`.

[131] Stanislaw Szpak et al. „Evidence of nuclear reactions in the Pd lattice“. In: *Naturwissenschaften* 92.8 (July 2005), 394–397. DOI: `10.1007/s00114-005-0008-7`.

[132] J. Dash and A. Ambadkar. „Co-deposition of Palladium With Hydrogen Isotopes“. In: *Condensed Matter Nuclear Science*. World Scientific, Feb. 2006, 477–484. DOI: `10.1142/9789812774354_0038`.

[133] Tadahiko Mizuno, Tadayoshi Ohmori, and Michio Enyo. „Isotopic changes of the reaction products induced by cathodic electrolysis in Pd“. In: *J. New Energy* 1 (Sept. 1996).

[134] Gaurav Yadav, Neelkanth Nirmalkar, and Claus-Dieter Ohl. „Electrochemically reactive colloidal nanobubbles by water splitting“. In: *Journal of Colloid and Interface Science* 663 (2024), pp. 518–531. DOI: `https://doi.org/10.1016/j.jcis.2024.02.148`.

[135] Xuegeng Yang et al. „Dynamics of Single Hydrogen Bubbles at a Platinum Microelectrode“. In: *Langmuir* 31.29 (2015). PMID: 26133052, pp. 8184–8193. DOI: `10.1021/acs.langmuir.5b01825`.

[136] Çayan Demirkır et al. „Life beyond Fritz: On the Detachment of Electrolytic Bubbles“. In: *Langmuir* 40.39 (2024). PMID: 39305203, pp. 20474–20484. DOI: `10.1021/acs.langmuir.4c01963`.

[137] Rui Hao et al. „Imaging nanobubble nucleation and hydrogen spillover during electrocatalytic water splitting“. In: *Proceedings of the National Academy of Sciences* 115.23 (2018), pp. 5878–5883. DOI: `10.1073/pnas.1800945115`.

[138] Shasha Guo et al. „Separating nanobubble nucleation for transfer-resistance-free electrocatalysis“. In: *Nature communications* 16.1 (2025), p. 919. DOI: `10.1038/s41467-024-55750-5`.

[139] Van-Tu Nguyen et al. „Modeling of the bubble collapse with water jets and pressure loads using a geometrical volume of fluid based simulation method“. In: *International Journal of Multiphase Flow* 152 (2022), p. 104103. DOI: `https://doi.org/10.1016/j.ijmultiphaseflow.2022.104103`.

[140] Joachim Dzubiella. „Interface dynamics of microscopic cavities in water“. In: *The Journal of Chemical Physics* 126.19 (May 2007), p. 194504. DOI: `10.1063/1.2734962`.

[141] Julien Lombard, Thierry Biben, and Samy Merabia. „Kinetics of Nanobubble Generation Around Overheated Nanoparticles“. In: *Phys. Rev. Lett.* 112 (10 Mar. 2014), p. 105701. DOI: `10.1103/PhysRevLett.112.105701`.

[142] Vitaly B. Svetovoy et al. „Explosion of Microbubbles Generated by the Alternating Polarity Water Electrolysis“. In: *Energies* 13.1 (2020). DOI: `10.3390/en13010020`.

[143] Ilia V. Uvarov et al. „Highly energetic impact of H2 and O2 nanobubbles on Pt surface“. In: *Journal of Colloid and Interface Science* 582 (2021), pp. 167–176. DOI: `https://doi.org/10.1016/j.jcis.2020.07.135`.

[144] Vitaly B. Svetovoy et al. „Combustion of hydrogen-oxygen mixture in electrochemically generated nanobubbles“. In: *Phys. Rev. E* 84 (3 Sept. 2011), p. 035302. DOI: `10.1103/PhysRevE.84.035302`.

[145] Alexander Prokaznikov, Niels Tas, and Vitaly Svetovoy. „Surface Assisted Combustion of Hydrogen-Oxygen Mixture in Nanobubbles Produced by Electrolysis“. In: *Energies* 10.2 (2017). DOI: `10.3390/en10020178`.

[146] Tetsuo Sakai, Hiroyasu Takenaka, and Eiichi Torikai. „Gas Diffusion in the Dried and Hydrated Nafions“. In: *Journal of The Electrochemical Society* 133.1 (Jan. 1986), 88–92. DOI: `10.1149/1.2108551`.

[147] Professional Plastics. *CR-39 Homalite Sheet*. Accessed: 2025-06-12. 2025. URL: `https://www.professionalplastics.com/CR39-HOMALITESHEET`.

[148] Lev I. Krishtalik. „Kinetic isotope effect in the hydrogen evolution reaction“. In: *Electrochimica Acta* 46.19 (2001), pp. 2949–2960. DOI: `https://doi.org/10.1016/S0013-4686(01)00526-6`.

[149] Sunghak Park et al. „Solutal Marangoni effect determines bubble dynamics during electrocatalytic hydrogen evolution“. In: *Nature Chemistry* 15.11 (Aug. 2023), 1532–1540. DOI: `10.1038/s41557-023-01294-y`.

[150] Ines M. Hauner et al. „The Dynamic Surface Tension of Water“. In: *The Journal of Physical Chemistry Letters* 8.7 (2017). PMID: 28301160, pp. 1599–1603. DOI: `10.1021/acs.jpclett.7b00267`.

[151] J. R. Heiks et al. „The Density, Surface Tension and Viscosity of Deuterium Oxide at Elevated Temperatures“. In: *The Journal of Physical Chemistry* 58.6 (1954), pp. 488–491. DOI: `10.1021/j150516a010`.

[152] Kenneth Suslick and Gareth Price. „Application of Ultrasound to Materials Chemistry“. In: *Annual Review of Materials Science* 29 (Aug. 1999), pp. 295–326. DOI: `10.1146/annurev.matsci.29.1.295`.

[153] H. Sayed-Ahmed, Á.I. Toldy, and A. Santasalo-Aarnio. „Dynamic operation of proton exchange membrane electrolyzers—Critical review“. In: *Renewable and Sustainable Energy Reviews* 189 (2024), p. 113883. DOI: `https://doi.org/10.1016/j.rser.2023.113883`.

[154] Xu Zhao, Hang Ren, and Long Luo. „Gas Bubbles in Electrochemical Gas Evolution Reactions“. In: *Langmuir* 35.16 (2019). PMID: 30888828, pp. 5392–5408. DOI: `10.1021/acs.langmuir.9b00119`.

[155] S. C. Bădescu et al. „Vibrational states of a H monolayer on the Pt(111) surface“. In: *Phys. Rev. B* 68 (20 Nov. 2003), p. 205401. DOI: `10.1103/PhysRevB.68.205401`.

[156] Akiko Katayama and Hideaki Kita. „Adsorption of Hydrogen on a Platinum-Graphite Catalyst: Part II. Measurements in the Electrochemical System by Electron Spin Resonance and Potential-Sweep Techniques“. In: *Journal of the Research Institute for Catalysis Hokkaido University* 26.3 (Feb. 1979), pp. 131–143. URL: `http://hdl.handle.net/2115/25049`.

[157] Leon Jacobse, Marcel J. Rost, and Marc T. M. Koper. „Atomic-Scale Identification of the Electrochemical Roughening of Platinum“. In: *ACS Central Science* 5.12 (Oct. 2019), 1920–1928. DOI: `10.1021/acscentsci.9b00782`.

[158] Juan M. Feliu and Enrique Herrero. „Pt single crystal surfaces in electrochemistry and electrocatalysis“. In: *EES Catalysis* 2.2 (2024), 399–410. DOI: `10.1039/d3ey00260h`.

[159] Marcus D. Pohl et al. „Elucidation of adsorption processes at the surface of Pt(331) model electrocatalysts in acidic aqueous media“. In: *Physical Chemistry Chemical Physics* 18.16 (2016), 10792–10799. DOI: `10.1039/c5cp08000b`.

[160] Kun-Ting Song et al. „Influence of Alkali Metal Cations on the Oxygen Reduction Activity of Pt5Y and Pt5Gd Alloys“. In: *The Journal of Physical Chemistry C* 128.12 (2024), pp. 4969–4977. DOI: `10.1021/acs.jpcc.4c00531`.

[161] Sudarsan Surendralal, Mira Todorova, and Jörg Neugebauer. „Laterally Resolved Free Energy Profiles and Vibrational Spectra of Chemisorbed H Atoms on Pt(111)“. In: *Journal of Chemical Theory and Computation* 20.5 (Feb. 2024), 2192–2201. DOI: `10.1021/acs.jctc.3c00997`.

TURUN YLIOPISTO
UNIVERSITY OF TURKU

ISBN 978-952-02-0584-3 (PRINT)
ISBN 978-952-02-0585-0 (PDF)
ISSN 2736-9390 (PRINT)
ISSN 2736-9684 (ONLINE)

Painosalama, Turku, Finland 2026